Setup of a Penning trap for precision laser spectroscopy at HITRAP

Trapping, cooling and electronic detection of externally produced ions

Dissertation

zur Erlangung des Grades
„Doktor der Naturwissenschaften“

im Promotionsfach Chemie
am Fachbereich Chemie, Pharmazie und Geowissenschaften
der Johannes Gutenberg-Universität Mainz

Zoran Anđelković
geb. in Belgrad, Serbien

Mainz, den 22. März 2012

Contents

List of Figures

List of Tables

Abstract

Ion traps have been established as a powerful tool for ion cooling and laser spectroscopy experiments since a long time ago. SpecTrap, one of the precision experiments associated to the HITRAP facility at GSI, is implementing a Penning trap for studies of large bunches of externally produced highly charged ions. The extremely strong electric and magnetic fields that exist around the nuclei of heavy elements drastically change their electronic properties, such as energy level spacings and radiative lifetimes. The electrons can therefore serve as sensitive probes for nuclear properties such as size, magnetic moment and spatial distribution of charge and magnetization. The energies of forbidden fine and hyperfine structure transitions in such ions strongly depend on the nuclear charge and shift from the microwave domain into the optical domain. Thus, they become accessible for laser spectroscopy and its potentially high accuracy. A number of such measurements has been performed in storage rings and electron beam ion traps and yielded results with relative accuracies in the 10^{-3} to 10^{-4} region. This work presents the construction and commissioning of a Penning trap used for capturing highly charged ions in-flight and cooling them nearly to rest, thus reducing Doppler broadening and increasing the possible accuracy. As an important step-stone towards that goal, singly charged Mg ions were produced in an electron impact ion source, transported to the trap and laser cooled to sub-K temperatures. Indications of Coulomb crystals formation are reported. Non-destructive detection of the stored ions was performed both electronically, with the attached cryogenic resonant circuits, and optically, by observing the fluorescence directly from the trap centre. The designed electronic components can also be used for resistive cooling, which becomes particularly efficient for highly charged ions. It was demonstrated that large ion clouds can be created in the trap, formed by accumulating many consecutive ion source shots. Ions were stored with lifetimes of the order of 100 s and cooled to temperatures lower than 60 mK. The same technique can be used in future experiments for mixing laser-cooled Mg^+ with highly charged ions delivered by HITRAP. Thus, sympathetic cooling of highly charged ions to sub-K temperatures will become possible. This is sufficient for reducing the Doppler width of a transition in a heavy ion to several MHz and enables laser spectroscopy experiments with a relative accuracy up to 10^{-8}.

Zusammenfassung

Ionenfallen sind bereits seit geraumer Zeit wohletablierte Instrumente für die Speicherung und Kühlung von Ionen, insbesondere vor dem Hintergrund von Laserspektroskopie-Experimenten. SpecTrap ist eines der Präzisionsexperimente im Rahmen des HITRAP-Projekts an der GSI und verwendet eine Penning-Ionenfalle für spektroskopische Untersuchungen an extern erzeugten, hoch geladenen Ionen. In solchen Wenig-Elektronensystemen erfahren die elektronischen Energieniveaus und radiativen Lebensdauern von Zuständen extreme Veränderungen durch die hohen elektrischen und magnetischen Feldstärken in der Nähe des ionischen Kerns. Sie sind daher sehr empfindliche Proben für Kerneigenschaften wie etwa Größe, magnetisches Moment und die räumlichen Verteilungen der Ladung und Magnetisierung. Übergänge zwischen Niveaus der Fein- und Hyperfeinstruktur sind magnetische Dipolübergänge, die durch die starke Abhängigkeit der Kernfelder von der Kernladungszahl im optischen Wellenlängenbereich liegen können. Sie sind daher den Methoden der Laserspektroskopie und der damit verbundenen hohen Präzision zugänglich. Verschiedene Messungen an derartigen Übergängen sind bereits in Speicherringen und Elektronenstrahl-Ionenfallen durchgeführt worden, mit relativen Genauigkeiten im Promille-Bereich. In dieser Arbeit wird der Aufbau und die Durchführung eines Penningfallen-Experiments vorgestellt, welches geeignet ist, extern erzeugte, hoch geladene Ionen einzufangen, zu speichern, zu kühlen und mit noch größeren relativen Genauigkeiten zu spektroskopieren. Als Vorbereitung hierauf wurden einfach geladene Mg-Ionen in einer externen Quelle erzeugt, in die Falle eingefangen, gespeichert und auf Temperaturen unterhalb von einem Kelvin gekühlt. Experimentelle Hinweise auf die Bildung von Coulomb-Kristallen wurden gesammelt. Das Experiment erlaubt sowohl elektronische und optische Kühlung der Ionenbewegung als auch zerstörungsfreien elektronischen und optischen Nachweis der gespeicherten Ionen. Große Ionenensembles konnten in der Falle gesammelt und gespeichert werden durch wiederholten Einfang von extern erzeugten Ionen. Diese Ensembles konnten mit einer Speicherzeitkonstanten von etwa 100 Sekunden gespeichert und auf Temperaturen von unterhalb 60 mK gekühlt werden. Hiermit können in künftigen Experimenten die hoch geladenen Ionen aus der HITRAP-Anlage sympathetisch auf entsprechende Temperaturen gekühlt werden. Diese Kühlung ermöglicht Spektroskopie bei relativen Dopplerbreiten der untersuchten Übergänge von der Größenordnung MHz und erlaubt damit relative spektroskopische Auflösungen von etwa 10^{-8}.

Introduction

Contrary to what we see in the world around us, a large part of our universe consists of highly ionized matter [1], located predominantly in stars. Because of the Earth's atmosphere which absorbs most of the X-ray radiation that would tell us of their existence, we cannot see much of highly charged ions (HCI) under "normal" conditions. However, as the technology advanced towards HCI production, so did the theory which explains the fundamental processes that take place within them. A good example are the astrophysical plasmas, which can be modelled according to the processes observed in micro-plasmas of HCI formed in a laboratory. On the other hand, the calculation of quantum electrodynamics (QED) contributions to the bound electrons' energies in HCI has seen significant advances and can now be applied to ever more complex systems, offering an opportunity to test QED on an even higher level. The overall error budget in the calculated electronic level energies is dominated by the electron-electron correlations and nuclear effects, and still requires experimental input to be benchmarked.

With the introduction of electron beam ion traps (EBITs) medium-heavy and heavy highly charged ions became available for experiments [2]. Alternatively, suitable ions with extremely high charge states can be created at heavy ion accelerator facilities such as GSI Darmstadt [3], where a fast ion beam of low charge states is further ionized by passing a stripper foil. These HCI are then injected into the experimental storage ring (ESR), where they can be investigated at high energies or decelerated down to 4 MeV/u. The new HITRAP facility at GSI is designed to extract these bunches and decelerate them to the sub-eV energy region [4]. As a result, a cooled bunch of some 10^5 HCI can be delivered to several precision experiments associated with HITRAP, out of which SpecTrap, the topic of this thesis work, aims to trap them in a Penning trap, cool to ultra-low temperatures, and investigate by means of precision laser spectroscopy.

A cylindrical, open-endcap Penning trap has been chosen for these experiments, since the design offers both an open geometry for capturing externally produced ions and a harmonic potential necessary for decoupling of different ion eigenmotions. Within this work it has been installed in a vertical, cold-bore, split-coil superconducting magnet and equipped with electronic components necessary for manipulation and non-destructive detection of the trapped ions. Optical access to the trapped ions is possible axially, through the open endcaps, as well as radially, through four round holes in the central trap electrode, aligned with the optical ports of the magnet. Ions are injected axially from above and a laser beam from the opposite side, as seen in Fig. 1, leaving the radial plain free for fluorescence detection.

Laser and sympathetic cooling can be used for reducing the temperature of trapped ions even below the liquid helium temperature of the magnet and the trap and are foreseen for use in

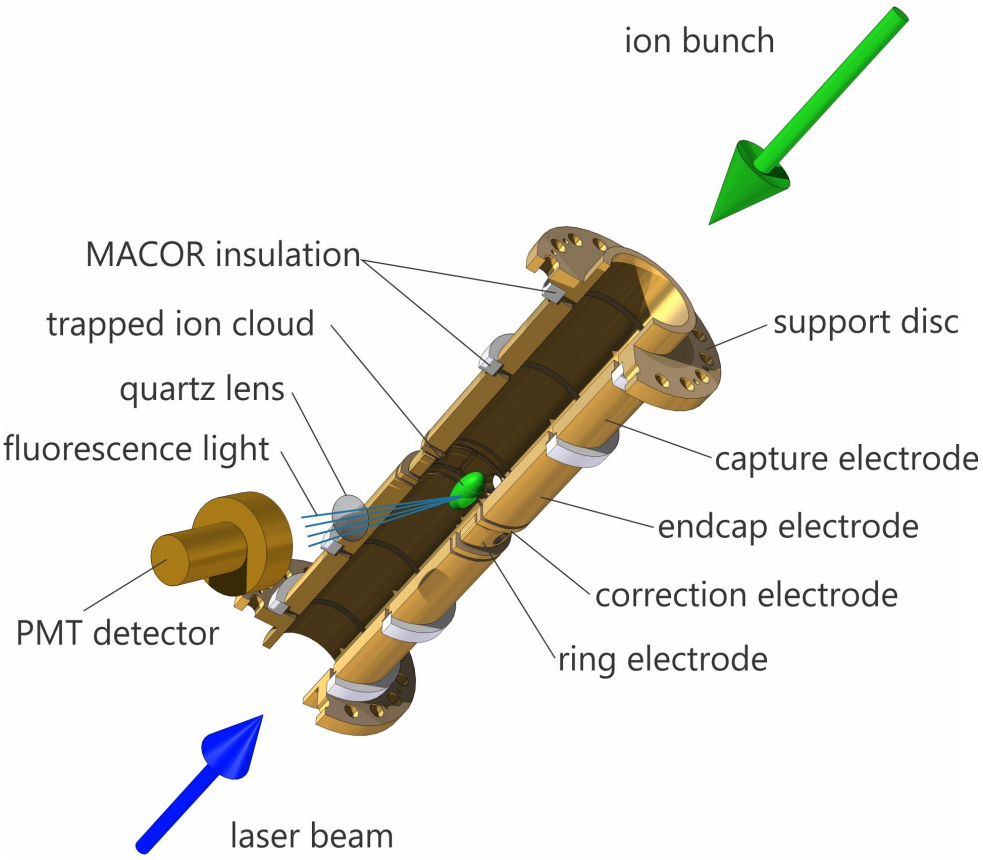

Figure 1: Overview of the SpecTrap ion trap, indicating the direction of the injected ions, laser beam and fluorescence detection.

SpecTrap. Because of their favourable level structure, singly charged Mg ions have been chosen for commissioning the system, as well as for further use in experiments with HCI. This work will demonstrate that it is possible to trap externally produced Mg ions in SpecTrap for extended amounts of time, laser cool them to sub-K temperatures and detect their fluorescence directly from the trap centre, thus preparing the system for the planned trapping and sympathetic cooling of HCI.

The first two chapters of this thesis will give the theoretical background of laser spectroscopy of highly charged ions, as well as the techniques of ion confinement, cooling and detection. Especially important are the principles of resonant circuits and their use for non-destructive ion detection. An overview of the SpecTrap Penning trap system and the required experimental equipment is given in the next two chapters. A lot of work has also been invested into construction of the vacuum system and the ion beamline guiding the ions towards the trap. The final two chapters, followed by conclusions and an outlook, give the results of commissioning the ion beamline and the trap, as well as the first trapping and laser cooling results for Mg^+.

Chapter 1

Laser spectroscopy of forbidden transitions in highly charged ions

As an experimental technique, laser spectroscopy has led to significant advances in the accuracy of determining spectral line frequencies and has a fundamental importance for research of atomic processes. Also in experiments with HCI, laser spectroscopy has proven to be a valuable tool for precision measurements [5, 6, 7]. Experimental access to fine and hyperfine structure of HCI became possible in the last two decades, providing sensitive tests for the corresponding theoretical atomic structure calculations [8, 9].

After a general introduction into the field and terminology of highly charged ions, sections 1.1.1 and 1.1.2 will present the possibilities of their production at GSI. SpecTrap aims to measure ground-state electronic fine and hyperfine transitions in HCI, which are electric-dipole forbidden, and the corresponding theory is given in section 1.2. Finally, some basics of laser spectroscopy are briefly treated by section 1.3.

1.1. Highly charged ions

The definition of a *highly charged ion* (HCI) is not unique, but depends on the application. Wile sometimes already ions missing more than one or two electrons are referred to as HCI, a more precise definition states that an HCI is an ion stripped of multiple electrons, in a process where the ionization energy was significantly higher than the energy scale of standard laboratory atomic interactions (i.e. $Q \gg 1$ and $U \gg 10$ eV). Thus, typical HCI considered throughout this work will have a charge $Q > 10$ and an ionization energy $U > 1000$ eV.

During the last two decades technology has sufficiently advanced to allow routine production and research of HCI under well-controlled laboratory conditions. That has offered new insights into the structure of matter and vacuum, which were not possible before. To elaborate this point, it is convenient to compare the size, i.e. the wavefunction of a hydrogen-like uranium U^{91+}, to that of hydrogen. The Bohr radius R scales inversely with the atomic number

$$R \sim \frac{1}{Z} \sim \frac{1}{Q+1} \sim \frac{1}{Q} \qquad \text{for } Q \gg 1 \tag{1.1}$$

and reduces the average distance of the electron from the nucleus by about two orders of magnitude. This already falls below the Compton wavelength of the electron (2 pm) and single-particle quantum mechanics starts to break down. Instead, quantum field theory is needed to accurately describe the system. This is because in the new picture the structure of vacuum begins to play a significant role - virtual electron-positron pairs which polarize the space and screen the bare charge of an electron faint at smaller distances. The electron charge gets less and less screened and in the extreme case effectively increases far above the nominal $1.6 \cdot 10^{-19}$ C.

When speaking of highly charged ions, there are two principle ways how to organize the data. From the experimental point of view, a logical course of action would be to follow the way HCI are produced and speak of a series of charge states of an ion whose nucleus always has the same charge and mass. This defines an *isonuclear sequence*. From the theoretical point of view, it makes much more sense to fix the number of electrons and change the properties of the nucleus. That defines an *isoelectronic sequence*.

The ionization energy U needed to produce a highly charged ion increases rapidly along an isonuclear sequence. It scales quadratically with the nuclear charge number

$$U(Z) \sim \frac{Z}{R} \sim \frac{Z}{1/Z} = Z^2. \tag{1.2}$$

This can also be seen from the solution of the Dirac equation for the 1s energy level

$$E_{1s} = m_e c^2 \sqrt{1 - Z^2\alpha^2} \approx m_e c^2 \left(1 - \frac{Z^2\alpha^2}{2} - \cdots\right) \qquad \text{for } Z\alpha \ll 1 \tag{1.3}$$

where m_e is the electron mass and $\alpha = \frac{e^2}{4\pi\epsilon_0\hbar c}$ the fine structure constant. A comparison of Eq.(1.3) and experimental results is shown in Fig. 1.1. It should be noted that the term *ionization energy* refers to the energy required to remove one electron from an ion (atom), and Fig. 1.1 shows the energy needed to remove the last electron in hydrogen-like ions. It should not be mixed up with the *neutralization energy*, which is the total energy required to reach a certain charge state and corresponds to the sum of all ionization energies.

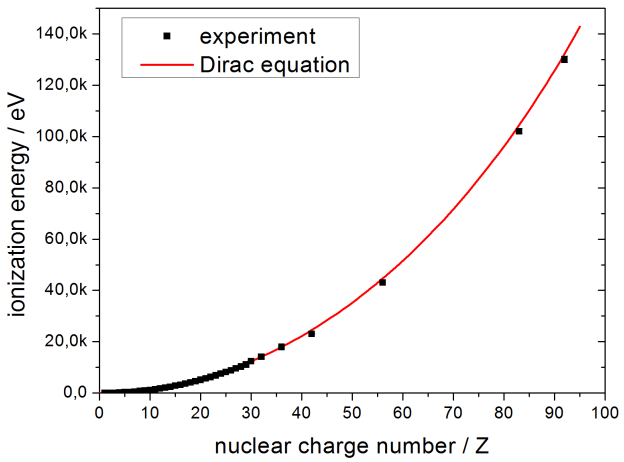

Figure 1.1: A graph showing how the ionization energy required for producing a hydrogen-like ion from a helium-like ion scales with the nuclear charge number. The data points are experimental results taken from [10, 11, 12], while the curve is calculated using Eq.(1.3).

The energies separating different eigenstates in highly charged ions rapidly decrease along an isoelectronic sequence. In other words, the wavelength of the emitted light scales inversely with

the nuclear charge and the rate depends on the terms in the Hamiltonian. The separation energy between states with different n quantum numbers scales with Z^2 since it is dominated by the Coulomb potential. In the case of fine structure transitions (see section 1.2.2) relativistic effects are dominant, and they scale faster with charge, typically as Z^4. In a semi-classical picture this can be illustrated using the relativistic energy expression

$$E = \sqrt{p^2c^2 + m_o^2c^4} \approx m_0c^2 + \frac{p^2}{2m_0} - \frac{p^4}{8m_0^3c^2} + \cdots . \tag{1.4}$$

The first two terms are the rest mass and the classical kinetic energy, while the third term gives the relativistic contribution. Since the orbital angular momentum $l = r \times p$ is fixed as a quantum number, p has to increase as the radius r decreases, producing the Z^4 scaling of the energy [13].

Finally, the hyperfine structure splitting (see section 1.2.3), arising from the interaction with the magnetic moment of the nucleus, scales as Z^3 [14]. This can be explained by considering the field induced in the nucleus by the orbiting electron. It scales inversely with the third power of the radius, which in turn has an inverse dependence on the charge as already mentioned. As a result, the hyperfine structure separation will also scale with the third power of charge.

A very important consequence of the strong transition energy scaling with charge is the fact that both fine and hyperfine structure transitions start entering the optical regime at some point (see chapters 1.2.2 and 1.2.3). This allows high-resolution laser spectroscopy measurements with sufficiently high accuracy to gain insight into the internal structure of the nucleus and to test the corresponding quantum electrodynamics (QED) calculations. Such measurements are also the goal of SpecTrap. The influence of the strong fields to the vacuum structure is probably one of the most remarkable aspects of quantum electrodynamics. It states that ordinary vacuum becomes unstable under the influence of a strong electric field and a phase transition from the neutral to the charged state through generation of electron-positron pairs occurs [15]. Such a strong field cannot be produced in a laboratory, and it exists only around the nuclei of very heavy highly charged ions, as Fig. 1.2 shows. The theory predicts that the critical field strength is expected around $Z > \alpha \approx 137$ [1], where the term under the square root from Eq.(1.3) is negative, and the nature prevents us from making an even more highly charged ion by electron creation from the vacuum. The study of HCI at $Z < 92$ is important to understand QED in such strong fields, and it remains an active investigation topic of [5, 6, 16] and of this work.

Highly charged ion production can be realized in two principle ways. The first method is the so-called in-flight stripping, where a fast ion beam impinges on a solid target, and its electrons are removed in collisions with the target's slow particles [17]. The main advantage of this production method is applicability to basically any ion species, with a relatively high yield; the main disadvantage is the need of an accelerator, which in turn delivers HCI at very high energies. The second way of producing highly charged ions exploits multiple ionization of comparably slow ions by energetic electrons. The devices which work on this principle are electron cyclotron resonance ion sources (ECRIS) and electron beam ions traps (EBIT) [2]. The main advantage of the system is an almost table-top size of the equipment delivering relatively low energy ions; the main disadvantage is a much lower yield of higher charge states.

[1] If the finite size of the nucleus is taken into account, this number is actually 173.

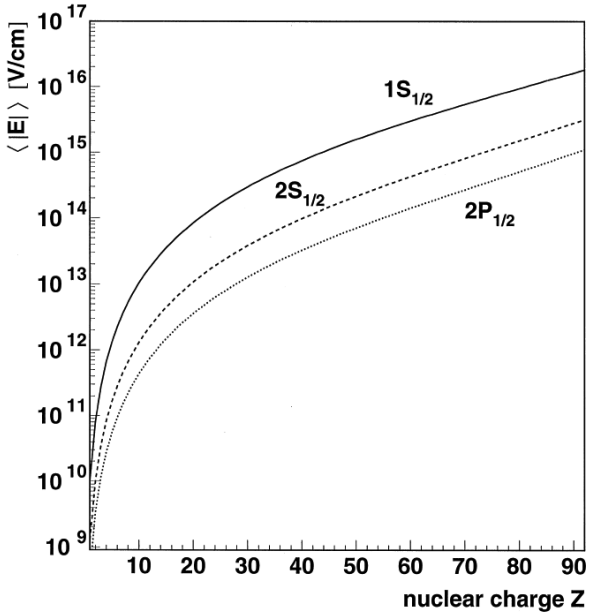

Figure 1.2: Average electrical field strength at the lowest-lying energy levels of hydrogen-like ions with atomic numbers from Z=1 to Z=92. It can be seen that hydrogen-like uranium exerts an electrical field of some 10^{16} V/cm on a 1s electron, while the highest fields achieved in the laboratory are of the order of 10^{14} V/cm. Picture reproduced from [14].

1.1.1. Heavy highly charged ions at the GSI accelerator facility

An overview of the GSI accelerator facility is shown in Fig. 1.3. Several ion sources can be used to produce almost any stable ion species, ranging from hydrogen to uranium. The initial acceleration and first stripping take place in the universal linear accelerator (UNILAC). The heavy ion synchrotron (SIS-18) takes care of further acceleration with energies ranging up to 1 GeV/u. The ion beam ejected from the SIS impinges on a stripper target, highly charged species of the incident ions are produced and the desired charge state is then injected into the experimental storage ring (ESR), where it can be bunched, cooled in the electron cooler and prepared for high-precision experiments at a desired energy. Laser spectroscopy with fast highly charged ions (in the MeV/u range) has already been conducted at the ESR, but suffered from large Doppler broadening and uncertainty of the ion beam energy, which limited the relative accuracy to $\Delta\nu/\nu \sim 10^{-4}$ [5, 6]. It would be much more favourable if ions could be decelerated to far lower energies (into the eV range) and made available for precision experiments. A proposal for such a facility was accepted by GSI and the construction of HITRAP (heavy ion trap) began in 2006.

Even though the ESR is optimized for ion storage and experiments, it can also be used to decelerate the stored ions down to 4 MeV/u. HITRAP uses this mode to prepare the ions for further deceleration. The HITRAP deceleration beamline is located in the SIS reinjection channel, directly behind the ESR ejection port. It consists of several stages, corresponding to different energy ranges, as shown in Fig. 1.4. The first part is the double-drift buncher (DDB) which reshapes the ESR ion bunch for the first HITRAP deceleration stage - an integrated H-type linear decelerator (IH-linac). This one slows the ion bunch from the initial 4 MeV/u down to 0.5 MeV/u. The next deceleration stage is a radio frequency quadrupole (RFQ), which goes down to 6 keV/u. It should be emphasized that all these structures only slow down the ion bunch and perform no cooling (i.e. do not reduce the energy distribution). After deceleration, the low energy

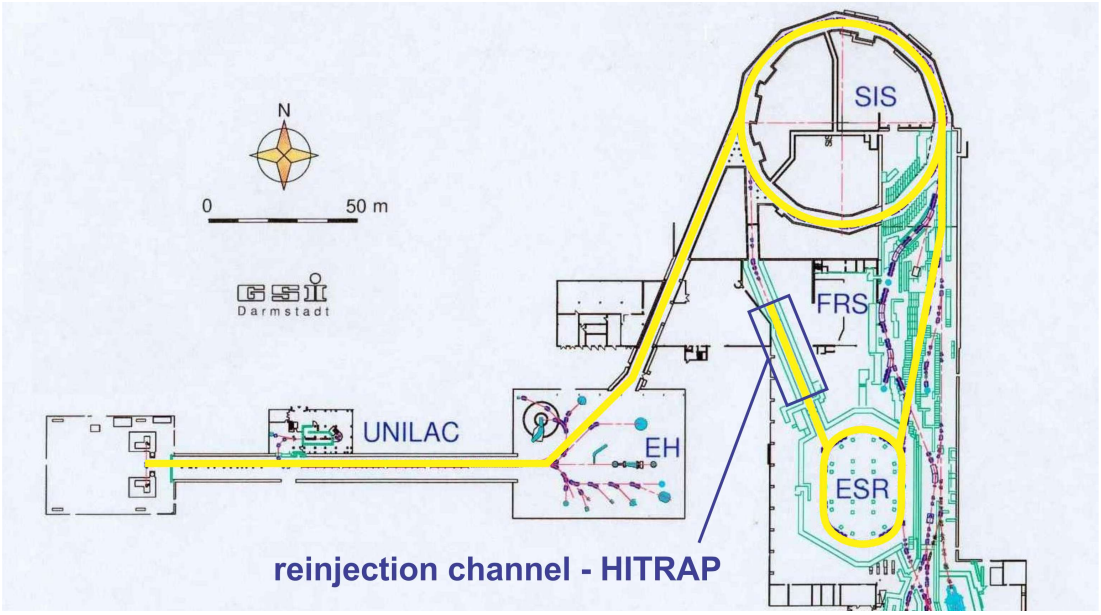

Figure 1.3: Overview of the GSI accelerator facility. After production, the ion beam (yellow line) is guided through several ionization and acceleration stages, until it is ejected from the SIS, stripped of electrons and injected into the storage ring. There it can be pre-cooled, slowed down, and forwarded to HITRAP, which is itself located in the former SIS reinjection channel.

beam transport (LEBT) prepares particles for trapping in the cooler trap. Here, as the name suggests, ion cooling to energies less than 1 eV takes place. The details of the whole process can be found in several articles and PhD theses [18, 19, 20, 21].

The cooled ions can be extracted from the cooler trap at several keV/q (for practical reasons the energy units at this point change from keV/u to keV/q). It is guided to the upper level of the facility, where they will be distributed to different experiments, one of them being SpecTrap.

1.1.2. Mid-Z highly charged ions and the HITRAP EBIT

The idea of using fast electrons to ionize comparably slow atoms arose in the late '60s in Dubna, Russia [22]. Gas atoms are multiply ionized by a constant mono-energetic electron beam, and the process usually takes place in elongated drift tubes surrounded by a solenoid. The generated magnetic field compresses the electron beam and thus also helps to define the radially-confining potential for the created ions. The whole apparatus became commonly known as an electron beam ion source, or EBIS.

As an EBIS spin-off, the electron beam ion trap, or EBIT, was first conceived at Lawrence Livermore National Laboratory in the late '80s [2]. The main difference is the much stronger magnetic field, which allows also much stronger electron beams and offers additionally the "Penning trap operation" of the device, where the radial confinement is not lost after switching off the electron beam (hence the name). The EBITs of today all have the possibility of extracting the produced ions, what makes the EBIT-EBIS difference blurry, and the terminology is often used inconsistently.

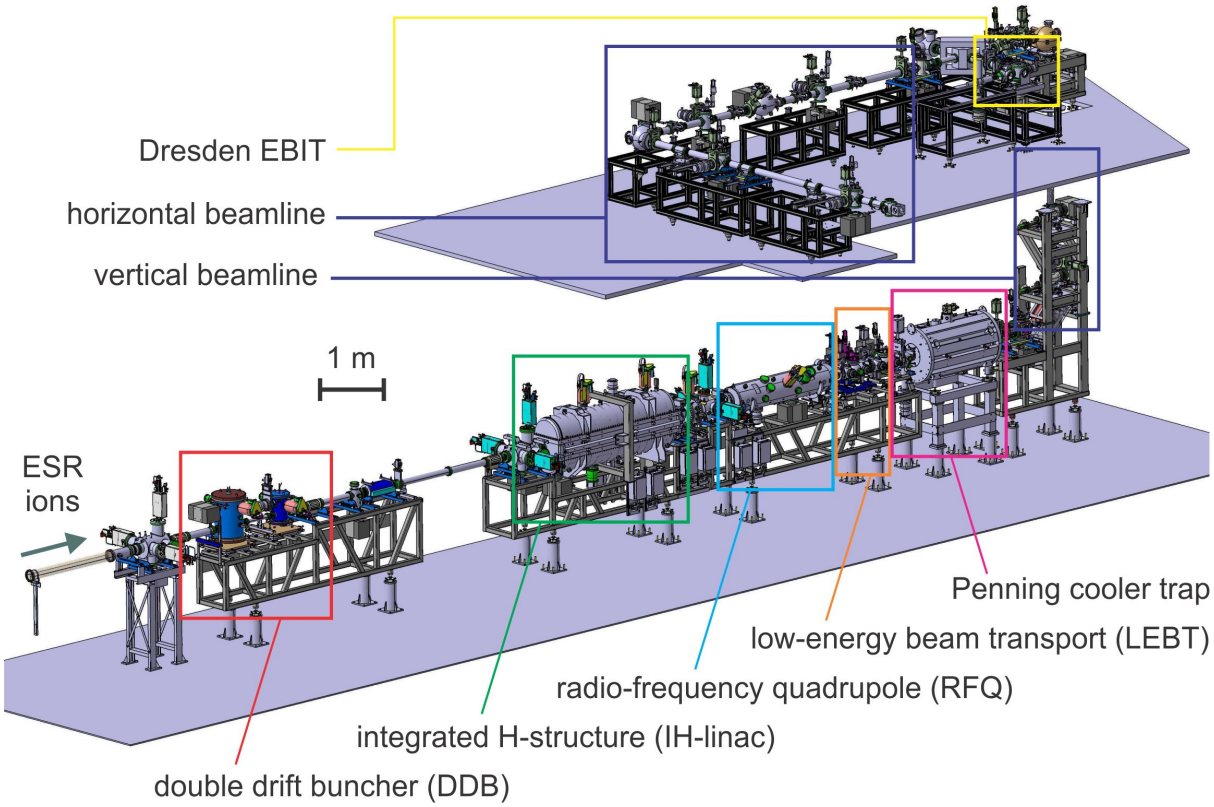

Figure 1.4: Overview of the HITRAP facility. The lower level contains different deceleration elements, as noted on the figure and described in the text. The ions injected from the ESR are decelerated in several steps, stored and cooled in the cooler trap, before they are distributed via the vertical beamline to the experiments on the upper level. An EBIT is also located there, which can provide HCI for off-line experiments. SpecTrap will be connected to the far end of the horizontal beamline, which awaits construction (status March 2012).

As will be discussed in section 1.2.2, optical fine-structure transitions, suitable for laser spectroscopy measurements in SpecTrap, can be found in mid-Z highly charged ions, which can be easily reached with commercial EBITs. A Dresden EBIT, the smallest model of the company DREEBIT, was purchased to serve as an ion source for commissioning the HITRAP cooler trap and for experiments with mid-Z highly charged ions [23]. Its operation principle is illustrated in Fig. 1.5. The negative potential of the cathode U_{cathode} accelerates the created electrons towards the drift tube structure, which is kept on a positive potential U_{ion}. This defines the kinetic energy of the electrons with respect to the ions simply as $E_e = (|U_{\text{cathode}}| + |U_{\text{ion}}|)e$, where e is the electron charge. The magnetic field compresses the electrons radially via the Lorentz force and creates a high current density in the ionization region. This electron beam also creates the potential needed for radial confinement of the ions. Axial confinement is provided by the side electrodes, which are kept on a higher positive potential than the drift tube. After a desired charge breeding time, one of these side potentials can be dropped, and the ions are extracted with energy $E_i = U_{\text{ion}}q$, where q is the charge of the ion.

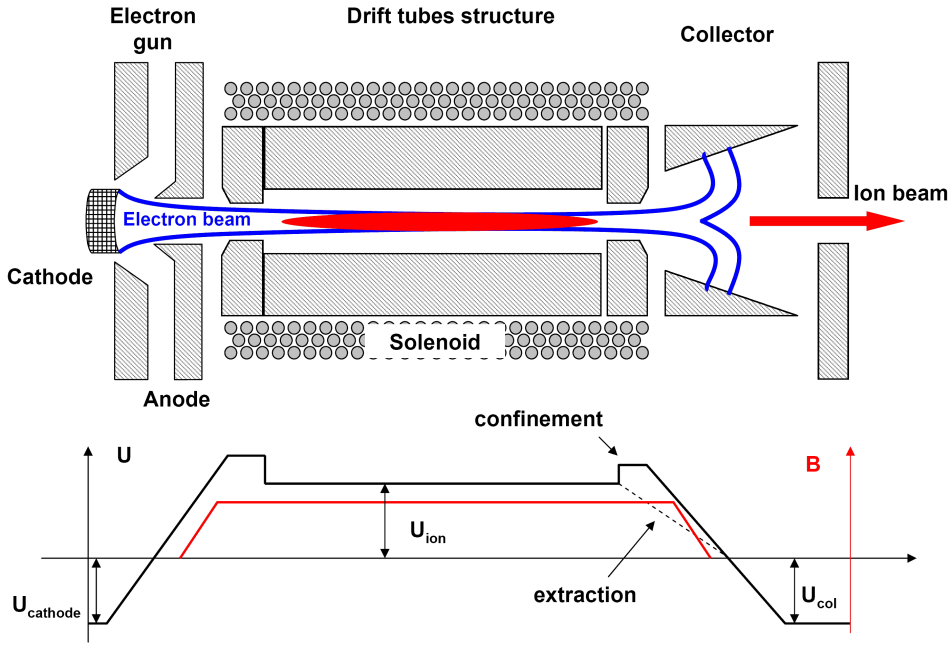

Figure 1.5: A sketch of the Dresden EBIT design and operation principle. The upper part shows the electrode configuration and the electron-ion overlap (given in blue and red). The lower part shows the electrical potentials used for confinement and the magnetic field strength in the ionization region used for compressing the electron beam. Picture reproduced with courtesy of A. Sokolov [24], while the ion production data can be seen online at www.dreebit.com.

1.2. Forbidden transitions in highly charged ions

In general, all transitions which are electric dipole (E1) forbidden are referred to as *forbidden* transitions. In fine and hyperfine structure transitions within the same electronic configuration parity does not change, and hence, they violate the selection rules of an E1 transition. An atom can nevertheless undergo such a transition by absorbing magnetic dipole radiation which does not require a change in n and l quantum numbers. It is then said the transition is magnetic-dipole (M1) allowed.

Although much weaker than E1, the M1 transitions are of big scientific interest because of the very fact that they take place within the same level multiplet. This means that they often represent a *ground state* transition, i.e. a transition between two lowest lying energy levels, without any possibility of electron shelving in dark states. The following sections give the theoretical background of transition probabilities, their selection rules, as well as calculations of ground state transition energies in highly charged ions.

1.2.1. Transition probabilities

The modified Hamiltonian for the semi-classical interaction of a quantum mechanical atom with a classical radiation field is given by

$$H = \frac{1}{2m_e}(\mathbf{p} + e\mathbf{A})^2 - e\phi + V_{\text{coul}} \tag{1.5}$$

where m_e and e are electron mass and charge respectively, p its momentum, ϕ and $\mathbf{A}$ scalar and vector potentials and V_{coul} the Coulomb potential energy. Here, the spin of the particle and its interaction with the magnetic field of the wave has been neglected. The Hamiltonian from Eq.(1.5) can be split into the unperturbed and the perturbation Hamiltonian

$$H = H_0 + H' \tag{1.6}$$

where

$$H_0 = \frac{p^2}{2m_e} + V_{\text{coul}} \qquad \text{and} \qquad H' = \frac{e}{2m_e}(\mathbf{p}\cdot\mathbf{A} + \mathbf{A}\cdot\mathbf{p}) + \frac{e^2}{2m_e}A^2 - e\phi. \tag{1.7}$$

If the radiation is taken as an incoherent superposition of plane waves periodic in time with $\phi = 0$, the Lorentz gauge gives $\nabla\cdot\mathbf{A} = 0$. This ensures that $\mathbf{p}$ commutes with $\mathbf{A}$, so that the perturbation Hamiltonian can be rewritten

$$H' = \frac{e}{m_e}\mathbf{A}\cdot\mathbf{p} + \frac{e^2}{2m_e}A^2. \tag{1.8}$$

The second term from Eq.(1.8) can be neglected as being quadratic and small in the assumed weak interaction between radiation and matter (it describes an interchange of two photons). However, this limits the description to weak radiation and the conclusions will not be valid for an intense laser beam.

Now using this Hamiltonian, the Schrödinger equation can be expanded in terms of stationary states of the atom

$$\Psi = \sum_n c_n \psi_n e^{\frac{-iE_n t}{\hbar}} \tag{1.9}$$

and solved for the probability $|c_j(t)|^2$ that after a time t a transition from the state i to the state j has occurred. It can be shown (e.g. [25]) that the transition rate is proportional to the matrix element

$$\left|\left\langle j\left|\frac{e}{m_e}\widetilde{\mathbf{e}}\cdot\mathbf{p}\mathrm{e}^{i\mathbf{k}\cdot\mathbf{r}}\right|i\right\rangle\right|^2 \tag{1.10}$$

where $\widetilde{\mathbf{e}}$ is the polarization vector.

Further approximations can be done in this matrix element. For wavelengths that are large compared to the size of an atom, the exponent from Eq.(1.10) may be expanded

$$\mathrm{e}^{i\mathbf{k}\cdot\mathbf{r}} = 1 + i\mathbf{k}\cdot\mathbf{r} + \cdots \tag{1.11}$$

which is a good approximation when

$$kr = \frac{2\pi}{\lambda}\cdot\frac{a_0}{Z} = \frac{a_0}{Z\hbar c}(E_j - E_i) < \frac{a_0}{Z\hbar c}\cdot\frac{Z^2e^2}{4\pi\epsilon_0 a_0} = Z\alpha \approx \frac{Z}{137}. \tag{1.12}$$

The first term from Eq.(1.11) leads to the electric dipole approximation of this multipole expansion. This can be illustrated by assuming a polarization along the x-axis of the electric vector and introducing it with the first-order approximation to Eq.(1.10)

$$\left\langle j\left|\frac{e}{m}p_x\right|i\right\rangle = \langle j\,|e\dot{x}|\,i\rangle = \frac{ie}{\hbar}\langle j\,|[H_0,x]|\,i\rangle = \frac{ie}{\hbar}\langle j\,|H_0x - xH_0|\,i\rangle = \frac{i}{\hbar}(E_j - E_i)\langle j\,|ex|\,i\rangle\,. \tag{1.13}$$

This equation represents the matrix element between the stationary states i and j of a component of the electric dipole operator for the atom, which will induce a transition from state i to state j by absorption of electric dipole (E1) radiation polarized along the x-axis.

Similarly, it can be shown that taking the second term from Eq.(1.11) leads to two matrix elements proportional to $\langle j\,|\mu_l|\,i\rangle$, which is a magnetic dipole (M1) moment, and to $\langle j\,|exy|\,i\rangle$ corresponding to an electric quadrupole (E2) moment. The selection rules for these transitions can be worked out using the hydrogenic wave functions (see [25] p. 46 or [26] p. 30) and are summarized in Tab. 1.1.

Table 1.1: Selection rules for allowed (E1) and forbidden (M1, E2) transitions. The assumed coupling is LS; in case of different electron coupling (such as jj) the rules for ΔL and ΔS are not applicable, while the other are considered rigorous.

E1	M1	E2
$\Delta J = 0, \pm 1$ (excl. $0 \to 0$)	$\Delta J = 0, \pm 1$ (excl. $0 \to 0$)	$\Delta J = 0, \pm 1, \pm 2$
$\Delta M_J = 0, \pm 1$	$\Delta M_J = 0, \pm 1$	$\Delta M_J = 0, \pm 1, \pm 2$
(excl. $0 \to 0$ when $\Delta J = 0$)	(excl. $0 \to 0$ when $\Delta J = 0$)	/
$\Delta l = \pm 1$	$\Delta l = 0$	$\Delta l = 0, \pm 2$
$\Delta n =$ any	$\Delta n = 0$	$\Delta n =$ any
parity change	no parity change	no parity change
$\Delta L = 0, \pm 1$ (excl. $0 \to 1$)	$\Delta L = 0$	$\Delta L = 0, \pm 1, \pm 2$ (excl. $0 \to 0, 1$)
$\Delta S = 0$	$\Delta S = 0$	$\Delta S = 0$
example: $1s\,^2S - 3p\,^2P$	example: $^2P_{1/2} - {}^2P_{3/2}$	example: $1s\,^2S - 3d\,^2D$

1.2.2. Fine-structure transitions

The solutions of the Dirac equation for the bound-state energy a single electron in a Coulomb field of a nucleus with a charge Z, like in the case of hydrogen-like heavy ions, can be expressed by the following equation [27]

$$E_{n,j} = \frac{m_e c^2}{\sqrt{(1+Y)}}, \qquad Y = \frac{Z^2\alpha^2}{\left(n - j - \frac{1}{2} + \sqrt{\left(j+\frac{1}{2}\right)^2 - Z^2\alpha^2}\right)^2}, \tag{1.14}$$

where n is the principal quantum number and j the total angular momentum. The energy of an M1 fine-structure transition is then given by the difference $E_{\mathrm{FS}} = \left|E_{n,j} - E_{n,j'}\right|$. The equation gives good results even when taking into account the outermost electron in lighter many-electron ions, where the nuclear charge seen by the outer electron is screened by the lower-lying ones, in which case $Z_{\mathrm{eff}} = Z - N + 1$, where N is the number of electrons. This is shown in Fig. 1.6 for the case of boron-like and carbon-like ions, together with an illustration of similar fine-structure transitions observed by means of emission spectroscopy. Such measurements are several orders of magnitude less accurate than laser spectroscopy experiments, but offer a broad spectrum of detected transitions as possible candidates for precision measurements. It can be seen that the fine-structure transitions in highly charged ions enter the laser accessible region for

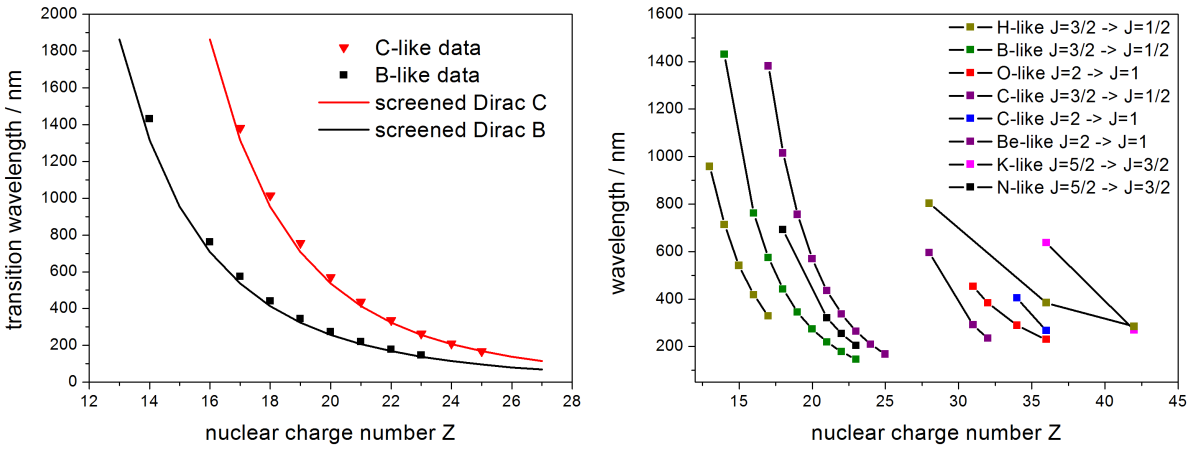

Figure 1.6: On the left: comparison of experimental results and the calculation with the screened Dirac equation for carbon and boron-like ions. On the right: overview of detected fine-structure transitions in highly charged ions with wavelengths accessible with lasers (values taken from [12]). Lines have been added to guide the eye.

$15 < Z < 50$, typically in hydrogen- to nitrogen-like ions. As mentioned above, all are magnetic dipole transitions, i.e. E1 forbidden.

The lifetime τ of an excited state is given by the inverse sum of the rates A_i in all possible decay channels to lower lying levels

$$\tau = \left(\sum A_i\right)^{-1} \tag{1.15}$$

including the forbidden and intercombination transitions. These radiative lifetimes can be very difficult to calculate since they require calculations of electric dipole matrix elements of all possible transitions to lower energy levels. For a specific hydrogenic or quasi-hydrogenic state an approximate semi-classical equation accurate up to a few per cent is given by [28]

$$\tau_{nl} \approx \frac{3\hbar n^5}{2Z^4\alpha^5 m_e c^2} \cdot \frac{l\,(l+1)}{n^2}\,, \qquad n \geq 2,\ l \neq 0, \tag{1.16}$$

while a more accurate equation is beyond the scope of this work and can be found in [29]. Here $\hbar$ is the Planck constant divided by 2π and c is the speed of light. Good results can be achieved by using Eq.(1.16) with Z_{eff} in the same sense as in Eq.(1.14) for highly charged ions with more than one electron.

1.2.3. Hyperfine structure transitions

A nucleus with a non-zero spin $\mathbf{I}$ exibits a nuclear magnetic moment $\boldsymbol{\mu}_I = g_I \mu_N \mathbf{I}$, where g_I is the nuclear g-factor and μ_N is the nuclear magneton. In this case $\mathbf{I}$ and $\mathbf{J}$ couple to the total angular momentum of an atom $\mathbf{F} = \mathbf{I} + \mathbf{J}$ and the relative shift ΔE_{HFS} of this state relative to the unperturbed energy can for hydrogen-like ions be written in the following form [9]

$$\begin{aligned}\Delta E^{1s}_{\text{HFS}} = &\frac{\alpha(\alpha Z)^3}{n^3} g_I \frac{m_e}{m_p} \frac{F(F+1) - I(I+1) - J(J+1)}{2J(J+1)(2L+1)} m_e c^2 \times \\ &\times \left[A^{1s}(\alpha Z)(1-\delta^{1s})(1-\epsilon^{1s}) + \chi_{\text{rad}}\right],\end{aligned} \tag{1.17}$$

where m_p is the proton mass, $A^{1s}(\alpha Z)$ the relativistic correction, δ^{1s} the nuclear charge distribution correction, ϵ^{1s} the nuclear magnetization distribution correction and χ_{rad} the radiative correction. Using Eq.(1.17) the HFS splitting of the $1S_{1/2}$ ground state in hydrogen-like ions can be calculated

$$\begin{aligned}\Delta E^{1s}_{\mathrm{HFS,splitt}} &= \Delta E^{1s}_{\mathrm{HFS}}(F = I + 1/2) - \Delta E^{1s}_{\mathrm{HFS}}(F = I - 1/2) = \\ &= \frac{4}{3}\alpha(\alpha Z)^3 g_I \frac{m_e}{m_p}\frac{2I+1}{2} m_e c^2 \left[A^{1s}(\alpha Z)(1-\delta^{1s})(1-\epsilon^{1s}) + \chi_{\mathrm{rad}}\right].\end{aligned} \tag{1.18}$$

Equation (1.17) can also be applied to the HFS splitting of the $2S_{1/2}$ ground state in lithium-like ions [14]

$$\begin{aligned}\Delta E^{2s}_{\mathrm{HFS,splitt}} =& \frac{1}{6}\alpha(\alpha Z)^3 g_I \frac{m_e}{m_p}\frac{2I+1}{2} m_e c^2 \times \\ &\times \left[A^{2s}(\alpha Z)(1-\delta^{2s})(1-\epsilon^{2s}) + \chi_{\mathrm{rad}} + \frac{B(Z\alpha)}{Z} + \frac{C(Z\alpha)}{Z^2} + \cdots\right]\end{aligned} \tag{1.19}$$

where the same notation is used as in Eq.(1.17), and the terms $B(\alpha Z)/Z$ and $C(\alpha Z)/Z^2$ correspond to the interelectronic interaction corrections in the first and second order, respectively.

As Eqs.(1.18) and (1.19) exhibit, the transition energy is proportional to the third power of the nuclear charge. In terms of wavelength, it scales down from the microwave domain for $Z = 1$ to the optical or near-optical domain for roughly $Z > 50$. Still a strong dependence on the nuclear magnetic moment causes a broad scatter of the transition wavelengths for different isotopes as can be seen in Fig. 1.7. The biggest uncertainty in the calculation is the largely unknown spatial distribution of the nuclear magnetization (Bohr-Weisskopf effect). This actually limits the possibility to extract the QED contribution from the experimental determination of the 1s HFS in hydrogen-like ions. However, it has been pointed out by V. Shabaev and co-workers that a comparison of the HFS in hydrogen- and lithium-like ions offers a possibility to largely cancel the nuclear contributions and represents therefore also a better test of the bound-state QED [30]. Figure 1.7 shows the calculated and measured HFS for these types of highly charged ions within the laser-accessible region.

Provided that the transition wavelength is much larger than the diameter of the ion (which becomes even more pronounced in highly charged ions since $r_{\mathrm{ion}} \sim Z^{-1}$), the magnetic dipole approximation can be used to calculate the transition probability between hyperfine levels. For s-electrons it is given by [14]

$$A_{F\to F'} = \frac{4\alpha\omega^3\hbar^2 I}{27 m_e^2 c^4 (2I+1)} (\Lambda + 1)^2 \tag{1.20}$$

for the ground state of a hydrogen-like ion. Here ω is the transition frequency and Λ a factor defined in [14] representing the ratio of the Dirac energy eigenvalue to the electron energy. It can be seen that the excited state lifetime of a hyperfine level, as defined by Eqs.(1.15) and (1.20), scales with Z^{-9} from $\sim 10^{14}$ s for small atomic numbers to several ms for heavy few-electron ions, allowing sufficiently high fluorescence rates for laser spectroscopy.

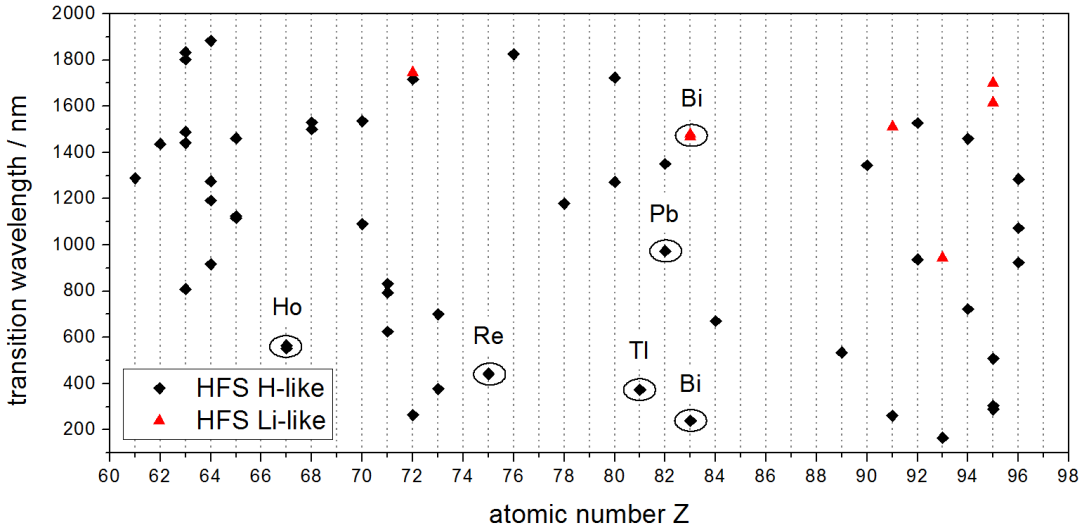

Figure 1.7: Ground-state hyperfine transition wavelengths of stable and long-lived radioactive highly charged ions, calculated according to Eq.(1.17). The figure includes also different isotopes of the same atomic number Z. The encircled ionic species have been experimentally investigated, either in en EBIT or a storage ring. Only the near-UV to near-IR region is shown, since it is typically accessible for precision laser spectroscopy.

1.3. Laser spectroscopy in ion traps

The biggest part of our knowledge about the internal structure of atoms and molecules comes from spectroscopic methods, out of which laser spectroscopy is an important asset. It has led to advances in the precision and accuracy with which electron level energies can be measured, and this has fundamental importance for the understanding of basic atomic processes. The measured transition wavelength can serve as a probe for models of the atom, while the excited state's lifetime, extracted from the transition's natural linewidth, can improve the accuracy of many-electron theoretical calculations. Unless Doppler-free spectroscopic techniques are applied, the sensitivity of this type of measurements is typically limited by the velocity distribution, i.e. the temperature of the sample under investigation.

Ion traps offer the possibility to have a well defined ensemble of particles, spatially confined within the laser interaction region. This extended sampling time enables measurements of even very slow (forbidden) transitions, which would not be accessible by other methods. Additionally, an ion trap allows various ion cooling schemes to be implemented, significantly reducing the Doppler width of the observed transition.

In that sense, classical laser spectroscopy is done by exciting the ground state transition in the ion of interest and observing the spontaneously emitted fluorescence photons from the excited state. This section will define several terms and concepts related to that technique, which are used throughout this work.

1.3.1. Laser induced fluorescence spectroscopy

If the laser wavelength is precisely tuned to the energy difference $E_i - E_j$ of the transition of interest, the number of absorbed photons per second n_a is expressed as

$$n_a = N_i \phi_L \sigma_{ij} \tag{1.21}$$

where N_i is the number of non-excited particles, ϕ_L the laser photon flux per cm^2 per second and σ_{ij} the resonant absorption cross section. It should be noted that N_i is in general itself dependent on n_a, and Eq.(1.21) is an approximation for small transition rates, i.e. a small product of the cross-section and the photon flux. The number of emitted fluorescence photons per second is given by [31]

$$n_f = N_j A_j = N_j 2\pi\Delta\nu \tag{1.22}$$

where N_j is the number of excited particles and A_j the transition probability, directly related to the natural linewidth $\Delta\nu$, i.e. lifetime of the exited state $|j\rangle$, as discussed in sections 1.2.2 and 1.2.3. Under steady-state conditions, the number of fluorescence photons emitted into the full solid angle of 4π will be equal to the number of absorbed photons. However, only a fraction of the fluorescence photons are collected by the detector, which defines the *detection solid angle* Ω and the *spatial detection efficiency* $F = \Omega/4\pi$. The fraction of fluorescence photons entering the detector that produce secondary electrons and lead to a sufficiently strong pulse for amplification defines the *quantum efficiency* of the detector. Typically, the largest sensitivity is achieved in the visible and UV part of the optical spectrum. Quantum efficiency drops rapidly for infrared photons, while the detectors' dark-count rate increases.

If the excited transition is not a part of a true two-level system, i.e. decay from the level $|j\rangle$ does not only èead back to $|i\rangle$, so-called *electron shelving* in dark states can be a serious problem for the desired measurement. In the example of a three level system, it takes place when the excited state has a non-vanishing decay channel to an intermediate level which either cannot decay back to the lower one, or has a very long lifetime. After a while, all excited electrons are "shelved" on it, rendering the system dark (without fluorescence photons). It can be avoided by re-pumping the electrons from the dark state back into the exited state, from where they can again decay also to the lower level.

1.3.2. Broadening of spectral lines

If an excited energy level has a lifetime τ_0, its energy can only be determined with an uncertainty of $\Delta E = \hbar/\tau_0$ according to the uncertainty principle. This translates to a frequency uncertainty for the transition to the lower (stable) level

$$\Delta\omega = \frac{\Delta E}{\hbar} = \frac{1}{\tau_0}. \tag{1.23}$$

If both of these states have a finite lifetime, both energy uncertainties have to be taken into account. In this work, however, only ground-state transitions are considered.

Equation (1.23) defines the *natural linewidth* of an atomic or a molecular transition. However, typically it cannot be observed without special techniques because it will be covered by line-

broadening effects. One of the major contributions arises from the non-zero thermal velocity of the absorbing and emitting particles, which results in Doppler broadening of spectral lines.

If one assumes a Maxwellian velocity distribution in the observed sample, the Doppler broadened linewidth can be expressed as [31]

$$\frac{\Delta\nu_D}{\nu_0} = 2\sqrt{\ln 2}\,\frac{u}{c}\,; \qquad u = \sqrt{\frac{2k_BT}{m}} \tag{1.24}$$

where k_B is the Boltzmann constant and u the most probable velocity for atoms (ions) of mass m at temperature T. The calculated values for $T = 10$ K are roughly 250 MHz for lighter atoms ($M \approx 50$ amu) and 100 MHz for heavier ones ($M \approx 200$ amu).

As mentioned in the previous chapter, even in a true two-level system the fluorescence rate does not increase linearly with increasing laser power but rather saturates. This happens because at maximum half of the population can be transferred into the upper state. The relevant parameter describing the saturation curve is called the *saturation intensity* and can be expressed as [26]

$$I_{\text{sat}} = \frac{\pi}{3}\frac{hc}{\lambda_0^3\tau_0}, \tag{1.25}$$

where h is the Planck constant and λ_0 the transition wavelength. In case of Mg^+ the relevant parameters are $\lambda_0 = 280$ nm and $\tau_0 = 4$ ns. Thus, the saturation intensity is $I_{\text{sat}}^{\text{Mg}} = 2.4\ \text{mW/mm}^2$, a typical value for a strong resonance transition in alkaline and alkaline earth ions.

Equation (1.25) is valid if the excitation wavelength λ is tuned to the centre of the resonance, where the interaction cross-section is largest. Another contribution to the observed transition linewidth comes from the fact that saturation already limits absorption close to the resonance, while off-resonance the saturation is much smaller [26]. With increasing laser intensity, saturation is also reached in the resonance wings, and the line becomes broader. This can also be also understood as caused by the reduced lifetime of the excited state because of induced emission [31], which becomes significant above the saturation intensity. The resulting linewidth is given by

$$\Delta\nu_{\text{FWHM}} = \frac{1}{2\pi\tau_0}\sqrt{1 + \frac{I}{I_{\text{sat}}}} \tag{1.26}$$

and is also known as *power broadening*.

There are additional spectral line-broadening mechanisms, like *pressure broadening* and *transit-time broadening*, but for typical ion trap experiments they are less important and not considered in this work.

Chapter 2

Ion storage, detection and cooling in a Penning trap

Ion trapping as an experimental technique emerged from studies of electrical discharges in 1923 by K.H. Kingdon [32] and 13 years later by F.M. Penning, who did the same in the presence of magnetic fields [33]. The idea was further developed by J.R. Pierce by combining magnetic fields with hyperbolical electrodes [34], and by H.G. Dehmelt who studied ion traps in detail [35]. A trap where radial confinement is achieved with a magnetic field and axial with an electrostatic field became known as a *Penning trap*. The theory of charged particle confinement and ion eigenmotions in a Penning trap is summarized in section 2.1. A special version of the trap is the open *cylindrical* form, which allows better access than the classical closed hyperbolical type. This property is very important for the SpecTrap experiment, since it allows injection of both externally produced ions and laser beam(s) into the trap. Imperfections of the electrical and magnetic fields which are present in every real Penning trap and their consequences are described in section 2.1.4.

The first experimental results on spectroscopy of heavy highly charged ions came from electron beam ion traps (EBITs) [36, 37] and storage rings [5, 6] some 20 years ago, but their precision was limited due to large transition Doppler widths and the uncertainty of the ion velocity. It was soon realized that combining ion traps with laser spectroscopy provided significant advantages: the trapped ions can be cooled to very low temperatures (i.e. motional energies), reducing the Doppler broadening. Additionally, extended trapping times allow measurements of even very slow transitions. To that end, Penning traps could in principle be built very large (i.e. with a large space charge limit) in order to accommodate the required amount of ions. Because of these unique properties, Penning traps are nowadays widely used for precision mass measurements [38], g-factor determinations [39] and laser spectroscopy [40]. The latter, in particular laser spectroscopy of trapped highly charged ions, is the main goal of the SpecTrap experiment.

After an introduction to the basics of ion trapping, the following sections will describe destructive (section 2.2) and non-destructive (section 2.3) ion detection methods. They are both required to establish stable ion trapping of externally produced ions. Very high sensitivity can be reached especially in the case of passive tuned-circuit image current detection. The technique

is inevitably followed by dissipation of the trapped ions' energy, which leads to ion cooling and in particular resistive cooling. This technique is suitable for trapped ion cooling down to a few K, and for reaching even lower temperatures laser Doppler and sympathetic cooling have to be applied. All these methods are implemented at SpecTrap, and by a conjunction of several cooling methods almost any ion species can be brought to sub-K temperatures, where the smaller Doppler broadening makes laser spectroscopy measurements on highly charged ions several orders of magnitude more accurate than in previous work.

2.1. Principles of charged particle confinement

In order to confine a charged particle within a limited volume a minimum of the potential energy E has to be produced at a point in space. Only in that case the net force $\mathbf{F}$ acting on the particle will always be directed towards that point. Thus

$$\mathbf{F} = -\gamma \mathbf{r}; \qquad \mathbf{F} = -\boldsymbol{\nabla} E \tag{2.1}$$

where $\gamma > 0$ is a constant and $\mathbf{r}$ the radius vector. Assuming a charge q, this results in a harmonic potential V

$$V = \frac{E}{q} = \frac{\gamma}{2q} r^2 = \frac{\gamma}{2q}(Ax^2 + By^2 + Cz^2) \tag{2.2}$$

with A, B and C as arbitrary coefficients. The potential (2.2) has to satisfy Laplace's equation $\Delta V = 0$, which means that $A + B + C = 0$. With a choice of $A = B = -1$ and $C = 2$ one gets a hyperbolic potential in cylindrical coordinates

$$V = \frac{\gamma}{2q}(2z^2 - r^2). \tag{2.3}$$

Because of the different signs of the radial and axial part it is obvious that the potential exhibits a saddle and not an extreme in the point of origin. This means that it is not possible to achieve three-dimensional confinement using only electrostatic fields[1]. In order to do so one has to combine the electrostatic potential either with a static axial magnetic field, creating a *Penning trap*, or with a high frequency alternating electric quadrupole field, creating a *Paul trap*. A typical hyperbolic trap that provides the potential (2.3) consists of three revolving hyperboloids, commonly named the ring electrode and two endcap electrodes, as shown in Fig. 2.1.

The constant γ can be determined by the way in which the voltage is applied to the electrodes. If it is done symmetrically, e.g. $+V_0/2$ to the endcaps and $-V_0/2$ to the ring, γ becomes

$$\gamma = \frac{2V_0 q}{2z_0^2 + r_0^2} = \frac{V_0 q}{2d^2}; \qquad d = \sqrt{\frac{1}{2}\left(z_0^2 + \frac{1}{2} r_0^2\right)} \tag{2.4}$$

resulting in the potential

$$V = \frac{V_0}{4d^2}(2z^2 - r^2). \tag{2.5}$$

The constant d, usually introduced for easier calculation and discussion, is referred to as the *trap dimension*.

[1] Which is also given by Earnshaw's theorem - an electrostatic potential cannot have a minimum in free space.

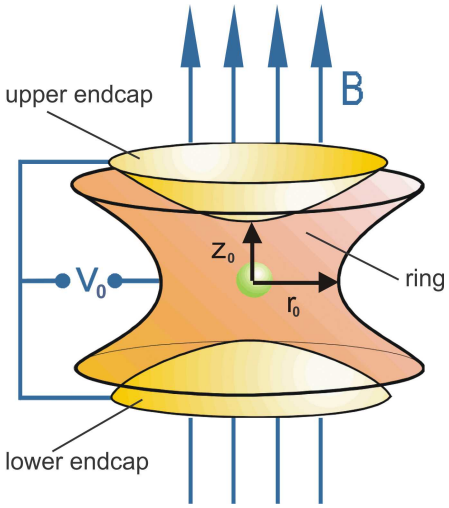

Figure 2.1: Typical electrode configuration that creates a quadrupole potential. The direction of the magnetic field in case of a Penning trap is also indicated.

2.1.1. Particle motion inside a Penning trap

A typical Penning trap is made by combining a homogeneous magnetic field $\mathbf{B} = (0, 0, B_0)$ and an electric field $E = -\nabla V$ derived from (2.5). Therefore, a particle with mass m, charge q and velocity $\mathbf{v} = (v_x, v_y, v_z)$ experiences a force

$$\mathbf{F} = -q\boldsymbol{\nabla} V + q(\mathbf{v} \times \mathbf{B}). \tag{2.6}$$

This results in three equations of motion written in Cartesian coordinates as follows

$$\frac{\mathrm{d}^2 x}{\mathrm{d}t^2} - \omega_c^2 \frac{\mathrm{d}y}{\mathrm{d}t} - \frac{1}{2}\omega_z^2 x = 0 \tag{2.7}$$

$$\frac{\mathrm{d}^2 y}{\mathrm{d}t^2} + \omega_c^2 \frac{\mathrm{d}x}{\mathrm{d}t} - \frac{1}{2}\omega_z^2 y = 0 \tag{2.8}$$

$$\frac{\mathrm{d}^2 z}{\mathrm{d}t^2} + \omega_z^2 z = 0 \tag{2.9}$$

where the *unperturbed cyclotron* and *axial* frequency, respectively, are defined

$$\omega_c = \frac{qB_0}{m} \tag{2.10}$$

$$\omega_z = \sqrt{\frac{qV_0}{md^2}}. \tag{2.11}$$

It is obvious that the motion in the z direction is a simple harmonic motion characterized by a frequency ω_z and decoupled from the motions in x and y directions. These equations have analytical solutions [41] stating that the radial motion consists of two superimposed oscillation frequencies given by

$$\omega_+ = \frac{\omega_c}{2} + \sqrt{\left(\frac{\omega_c}{2}\right)^2 - \frac{\omega_z^2}{2}} \tag{2.12}$$

$$\omega_- = \frac{\omega_c}{2} - \sqrt{\left(\frac{\omega_c}{2}\right)^2 - \frac{\omega_z^2}{2}} \tag{2.13}$$

usually called the *reduced cyclotron* and the *magnetron drift* frequency, respectively. It should be noted that ω is the angular velocity, while the corresponding frequency is given by $\nu = \omega/2\pi$,

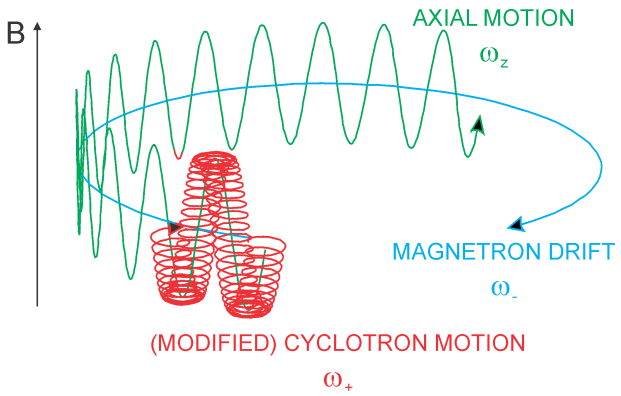

Figure 2.2: An overview of the combined typical three particle motions inside a Penning trap. It should be noted that in an ideal trap the amplitudes are independent from each other and can thus significantly differ from what is shown.

although the terminology is often used ambiguously. Fig. 2.2 shows the three typical motions combined with arbitrary amplitudes.

Since the derivation was purely classical, the question arises if such a treatment is justified from the quantum mechanical point of view. The values to be considered for SpecTrap and highly charged ions are $\omega_z = 2\pi \cdot 1$ MHz and $\omega_+ = 2\pi \cdot 21$ MHz, derived from $d = 6.9$ mm, $\tilde{m}/\tilde{q} = 3$, $V_0 = 200$ V and $B_0 = 4$ T. Therefore the fastest motion with the ω_+ frequency corresponds to the quantum energy $\hbar\omega_+ \approx 10^{-7}$ eV. This value is more than three orders of magnitude smaller than the thermal energy assigned to an ion at liquid helium temperature 4 K, given by $E = k_B T \approx 4 \cdot 10^{-4}$ eV. This means that the ion would have a quantum number of several thousand, which justifies a non-quantum-mechanical approach. Extensive studies on that topic can be found in [41, 42].

Several useful relations between the mentioned motional frequencies exist in absence of geometrical imperfections of the trap electrodes [41]

$$\omega_+ + \omega_- = \omega_c \tag{2.14}$$

$$2\omega_+\omega_- = \omega_z^2 \tag{2.15}$$

$$\omega_+^2 + \omega_-^2 + \omega_z^2 = \omega_c^2. \tag{2.16}$$

The last equation is known as the *invariance theorem*. It should be noted that in an ideal trap the energies, i.e. amplitudes, of different motions are unrelated to each other, meaning that one can address them independently without disturbing the others.

Equations (2.12) and (2.13) can be used to estimate the maximum charge-to-mass ratio of particles that can be stored in the trap. In order to keep the harmonic oscillation, the term under the root has to remain positive which is fulfilled when

$$\frac{\tilde{m}}{\tilde{q}} \leq \frac{B_0^2 d^2 e}{2 V_0 m_p} = 2.35 \cdot 10^3 \frac{B_0^2}{V_0} \left[\frac{\mathrm{V}}{\mathrm{T}^2}\right] \approx 80 \tag{2.17}$$

where $\tilde{m}$ and $\tilde{q}$ are the mass and charge number, respectively, m_p the proton mass and e the elementary charge. The value 80 was calculated for $B = 4$ T, $d = 6.9$ mm and $V_0 = 500$ V, and it covers almost all but the heaviest singly charged ions.

Since electric and magnetic field imperfections are always present, the ω_+ and ω_- frequencies will deviate from their ideal form given by Eqs.(2.12) and (2.13) [42]. One can take advantage of this by deliberately implementing a well defined electric anharmonicity or magnetic inhomogeneity, which in turn induce controllable frequency shifts and energy transfers between different particle motions [40].

2.1.2. Space charge effects

The equations discussed in the previous section apply to a *single* charged particle in a trap. However, for spectroscopy purposes it is favourable to have an ion cloud, i.e. a large number of stored ions in order to achieve higher fluorescence rates. In that case the positive potential of the ion cloud reduces the effective trapping potential. A given ion will feel the average space charge field acting on it from the other ions and its axial frequency will stay harmonic but with a downward shift [41]

$$\omega_z' = \omega_z \sqrt{\left(1 - \frac{\omega_p^2}{3\omega_z^2}\right)} \tag{2.18}$$

where $\omega_p = \sqrt{\frac{q^2 n}{\epsilon_0 m}}$ is the plasma frequency (n is the ion density). A similar equation is valid also for the radial frequencies, but it is for SpecTrap less important. It should be noted that the centre-of-charge motion cannot be affected that way. Additional to this shift, which can be compensated with a higher trapping potential, space charge effects will broaden the distribution of oscillation frequencies and lower the ion cloud density.

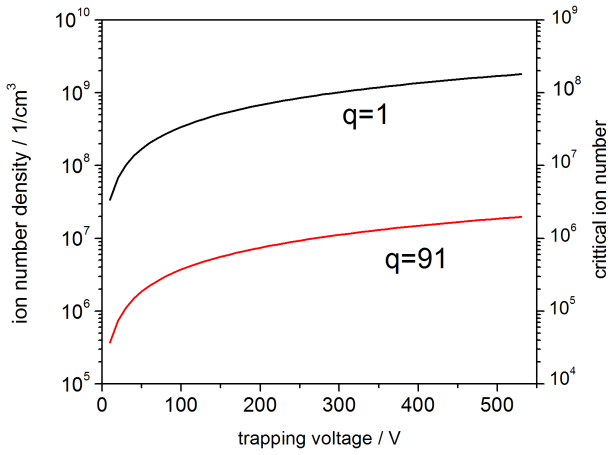

Figure 2.3: Critical ion density and total number calculated according to Eq.(2.19) for a trap with $d = 7$ mm, as considered in this work. Two curves show results for singly charged (black) and multiply charged ions (red). The right-hand side scale shows the corresponding maximum ion number inside a 5 mm ion cloud.

The maximum ion density is reached when the square root in Eq.(2.18) becomes zero. It effectively means loss of axial confinement and is given for ion densities higher than

$$n = \frac{3\epsilon_0 V_0}{q d^2}. \tag{2.19}$$

This equation should be taken rather as an approximation than a sharp threshold since it represents an extreme case - typically, particle motion will become unstable considerably before reaching it. Figure 2.3 shows the critical ion density as a function of trapping voltage, for singly

charged (black) and highly charged ions (red) inside a Penning trap with $d = 7$ mm. The maximum ion number in a spherical cloud of about 5 mm diameter is also given.

2.1.3. Open-endcap cylindrical Penning Trap

Although Penning traps with hyperbolic electrodes produce the electric quadrupole potential necessary for particle confinement, for experimental applications their closed geometry has several disadvantages:

- it is difficult to inject particles or direct laser radiation into the trap
- vacuum pumping is hindered
- the hyperbolic electrodes are very difficult to machine.

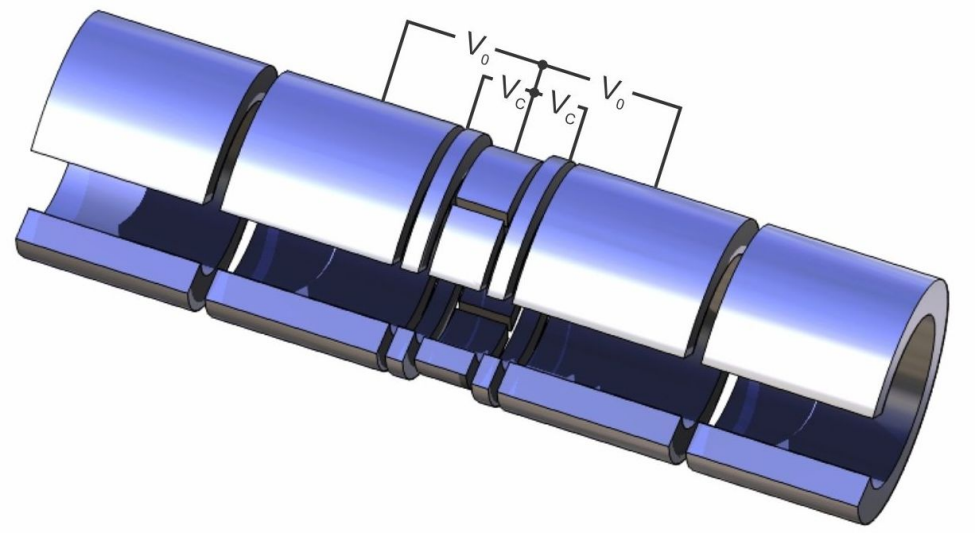

Figure 2.4: An illustration of a cylindrical trap. The central electrode is the ring, segmented into four parts to allow electronic coupling of the ions' radial motion to the trap. The ring sets the trapping potential, i.e. the endcap potential V_0 and the correction potential V_c are defined with respect to it. In the presented example the voltages are applied symmetrically, which generally does not have to be the case. One can also add more electrodes behind the endcaps, as in this case, which could be used for capturing externally produced ions.

For the price of a slightly less harmonic potential, these problems can be solved by replacing the hyperbolic endcaps with open, extended cylindrical electrodes. As it turns out, the potential in the trap can still be calculated analytically [43], and it is easier to tune and align such a trap. The imperfections can be compensated using an additional set of correction electrodes [43], as shown in Fig. 2.4. In order to calculate them, it is useful to express the electric potential in the centre of a Penning trap in terms of Legendre polynomials P_k

$$V = \frac{1}{2} V_0 \sum_{k=0}^{\infty} C_k \left(\frac{r}{d}\right)^k P_k(\cos\theta); \qquad k = \text{even} \tag{2.20}$$

where C_k are the expansion coefficients of the $P_k(\cos\theta)$ chosen because of cylindrical symmetry and all other variables are as defined in previous chapters. Only even values for k are considered because of the $z = 0$ plane symmetry.

If a potential V_c is applied to the correction electrodes, it will be superimposed in the centre of the trap to the already present endcap potential V_0

$$V = V_0\phi_0 + V_c\phi_c \tag{2.21}$$

where ϕ_0 and ϕ_c are solutions of Laplace's equation, expanded near the trap centre as

$$\phi_0 = \frac{1}{2}\sum_{k=0}^{\infty} C_k^{(0)} \left(\frac{r}{d}\right)^k P_k(\cos\theta) \tag{2.22}$$

$$\phi_c = \frac{1}{2}\sum_{k=0}^{\infty} D_k \left(\frac{r}{d}\right)^k P_k(\cos\theta) \tag{2.23}$$

making the C_k coefficients from Eq.(2.20)

$$C_k = C_k^{(0)} + D_k\frac{V_c}{V_0}. \tag{2.24}$$

The factors $C_k^{(0)}$ and D_k can be calculated using [43]

$$C_k^{(0)} = \frac{(-1)^{k/2}}{k!}\frac{\pi^{k-1}}{2^{k-3}}\left(\frac{d}{z_o+z_e}\right)^k \sum_{n=0}^{\infty}(2n+1)^{k-1}\frac{A_n^{(c)}}{J_0(ik_nr_0)} \tag{2.25}$$

$$D_k = \frac{(-1)^{k/2}}{k!}\frac{\pi^{k-1}}{2^{k-3}}\left(\frac{d}{z_o+z_e}\right)^k \sum_{n=0}^{\infty}(2n+1)^{k-1}\frac{A_n^{(d)}}{J_0(ik_nr_0)} \tag{2.26}$$

$$A_n^{(c)} = \frac{1}{2}\left((-1)^n - \sin k_n z_0 - \sin\left(k_n(z_0 - z_c)\right)\right) \tag{2.27}$$

$$A_n^{(d)} = \sin(k_n z_0) - \sin(k_n(z_0 - z_c)) \tag{2.28}$$

where z_e is the length of the endcap electrodes, z_c the length of the correction electrodes and J_0 the zeroth-order Bessel function.

The lowest term of Eq.(2.20) associated with the C_0 coefficient is just a constant and is irrelevant for this discussion. In a perfect quadrupole potential the next term, C_2, is 1, and all other terms are zero. In that sense the axial frequency from Eq.(2.11) is

$$\omega_z^2 = \frac{qV_0}{md^2}C_2. \tag{2.29}$$

This axial oscillation becomes anharmonic if the next term $C_4 \neq 0$. In a cylindrical Penning trap this term is usually far from zero, but it can be compensated by choosing a proper ratio of voltages and electrode sizes used in Eqs.(2.24)-(2.28). All higher-order terms are much less important since they scale with a factor larger than $(r/d)^2$.

The so-called "orthogonalized" Penning trap is achieved by choosing the ratio r_0/z_0 in such a way that also the D_2 coefficient vanishes. In that case the C_2 coefficient from Eq.(2.24) does not depend on the voltage V_c (required to remove C_4), which simplifies the tuning of the trap. Since this can be achieved for any size of the correction electrode, one still has the freedom to choose z_c/z_0. This can be used to additionally remove even the C_6 term simultaneously with the C_4 term.

2.1.4. Electric and magnetic field inhomogeneities

In an ideal Penning trap the ion oscillation frequencies $\omega_{z/+}$ are independent of the energies $E_{z/+}$, i.e. the amplitudes of the ions' motion. However, in a real Penning trap, especially in the case of a cylindrical Penning trap, there are some residual electric and magnetic field inhomogeneity, and frequencies and amplitudes are no longer independent. Of experimental interest are usually the frequencies ω_z and ω_+ defined by Eqs.(2.29) and (2.12), respectively.

In the case of electric imperfections, the main contribution to the frequency-amplitude dependence comes from the non-vanishing C_4 term from Eq.(2.24). If it is removed as discussed above, it can be shown [40] that the relative frequency shift is given with

$$\begin{pmatrix} \Delta\omega_+/\omega_+ \\ \Delta\omega_z/\omega_z \end{pmatrix} = \frac{6C_4}{qU_0} \begin{pmatrix} \frac{1}{4}(\omega_z/\omega_+)^4 & -\frac{1}{2}(\omega_z/\omega_+)^2 \\ -\frac{1}{2}(\omega_z/\omega_+)^2 & \frac{1}{4} \end{pmatrix} \begin{pmatrix} E_+ \\ E_z \end{pmatrix}. \tag{2.30}$$

Similarly as in the case of the electrostatic potential V from Eq.(2.20), the magnetic field $B_z = B_z(r,z)$ can be expanded in a Taylor series with the coefficients

$$B_k = \frac{1}{k!}\frac{\partial^k}{\partial z^k} B_z(r,z). \tag{2.31}$$

The most important term of the expansion is B_2, and the axial magnetic field can be written as

$$B_z = \left[B_0 + B_2 \left(z^2 - \frac{r^2}{2} \right) \right], \tag{2.32}$$

while the radial magnetic field, being many orders of magnitude smaller, can be safely disregarded. The corresponding frequency shift then takes the form [40]

$$\begin{pmatrix} \Delta\omega_+/\omega_+ \\ \Delta\omega_z/\omega_z \end{pmatrix} = \frac{1}{m\omega_z^2}\frac{B_2}{B_0} \begin{pmatrix} -(\omega_z/\omega_+)^2 & 1 \\ 1 & 0 \end{pmatrix} \begin{pmatrix} E_+ \\ E_z \end{pmatrix}. \tag{2.33}$$

The presence of a non-vanishing B_2 term results in a so-called "magnetic bottle" shape of the magnetic field. In that configuration the invariance theorem is no longer valid, and as it can be seen from Eq.(2.33), both frequencies become dependent on the amplitudes, i.e. the motional energies. This leads to mixing of different motions, which is very important for the interpretation of experimental results, e.g. ion cooling in one degree of freedom results in a simultaneous cooling of the other ones. There are experimental techniques that take advantage of a deliberate B_2 term, like the continuous Stern-Gerlach effect for observations of a spin-flip of electrons bound to highly charged ions [44], but they are beyond the scope of this work.

2.2. Destructive ion detection

Depending on the way they interact with a particle, one can generally speak of destructive and non-destructive ion detectors. As the name suggests, the destructive ion detection techniques completely destroy the investigated ion cloud and a new one has to be loaded. The destructive detectors used in SpecTrap are

- secondary electron multipliers, biased with high negative voltage, capable of counting single ions with exact timing information

- current pick-up electrodes, or Faraday cups, normally on ground potential, measuring the current of a continuous ion beam.

A continuous dynode electron multiplier like a channeltron® is a single-channel secondary electron multiplier, as illustrated in Fig. 2.5. For detection of positive ions the input is generally at a negative potential of 1200 to 3000 volts and the output is at ground [45]. The high negative voltage attracts an ion which creates one or more electrons upon impact. These electrons are further accelerated by a voltage drop along the tube. They strike the channel walls, producing additional electrons until at the output a pulse of 10^7 to 10^8 electrons emerges. This pulse can be detected for each ion impact, amplified, discriminated and counted with a scaler.

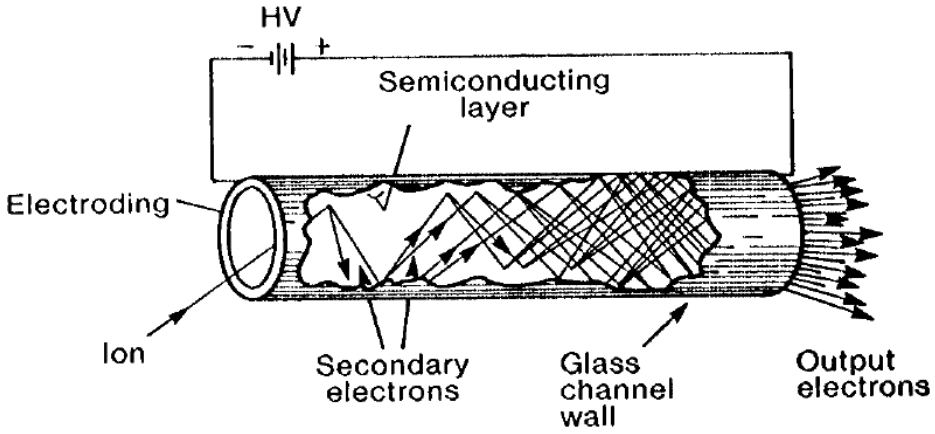

Figure 2.5: The operation principle of a straight channel electron multiplier. An ion incident on the surface of the detector creates an electron avalanche which can be picked up as a pulse on the other end of the tube. Picture reproduced from [45].

A micro channel plate (MCP) shares the same basic work principle as a channeltron®. It comprises many miniature electron multipliers oriented parallel to one another and distributed over an active area typically a few centimetres in diameter. Typical channel diameters range between 10 and 100 μm with length-to-diameter ratios of 40-100. Parallel electrical contact between channels is provided by a thin metal coating on the front and rear surfaces of the MCP, which serves then as an input and output electrode, respectively. Such micro channel plates typically have an amplification factor of around 10^4, which can be further increased by making stacks of two plates on top of each other, as depicted in Fig. 2.6.

Unlike a channeltron® which only counts particles, an MCP can offer additional spatial information about the incident ion beam. This can be provided by a phosphorous imaging screen, a so-called wedge-stripe diode or a resistive plate.

The time resolution of these detection methods is limited by the detectors' dead time. The width of each pulse on a channeltron® or an MCP is around 10 ns. Therefore, the highest theoretically possible ion flux is 10^8 particles/s or 100 MHz. In reality and under non-ideal conditions a pulse will be longer, additional relaxation time is required for stable operation and a channeltron® will show significant saturation already around 3 MHz. Due to a large number of channels, MCPs can have higher count rates, but typically not larger than 20 MHz.

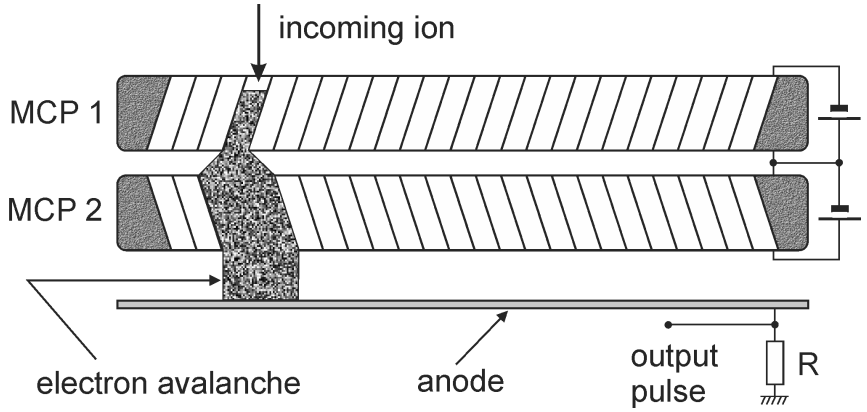

Figure 2.6: The operation principle of two micro channel plates in a Chevron arrangement. An incident ion creates an electron avalanche on several neighbouring channels, providing a pulse for counting and additional spatial information.

Because of their limited maximal count rate, secondary electron multipliers cannot be used for very intense ion beams. In that case a conductive plate or cup designed to catch charged particles can be used instead. It is popularly called *Faraday cup*. When an ion hits the plate the additional charge has to be balanced and an electron flowing from a connected reservoir (e.g. ground) represents a current I, which can be detected with a sensitive device. For a continuous beam of singly charged ions the number of incident ions per second can easily be calculated using

$$\dot{N} = \frac{I}{e}. \tag{2.34}$$

Alternatively, an ion signal from a Faraday cup can be recorded by discharging the plate through a resistor and measuring the corresponding voltage drop.

2.3. Non-destructive ion detection

Contrary to the destructive techniques, it is also possible to detect trapped charged particles by observing their interaction with the surrounding electrodes. However, although the process does not destroy the ions, it does introduce or extract energy from the system, giving the basis for *resistive cooling*.

This non-destructive method of trapped charged particle detection is basically noise pick-up, and it is highly sensitive to other noise sources. In order to have the best possible signal-to-noise ratio, it is best done with a resonant circuit and an overview of the theory behind resonant circuits is given in section 2.3.1. When in resonance, a large impedance for the given resonance frequency will maximize the picked-up signal, and a small impedance at all other frequencies will damp the background noise level.

The ion axial oscillation given by Eq.(2.11) can then be tuned to a desired resonant frequency by changing the voltages across the endcaps. An effective way to decouple the signal from the background noise is to perform a Fourier transform of the voltage measured across the resonant circuits (this technique became known as Fourier Transform Ion Cyclotron Resonance or FT-ICR). In fact, as can be seen from Eqs.(2.11), (2.12) and (2.13), for a given trapping voltage all

ion eigenfrequencies will depend on the q/m ratio. Therefore, a Fourier analysis of the signal will directly correspond to different masses or charge states of trapped ions. A detailed study can be found in [46]. It should be noted at this point that FT-ICR is a special technique of mass spectrometry, and it does not necessarily need to be coupled with resonant detection.

2.3.1. Theory of resonant circuits

Electronic resonant circuits are explained in detail in many textbooks [47, 48], and here only the relevant results are summarized. For convenience, the complex representation of voltages and currents is chosen, giving Ohm's law the same basic form $V(\omega) = I(\omega) \cdot Z(\omega)$ for both DC and AC signals, with the complex and frequency dependent impedance $Z(\omega)$ and voltage $V(\omega) = V_0 e^{i\omega t}$. Hence, the impedance of a capacitance C and an inductance L are

$$Z_C = \frac{1}{\mathrm{i}\omega C} \qquad \text{and} \qquad Z_L = \mathrm{i}\omega L, \tag{2.35}$$

respectively.

A circuit that consists of a capacitor C and an inductance L is called a resonant or an LC circuit. It can be shown that the current flowing through these elements behaves as a harmonic oscillator with a frequency ω. According to the rules of serial and parallel circuits, the equivalent impedance of a series LC circuit is

$$Z_{LC}^{(s)} = \mathrm{i}\left(\omega L - \frac{1}{\omega C}\right) \tag{2.36}$$

whereas in case of a parallel circuit it is

$$Z_{LC}^{(p)} = \mathrm{i}\left(\frac{1}{\omega L} - \omega C\right)^{-1}. \tag{2.37}$$

Obviously, on the resonant frequency

$$\omega_{LC} = \frac{1}{\sqrt{LC}} \tag{2.38}$$

the impedance becomes extreme and approaches zero or infinity for serial or parallel circuits, respectively.

In an ideal resonant circuit there is no energy loss and the current-voltage oscillation can proceed indefinitely once it has been initiated. In realistic circuits the energy is slowly dissipated and the oscillation is damped through internal resistances and other dissipative effects. The impedance of a serial circuit is then given by

$$Z_{RLC}^{(s)} = R + \mathrm{i}\left(\omega L - \frac{1}{\omega C}\right) \tag{2.39}$$

and of a parallel circuit by

$$Z_{RLC}^{(p)} = \left[\frac{1}{R} + \mathrm{i}\left(\omega C - \frac{1}{\omega L}\right)\right]^{-1} \tag{2.40}$$

which means that at the resonant frequency given by Eq.(2.38) the current does not diverge, but is rather dissipated on the resistance R, preventing a zero impedance condition. Diagrams of the fundamental parallel and serial RLC circuits are shown in Fig. 2.7.

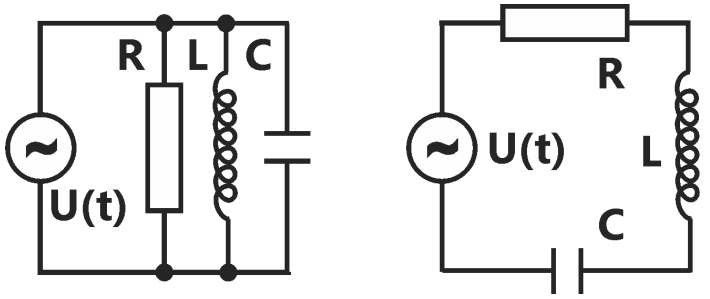

Figure 2.7: Circuit diagrams of basic RLC circuits in the parallel (left) and serial version (right).

According to Eq.(2.39), a current $I(t) = I_0 e^{-\mathrm{i}\omega t}$ leads to a voltage drop across the circuit which is given by

$$U(t) = I(t) Z_{RLC}^{(s)} = I_0 e^{-\mathrm{i}\omega t} \left[R + \mathrm{i} \left(\omega L - \frac{1}{\omega C} \right) \right] = RI(t) + L \frac{\mathrm{d}I(t)}{\mathrm{d}t} + \frac{1}{C} \int I(t) \mathrm{d}t. \tag{2.41}$$

The relative losses inside these elements are quantified by the *quality factor* Q. In case of a capacitor in a parallel circuit, it is defined as the ratio between the ohmic resistance (for instance R_C from the leakage model of the capacitor) and the capacitive resistance given by Eq.(2.35). Similarly, the quality factor of an inductor is given by the ratio of the ohmic resistance R_L to its inductive reactance

$$Q_C^{(p)} = R_C \omega C \qquad \text{and} \qquad Q_L^{(p)} = \frac{R_L}{\omega L}. \tag{2.42}$$

For a serial circuit there is a similar expression

$$Q_C^{(s)} = \frac{1}{R_C \omega C} \qquad \text{and} \qquad Q_L^{(s)} = \frac{\omega L}{R_L}. \tag{2.43}$$

A resonant circuit will be damped by losses in both of these elements, and it is convenient to represent those losses with a combined ohmic resistance R added to the circuit. The quality factor of an RLC resonant circuit is then expressed as the ratio between the total stored energy and the consumed energy per cycle. Since both the inductor and the capacitor should have the same impedances in resonance, the unloaded quality factor of a parallel circuit is given by

$$Q = R \omega_0 C = \frac{R}{\omega_0 L}. \tag{2.44}$$

The term unloaded indicates that no external load was added to the circuit, although it generally does not need to be the case. The way the quality factor scales with resistance is illustrated in Fig. 2.8.

An alternative way of expressing the quality of a resonant circuit is in terms of *bandwidth*. It is done by replacing the absolute current scale from the left part in Fig. 2.8 by the relative current scale. All peak currents are then normalized to 1 and only their relative drops considered. The bandwidth is defined as the frequency spread between the two points where the amplitude drops to $1/\sqrt{2}$ or -3 dB of its peak value since the power $P = RI^2$ at these points is exactly half the maximum power at resonance. For $Q \gg 10$, which is typically the case in ion resonant detection and discussed in the next sections, the curves from Fig. 2.8 can be considered to be symmetric and the bandwidth can be calculated as

$$\Delta f = \frac{f}{Q}. \tag{2.45}$$

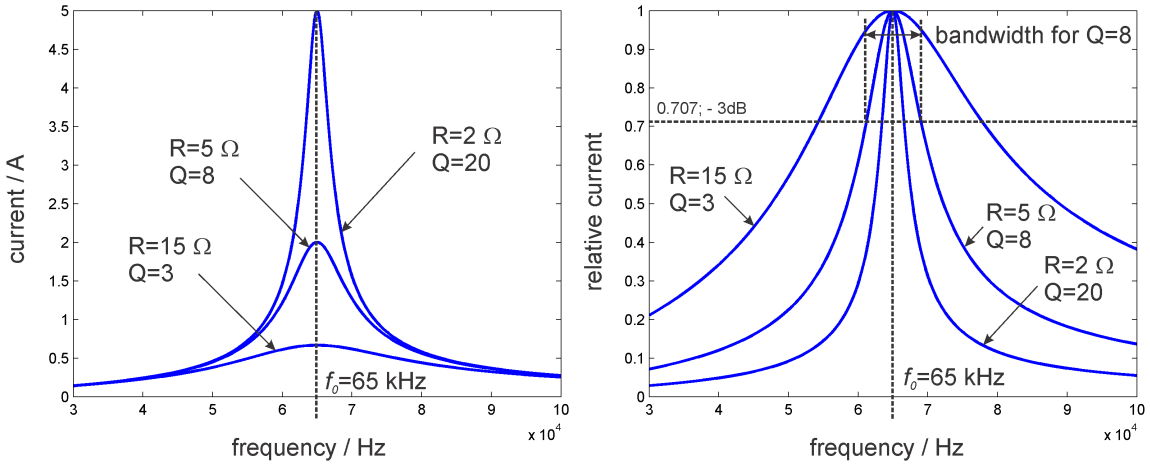

Figure 2.8: Left: Serial RLC circuit current profiles for $U = 10$ V, $L = 100$ μH and $C = 60$ nF and different ohmic resistances, i.e. different quality factors, as a function of frequency. Right: the same current profiles normalized to unity, illustrating the bandwidth for a given Q-value.

2.3.2. Interaction between trap electrodes and charged particles

To describe the interaction between the trap electrodes and particles oscillating between them, it is convenient to consider the trap electrodes as perfectly conducting large capacitor plates separated by a distance D. When a charged particle approaches one of the plates, its charge induces a collection of the opposite mirror charges on the plate. This process can also be described using the model of image charges [49], illustrated in Fig. 2.9, where a single charge q induces a series of images on both electrodes.

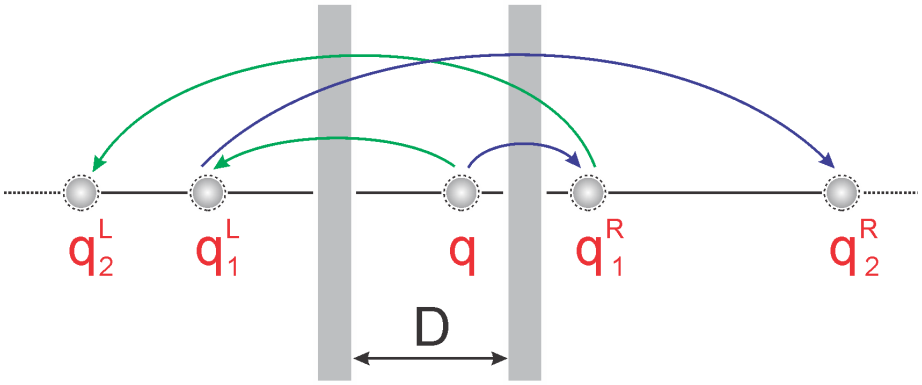

Figure 2.9: The image charge model of the interaction between trap electrodes approximated as capacitor plates and a charged particle. Both plates define a symmetry axis which mirrors all charges on the opposite side. The result is that a single charge induces a series of charges on the left q_i^L and on the right q_i^R.

A detailed analysis can be found in [50], and here it can be readily seen from the model that the image charges will move together with the charged particle. If the two electrodes are connected via a resistor R and an ion oscillates between them, it induces a current $I(t)$ and creates a voltage drop $U(t) = I(t)R$ across the resistor. Hence, the energy of the ion oscillation is dissipated across

the resistor, and the effective force damping the ion motion is

$$F_d = qE = \frac{qU(t)}{D} = \frac{qI(t)R}{D}. \tag{2.46}$$

The power P is given by

$$P = -\dot{z}F_d = RI^2(t), \tag{2.47}$$

where $\dot{z}$ is the axial velocity of the ion. Here, the z-axis was taken as the oscillation axis, but the derivation is also valid for the ion's radial oscillation. Equations (2.46) and (2.47) can be used to derive the current

$$I(t) = \frac{q\dot{z}}{D}. \tag{2.48}$$

If more than one ion oscillates between the electrodes, Eq.(2.48) scales in principle directly with the ion number N. However, due to the strong Coulomb interaction between the particles, any existing coherence in the oscillation is quickly lost, and the statistical contribution to the overall current, given by $\sqrt{N}$, has to be used instead. A geometric factor β also has to be added in order to account for real trap electrodes. If the endcap electrodes were really infinite plates, the factor β would be exactly 1; in this case $\beta \approx 0.8$ [42]. With those two factors Eq.(2.48) becomes

$$I(t) = \beta\sqrt{N}\frac{q\dot{z}}{D}. \tag{2.49}$$

These factors will be disregarded for the moment and reinserted later on.

On the other hand, equation (2.11) defines the axial ion motion as a harmonic oscillation between the trap electrodes. The restoring force of this oscillation is given by the electrostatic potential between the endcaps and the ring electrode

$$F_e = -m\omega_z^2 z. \tag{2.50}$$

Now Eq.(2.46) and (2.50) can be combined to describe the resulting ion motion

$$m\ddot{z} = F_d + F_e = \frac{qU(t)}{D} - m\omega_z^2 z \tag{2.51}$$

which can be used together with Eq.(2.48) to express the potential difference between the endcaps in terms of the induced current between them

$$U(t) = m\frac{D^2}{q^2}\frac{\mathrm{d}I(t)}{\mathrm{d}t} + m\omega_z^2\frac{D^2}{q^2}\int^t I(t')\mathrm{d}t'. \tag{2.52}$$

Using the substitutions

$$\begin{aligned} L' &= m\frac{D^2}{q^2} \\ C' &= \frac{1}{L'\omega_z^2} \end{aligned} \tag{2.53}$$

Eq.(2.52) becomes

$$U(t) = L'\frac{\mathrm{d}I(t)}{\mathrm{d}t} + \frac{1}{C'}\int^t I('t)\mathrm{d}t', \tag{2.54}$$

which is analogous to a voltage across an LC resonant circuit with $R = 0$, as given by Eq.(2.41). However, an ohmic resistance has to be added in all real circuits, meaning that the trap-ion system can be very well modelled with an RLC circuit [51].

2.3.3. Passive tuned-circuit noise detection

The electrical coupling between the trapped ions and the trap electrodes can be used as a powerful non-destructive detection method called passive tuned-circuit noise detection. Equation (2.48) defines the alternating current induced in the trap electrodes by the oscillating ions. The voltage drop caused by this current across an external circuit can be maximized if an RLC resonant circuit is used, as illustrated in Fig. 2.10.

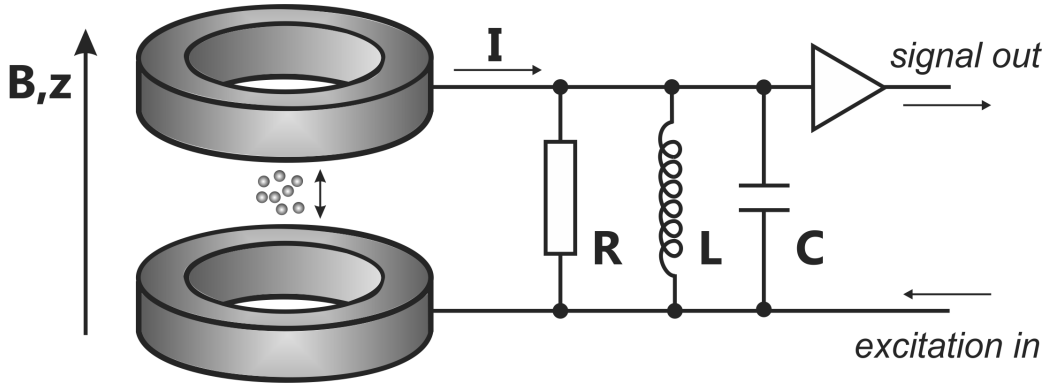

Figure 2.10: A schematic model of an RLC circuit attached to the endcap electrodes of a cylindrical Penning trap. The oscillating ions induce a current in the electrodes and the circuit. The signal in form of the voltage drop across the ohmic resistance is amplified and read out. Ions can also be briefly excited in order to boost the signal. The detection principle is analogous for radial oscillation.

It is therefore necessary to match the ion oscillation frequency given by Eq.(2.29) and the circuit's resonant frequency given by Eq.(2.38)

$$\sqrt{\frac{qV_0}{md^2}C_2} = \frac{1}{\sqrt{LC}}. \tag{2.55}$$

Since d and C_2 are fixed trap parameters, as defined in section 2.1, it is obvious that different q/m ratios will have different oscillation frequencies. They can, however, be "tuned" to a desired frequency by changing the trapping voltage V_0.

As shown in Fig. 2.8, the amplification factor depends directly on the quality factor of the resonant circuit, defined by Eq.(2.44). It reaches its maximum when the coupled frequencies exactly match and will have a continuous drop as a function of the circuit's bandwidth. In terms of ion oscillation frequency this means:

$$Q = \frac{\omega_z}{\Delta\omega_z}. \tag{2.56}$$

The frequency span $\Delta\omega_z$ can be understood as a range where the resonant circuit still has a significant amplification factor. It is of great importance when considering an ion cloud instead of a single trapped ion, since different ions will have slightly different oscillation frequencies due to trap imperfections, space charge, collisions with the residual gas and intra-cloud scattering. This results in a certain frequency distribution around the central frequency ω_z and, depending on the application, a compromise has to be made between large amplification (which requires a large Q-factor) and sufficiently large frequency acceptance (which requires a small Q-factor).

In order to estimate the amplitude of this signal, one has to consider the power dissipation of the induced current I from Eq.(2.49) across the resistor R

$$P = I^2R = N\frac{\beta^2q^2v_z^2}{D^2}R = N\frac{\beta^2q^2}{D^2}\frac{Q}{\omega C}v_z^2 \tag{2.57}$$

where v_z is the axial velocity of the ions and the quality factor Q from Eq.(2.44) was used. If one introduces the axial kinetic energy $E_k = \frac{mv_z^2}{2}$, Eq.(2.57) becomes

$$P = N\left(\frac{\beta q}{D}\right)^2\frac{Q}{\omega C}\frac{2E_k}{m}. \tag{2.58}$$

Taking into account that the energy of a harmonic oscillator can also be written as

$$E = \frac{mv_z^2}{2} = \frac{m}{2}\omega_z^2Z_0^2 \tag{2.59}$$

where Z_0 is the amplitude of ion's axial motion, Eqs.(2.49) and (2.58) can be used to determine the signal amplitude in volts generated by the oscillating ions. It is given by

$$S = \frac{P}{I} = \beta\sqrt{N}\frac{qZ_0}{DC}Q. \tag{2.60}$$

This equation is very important for estimating the sensitivity and signal-to-noise ratio of the circuitry used for this type of ion detection. It can be seen in both Eq.(2.58) and Eq.(2.60) that several factors have to be considered in order to obtain a large signal. These are

- the ion charge q. The advantage of using HCI is obvious since $S \sim q$.
- the kinetic energy of the ions, which can be directly associated with ion temperature using the Boltzman energy $E = k_BT$.
- the total number of ions, important for interpreting experimental results. A higher signal can mean both a higher ion temperature and a larger number of ions.
- the quality factor of the resonant circuit, which should be as high as possible. But there is a trade-off with the bandwidth, which may become too narrow for a desired experiment.
- the capacitance of the circuit, which reduces the signal. This includes the parasitic capacitance of the cables and the electrodes. Therefore electrical connections should be as short as possible, trap electrodes not too massive and the gap between them not too small.
- the effective electrode distance, which means that smaller traps provide a higher sensitivity.

All these requirements cannot be met at the same time, and depending on the application different compromises have to be made. For instance, as already mentioned, a large Q-factor will possibly result in a bandwidth smaller than the ion oscillation frequency bandwidth $\Delta\omega$, giving finally a weaker interaction and a smaller signal. Also, a small trap size produces a higher signal, but also lowers the space charge limit of the trap.

It should be noted that the signal can be further increased by an external excitation of the ion cloud with a short burst of an RF voltage at the resonant frequency. If this is applied to the corresponding trap electrodes, the ions will absorb some power of the excitation and their energy will increase. Additionally, their motion will become more correlated for a short period of time and the statistical factor $\sqrt{N}$ from Eq.(2.49) can be replaced by N.

2.4. Ion cooling

The first-order Doppler shift, discussed in section 1.3.2, is linear in velocity and the dominant spectral line-broadening effect in ion traps. It can be removed only by applying sophisticated techniques, such as two-photon absorption and Dicke narrowing. The former requires intense counter propagating laser beams, while the latter requires that the in-trap oscillation amplitude of the ions is much smaller than the transition wavelength, which is possible only for millimetre wave and microwave radiation[2]. Additionally, the second-order (relativistic) Doppler shift cannot be removed even with these techniques. A solution to both problems is offered by *ion cooling*.

Over the past three decades ion cooling techniques have advanced to sub-K ion motional temperatures, and even the quantum mechanical ground state of ion oscillation was reached [52]. This offers several beneficial effects for experiments with trapped ions. First, the storage time increases with lower temperatures because of smaller electron capture cross sections. Second, reduction in Doppler broadening leads to much higher experimental precision, as already mentioned. Finally, some phenomena, like the formation of Coulomb crystals and Bose-Einstein condensation of atoms, can be observed only at extremely low temperatures.

Three different ion cooling methods are foreseen in SpecTrap - resistive cooling, laser Doppler cooling and sympathetic cooling - and they will be described in the next sections. It should be noted that, unlike in the case of sympathetic cooling, resistive cooling and laser Doppler cooling are cooling methods that in principle address a single ion motional degree of freedom in the trap, while the other ones remain undisturbed.

There is a number of well established ion cooling techniques which are not a part of this work. The main ones are *evaporative cooling*, where collisionally coupled ions in a potential well are cooled down by allowing the most energetic ones to escape the confining well, and variations of laser cooling such as *Sisyphus cooling* (exploiting a polarization gradient of two counter propagating laser beams) and *resolved sideband cooling* (exploiting absorption sidebands of an ion which has an oscillation frequency that is much higher than the transition linewidth).

2.4.1. Resistive cooling

The basis of resistive cooling has been treated in section 2.3.3, where the alternating current I, induced by the oscillating ions, creates a voltage drop across an ohmic resistance R. The dissipated energy is effectively taken out of the ion cloud, which is consequently cooled down.

According to the theory of resonant circuits, the total energy $E(t)$ of the ion-trap resonant circuit decreases exponentially

$$E(t) = E_0 e^{-\frac{t}{\tau}} \tag{2.61}$$

where E_0 is the initial energy and τ the cooling time constant. It can be calculated using Eq.(2.58) for a single ion

$$P = -\left(\frac{\beta q}{D}\right)^2 \frac{Q}{\omega C}\frac{2E_k}{m} = \frac{\mathrm{d}E(t)}{\mathrm{d}t}. \tag{2.62}$$

[2]Actually, for extremely high ion charge states it is possible to enter the Lamb-Dicke regime even in the optical spectrum [53], but it will not be used in SpecTrap.

It can be safely assumed that the trapped ion energy E is almost entirely kinetic. Then, by taking into account

$$\frac{\mathrm{d}E(t)}{\mathrm{d}t} = -\frac{1}{\tau}E \tag{2.63}$$

it follows from Eq.(2.62) that

$$\tau = \left(\frac{D}{\beta q}\right)^2 \frac{m\omega C}{2Q} \approx 4 \cdot \frac{\tilde{m}}{\tilde{q}^2} \text{ [s]} \tag{2.64}$$

where $\tilde{m}$ and $\tilde{q}$ are the mass and charge numbers, respectively, and the values for the approximate calculation of the numerical constant were taken for the SpecTrap Penning trap ($D = 12$ mm, $Q = 300$, $\omega_z = 2\pi \cdot 500$ kHz and $C = 50$ pF). The calculated values for some relevant ions are

$$\tau(^{208}\mathrm{Pb}^{81+}) = 0.13 \text{ s}$$
$$\tau(^{40}\mathrm{Ca}^{14+}) = 0.8 \text{ s}$$
$$\tau(^{24}\mathrm{Mg}^{+}) = 96 \text{ s}$$
$$\tau(^{208}\mathrm{Pb}^{+}) = 832 \text{ s}$$

It is obvious that resistive cooling is more effective for HCI, which also follows from Eq.(2.64), since the cooling time scales inverse quadratically with the charge and only linearly with the mass.

Equation (2.64) is derived for a single trapped ion and it applies only to the centre-of-mass motion. This makes resistive cooling of a large ion cloud far less effective than cooling of a single ion. It is most easily seen in the so-called "breathing" model of an ion cloud where the centre of charge is stationary and the overall induced current is zero. This is however an ideal model, and in reality energy will be transferred from ion to ion through intra-cloud collisions, leading to non-zero centre-of-charge motion and energy dissipation in the resonance circuits. Consequently, an ion cloud is cooled but with a considerably longer time constant [50].

At high temperatures of a cloud of ions will have a large motional frequency distribution. To that end, the quality factor Q has to be carefully tuned: a high value means fast cooling inside a very small frequency range, and vice versa, a small value covers a large frequency span, but results in a weak interaction with the ion cloud.

To conclude, the main advantages of resistive cooling are the applicability to all ion species, as long as the oscillation frequency can be brought into resonance, and the fact that no particles are destroyed in the process. The lower limit of this cooling method is reached when a thermal equilibrium between the resonant circuit and the trapped particles is established. If the circuit is cooled with liquid helium this limit is 4.2 K. However, the electronic noise temperature of the circuits coupled to the ion motion can be significantly higher and result in a correspondingly higher ion temperature [54], independent for all three ion eigenmotions. Therefore, other cooling methods have to be applied if lower temperatures are required.

2.4.2. Laser Doppler cooling

Using the relativistic expression for energy $E = \hbar\omega = \sqrt{m^2c^4 + p^2c^2}$ it is possible to assign momentum $p = E/c$ even to a particle without mass, such as a photon. Hence, it follows from the conservation of momentum that an object absorbing radiation must change its momentum.

Therefore the net force F_{rad} exerted on an atom is proportional to the rate at which photons are absorbed. The momentum transfer leads to a force

$$F_{\text{rad}} = -\frac{\sigma_{\text{abs}} I}{c} \tag{2.65}$$

where I is the light intensity and σ_{abs} the frequency-dependent absorption cross-section. The minus sign indicates a force opposite to the Pointing vector.

A net acceleration effect on a particle can be achieved if the absorbed photons are taken from a unidirectional monochromatic, well-collimated laser beam. Each absorbed photon gives the ion (or atom) a kick in the direction of its motion, while the spontaneously emitted photons are evenly distributed in all directions. On average, this results in a scattering force which slows the particle down, proportional to the rate of photon absorption. This force is given by [26]

$$F_{\text{scatt}} = \hbar k \cdot \frac{\Gamma}{2} \cdot \frac{I/I_{\text{sat}}}{1 + I/I_{\text{sat}} + 4\delta^2/\Gamma^2} \tag{2.66}$$

where $\Gamma = \frac{1}{\tau_0}$ is the excited level's decay rate, I_{sat} the saturation intensity (as given by Eq.(1.25)) and $\delta = \omega - \omega_0 + kv$ the detuning of the laser frequency ω from resonance ω_0, taking into account the Doppler shift kv. The scattering force converges for $I \to \infty$ to the limit

$$F_{\text{max}} = \hbar k \frac{\Gamma}{2}. \tag{2.67}$$

The factor $\frac{\Gamma}{2}$ is caused by the fact that at large intensities the upper and the lower level are equally populated. Now, for an ion of mass m the maximum acceleration produced by this radiation can be written as

$$a_{\text{max}} = \frac{\hbar k}{m} \frac{\Gamma}{2}. \tag{2.68}$$

Typically, the deceleration rate is kept at about half the maximum value in order to obtain a strong force without significant power broadening of the transition.

Table 2.1: A list of the most common ions suitable for laser cooling. The atomic mass number was given for the most abundant isotope.

Ion	Atomic mass number	Resonance wavelength [nm]	Excited level lifetime [ns]
Be^+	9	313	9
Mg^+	24	280	4
Ca^+	40	397	7
Yb^+	174	369	42
Hg^+	202	194	2

The ion's kinetic energy after cooling can be calculated by taking into account the scattering force, the time average of the spontaneous emission force and their fluctuations [26]. The result is actually the ion temperature T, since it can be associated to the energy with the Boltzmann constant k_B. It is given by [26]

$$k_B T = \frac{\hbar\Gamma}{4} \cdot \frac{1 + (2\delta/\Gamma)^2}{-2\delta/\Gamma}. \tag{2.69}$$

This function exhibits a minimum for $\delta = -\frac{\Gamma}{2}$. That defines the *Doppler cooling limit*

$$k_B T = \frac{\hbar\Gamma}{2}, \tag{2.70}$$

which gives the lowest theoretical temperature achievable with this ion cooling method. This temperature is 1 mK for laser Doppler cooling of Mg^+.

2.4.3. Sympathetic cooling

Although laser cooling is a very powerful ion cooling method which reaches sub-K temperatures, it depends on a favourable level structure and has therefore been demonstrated only for a few ion species. Some of them are listed in Tab. 2.1. An arbitrary ion species can be cooled via *sympathetic cooling*. In that scheme two different charged particle species are loaded simultaneously into the trap. While one of them is cooled directly, e.g. by laser cooling, the temperature of the other one is reduced through Coulomb collisions in which the two ion species exchange energy and finally equalize in temperature.

The time until the collisionally coupled particles with mass and charge (m, q) and (m', q') reach the thermal equilibrium can be expressed using the characteristic time constant [55]

$$\tau_{\mathrm{eq}} = \frac{\sqrt{18\pi^3}\epsilon_0^2 m m' k_B^{3/2}}{n' q^2 q'^2 \ln\Lambda} \sqrt{\left(\frac{T}{m} + \frac{T'}{m'}\right)^3} \tag{2.71}$$

where n and n' are the cooled and pre-cooled particle densities, respectively, T and T' their corresponding temperatures and $\ln\Lambda$ the so-called Coulomb logarithm given by

$$\ln\Lambda = \ln\left[6\pi\sqrt{\frac{2}{n}\left(\frac{\epsilon_0 k_B T}{q^2}\right)^3}\right]. \tag{2.72}$$

As a figure of merit, a time constant of $\tau_{\mathrm{eq}} \approx 200$ ms can be calculated for a laser-cooled particle density of $n = 3 \cdot 10^{14}$ ions/m^3 mixed with highly charged ions in a Penning trap [55]. It should be noted, however, that this time is difficult to measure experimentally and can be significantly different for other ion temperatures, charge states or masses.

If two ion species with different masses are trapped, their magnetron drift frequencies, defined by Eq.(2.13), will be slightly different. Because of different angular velocities, the two species will have a collisional interaction and a momentum exchange in the φ direction. Due to the angular momentum conservation, this causes a radial separation of the two ion species, where the larger mass will have a larger orbit around the trap z axis and vice versa. The process continues until the frequencies equalize and the cloud starts rotating as a rigid body [56], which is a characteristic of a non-neutral plasma in thermal equilibrium. Although the heavier ions as a result form a ring around the lighter ones, limiting the thermal coupling, sympathetic cooling is still possible due to the strong electrical coupling and was experimentally demonstrated [55].

Chapter 3

The SpecTrap Penning trap system

This chapter describes the heart of the SpecTrap experimental setup - the cylindrical open-endcap Penning trap. Penning traps of that form are a tool of choice for precision experiments with low and highly charged ions [38, 40]. SpecTrap aims at measuring relatively slow transitions in highly charged ions, and the trap design had to focus on storing a large ion cloud and on maximizing the amount of collectable fluorescence photons. Section 3.1 gives a complete description of the mechanical design of the trap electrodes and optical detection system, as well as simulations and calculations of the trap potential. The potential and the signals generated in the trap are processed by the electronic components directly or indirectly connected to the trap electrodes, and they are described in section 3.2. A typical ion capture and ejection cycle is described in section 3.3. It discusses also the possibility of capturing multiple ion bunches and the specific destructive detection techniques for counting the ions ejected from the trap. Finally, section 3.4 gives an overview of the full assembled setup and its limits.

3.1. Trap design

The SpecTrap ion trap is a 5-pole, cylindrical, open-endcap Penning trap, with inner radius of $r_0 = 10.6$ mm, designed for in-flight capture of a large ion bunch, laser spectroscopy and detection of fluorescence photons. It follows the general design of such type of traps, already described in section 2.1.3, with an addition of two capture electrodes, necessary for dynamic ion capture (see section 3.3.1). A technical drawing of the trap is shown in Fig. 3.1. Starting from the centre, it comprises a ring electrode ($z_r = 6.8$ mm), two correction electrodes ($z_c = 1.5$ mm), two endcaps ($z_e = 25$ mm) and two capture electrodes ($z_i = 22$ mm). The capture electrodes are separated by MACOR rings on both sides, whereas the inner electrodes are insulated by 1 mm sapphire balls. The reason for using different insulation materials was to improve the potential in the trap centre, by removing possible charged surfaces (such as insulator material). In terms of breakdown voltage, a conservative estimation is that under the expected ultra-high vacuum conditions, the separation of 1.5 mm and 0.7 mm is sufficient for a potential difference of 2 kV and 1 kV, respectively. All electrodes are made of oxygen free high conductivity (OHFC) copper, because of its good electrical and thermal conductivity and low vacuum outgasing rate. Directly after production, the electrodes were gold plated, to ensure a good surface finish and to prevent

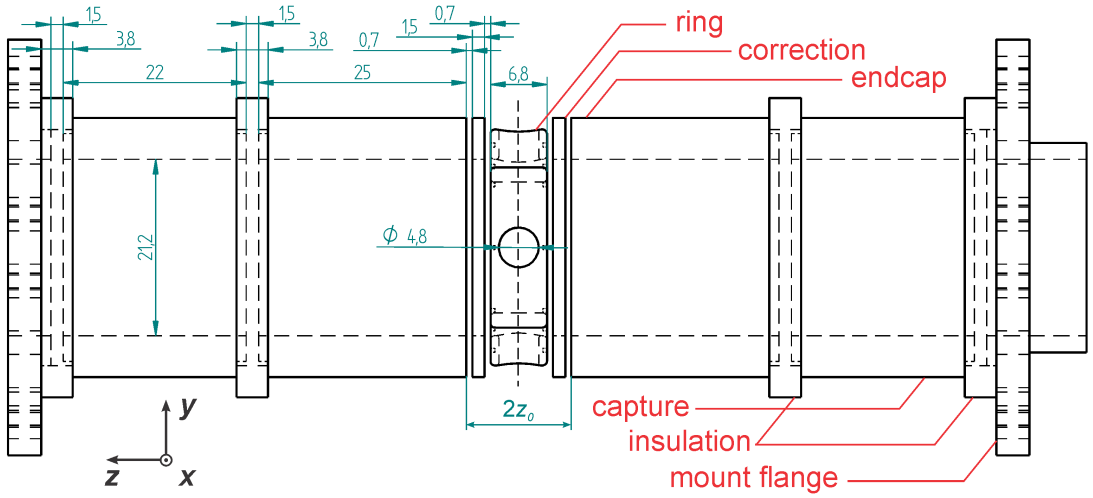

Figure 3.1: Cross section of the SpecTrap Penning trap with the relevant dimensions. The electrode stack is symmetric with respect to the plane splitting the ring electrode vertically in the centre as indicated, with the exception of the two outer flanges for mounting reasons. The insulation of the capture electrodes is realized on both sides with MACOR rings, whereas the inner electrodes are separated by 1 mm sapphire balls (not shown in the drawing). All units are mm ±0.01.

the formation of oxide layers. Silver coating was used to suppress diffusion of gold into the copper electrode. Usually nickel is used for this purpose, but since it is strongly ferromagnetic, it is not suitable for a Penning trap. To avoid damaging the thin gold layer (0.5 μm), all mechanical treatment of the trap electrodes had to be finished prior to the gold plating.

The ring electrode is split into four segments to allow for ion cyclotron frequency detection, ion excitation and implementation of the rotating wall compression technique. The latter was tested at Imperial College, and a detailed analysis of the achieved compression and related effects can be found in [57]. A 4.8 mm hole for detection of ion fluorescence was made in the centre of each of the four segments. This diameter was chosen as the maximum size that does not compromise the stability of the electrode segments. A previous version based on a copper mesh with 70% transmission instead of holes was abandoned since electron emission was observed. In contrast, the holes offer 100% transmission for photons for the price of a negligible loss in the harmonicity of the potential. The sides facing the correction electrodes are equipped with three small ($\varnothing = 0.5$ mm) blind holes to hold the saphire balls for electrode separation.

A three-dimensional overview of the trap assembly is shown in Fig. 3.2. The complete electrode stack is mounted on four parallel rods, forming the corners of a square that is defined by the cuts of the ring electrode. The rods establish mechanical contact with the trap only on the mounting flanges from Fig. 3.1, which are grounded and compress the electrode stack longitudinally. Assembled further out, but parallel with the main rods are four support rods, which hold the platform for trap's optical components (see section 3.1.2).

The main aluminium flange offers a stable support for the trap assembly (24 M5 screws at $\varnothing = 146$ mm). It is mounted on the bottom of the SpecTrap magnet LHe reservoir (see section

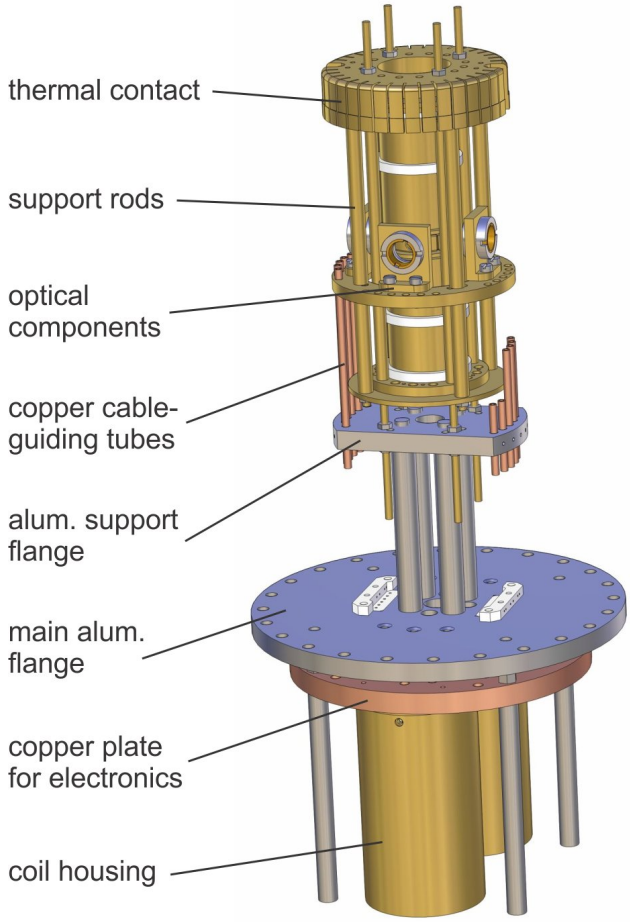

Figure 3.2: Drawing of the complete mechanical trap assembly, without cables and electronic components. It is mounted vertically as depicted; ions are introduced from the top, and the laser beam is aligned along the vertical axis from the bottom. The smallest aperture is the main aluminium flange, with a $\varnothing = 12$ mm central hole. The part above extends into the superconducting magnet central bore (see section 4.1), and the optical components are aligned with the radial windows. Cables are guided from the individual electrodes around or inside the copper tubes, towards PEEK connectors (white in the drawing) inside the main aluminium flange, which make the contact with the electronic components on the copper flange. Not shown are the filter boxes, which are plugged to the bottom of the copper flange and lead the electrical signals in and out of the trap assembly.

4.1) and thus also provides strong thermal coupling between the cryostat and the trap assembly. The distance of 159.25 mm between this flange and the homogeneous magnetic field region, where the trap centre has to be located, is bridged in two stages. Coarse spacing is done with four aluminium pillars, holding the $\varnothing = 80$ mm aluminium support flange, 72 mm above the main flange. Fine adjustment of the trap height is possible along the rods forming the support structures of the trap. They protrude the support aluminium flange at three possible mounting positions 11° from each other, providing also radial adjustment if necessary.

A copper plate that holds the trap's cryogenic electrical components and high-Q coil housings is mounted directly below the main aluminium flange. The electronics will be described in detail in section 3.2. Their mounting position directly below the LHe reservoir guarantees strong thermal coupling, keeping the operating temperature low. A grounded electrode with flexible flaps is added on top of the stack, and it provides additional thermal coupling to the cryostat and reduces the temperature gradient along the trap.

Electrical connection of the trap electrodes and the electronic elements on the copper plate is provided by PTFE[1] insulated copper cables. The capture electrodes were connected with Kapton insulated cables because of the high voltage requirements. Figure 3.2 shows also copper tubes which provide electrical shielding and guide the cables towards the trap electrodes.

[1]Polytetrafluoroethylene, most well known under the brand name Teflon by DuPont Co.

3.1.1. Simulations and trap imperfections

Using a cylindrical open-endcap Penning trap offers significant advantages for the price of a slightly less harmonic potential, as discussed in section 2.1.3. The expansion coefficients C_k, $C_k^{(0)}$ and D_k are used in Eq.(2.20) to describe the electric potential of such a trap. Since they can be analytically calculated, the trap electrodes can be designed to achieve an orthogonal trap and a quasi-harmonic potential. The result of this optimization for the SpecTrap ion trap is presented in Tab. 3.1.

Table 3.1: Dimensions and expansion coefficients of the SpecTrap cylindrical open-endcap Penning trap.

dimension	exp. coeff.
endcap distance $z_0 = 6.30$ mm	$C_2^{(0)} = 0.563$
inner radius $r_0/z_0 = 1.68$	$D_2 = 0.027$
ring size $z_r/z_0 = 1.08$	$C_4^{(0)} = -0.127$
correction size $z_c/z_0 = 0.24$	$D_4 = -0.078$
endcap size $z_e/z_0 = 3.97$	$C_6^{(0)} = 0.003$
capture size $z_{cp}/z_0 = 3.49$	$D_6 = 0.032$

The tuning ratio V_c/V_0 needed to tune C_4 to zero can now be calculated using

$$\frac{V_c}{V_0} = -\frac{C_4^{(0)}}{D_4} = -1.63. \tag{3.1}$$

Moreover, the D_2 coefficient is roughly 20 times smaller than $C_2^{(0)}$, making the coefficient C_2 almost independent of the V_c/V_0 ratio and thus the trap orthogonal. Therefore, it can be calculated that

$$C_2 \approx 0.52. \tag{3.2}$$

Finally, the z_c/z_0 ratio was chosen such that the C_6 coefficient almost vanishes. If the V_c/V_0 ratio is kept unchanged, it can be calculated that

$$C_6 \approx -0.05. \tag{3.3}$$

The analysis shows that the SpecTrap ion trap can be orthogonalized to a large degree and the C_4 coefficient can be tuned out, leading to a negligible frequency shift according to Eq.(2.30). However, the required voltage ratio between the correction and endcap electrodes is rather high and limits the achievable trap potential depth in practice. The precision voltage supply used for the trap electrodes in SpecTrap can provide a maximum voltage of $V_{\max} = 500$ V (unipolar). By taking into account that the endcap and correction voltages are defined with respect to the ring electrode, the condition given by Eq.(3.1) becomes

$$\frac{V_c - V_r}{V_e - V_r} = \frac{V_{c:r}}{V_{e:r}} = -1.63 \tag{3.4}$$

where $V_{e/c/r}$ are voltages with respect to ground and $V_{e:r/c:r}$ with respect to the ring. If the endcap and correction voltages take the maximum value $V_e = -V_c = V_{\max} = 500$ V, the necessary voltage

ratio is achieved when $V_r = 120$ V. The maximum trap depth, in terms of potential difference between the ring and the endcap electrodes, is then

$$V_{e:r} = V_{\max} - V_r = 380 \text{ V}; \qquad V_{c:r} = -V_{\max} - V_r = -620 \text{ V}; \qquad \text{with } V_r = 120 \text{ V}.$$

Although this is not a "hard" limit defined by internal parameters of the trap, it should not be exceeded because these values also lead to 1 kV potential difference between the correction and the endcap electrodes, which is close to the estimated breakdown voltage.

The calculated potential along the z-axis of the SpecTrap ion trap for a grounded ring electrode and a potential of 100 V at the endcaps is shown in Fig. 3.3. The red line depicts the potential for a grounded correction electrode. Although the potential of the endcaps was set to 100 V, this value is not reached along the central axis and neither is the potential 0 V in the trap centre. The black line represents the potential after introducing $V_c = -1.63 \cdot V_e = -163$ V, which extends the central trap potential closer to zero. An ideal harmonic potential with the same offset at the trap centre is also plotted in blue and shows good agreement with the real potential within ±3 mm from the centre.

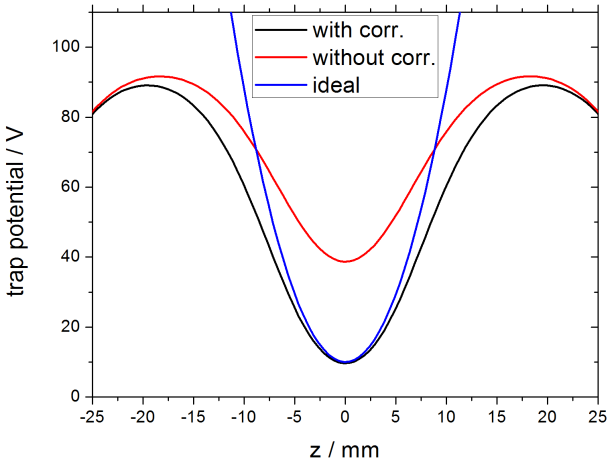

Figure 3.3: Electrical potential along the z axis of the SpecTrap Penning trap for an endcap voltage of $V_e = 100$ V. The red line shows the potential with grounded correction electrodes and the black line with $V_c = -1.63 \cdot V_e$. The blue line shows the ideal form of a harmonic potential for the given trap parameters.

Finally, it should be emphasized that the SpecTrap ion trap was designed for maximizing the observable fluorescence of the stored ions and not for experiments based on high-precision ion oscillation frequency measurements. The oscillation frequencies of the ions in a cloud will have a comparably broad distribution because of the non-vanishing C_k coefficients and the non-ideal trap geometry, making measurements like a g-factor determination [39, 44] not possible. However, it was shown that the trap potential can be made harmonic even with its open-endcap cylindrical geometry, which decouples to a large degree the eigenmotions defined by Eqs.(2.11)-(2.13), and enables storage of a large number of externally produced ions with well defined frequencies and energies. This makes SpecTrap an ideal tool combining ion trapping and cooling, laser spectroscopy and fluorescence detection.

3.1.2. Optical components for fluorescence detection

A special property of the SpecTrap setup is the split-coil configuration of the superconducting magnet and the radial view ports which enable direct optical access to the trap centre (see

section 4.1). A laser beam introduced along the z-axis of the trap can interact with the ions, and their fluorescence can be observed along a radial axis through the holes in the ring electrode, with a detector mounted outside the vacuum system. In order to maximize the fluorescence collection efficiency, optical elements are mounted directly on the trap, close to the laser-ion interaction region. Due to the required ultra-high vacuum conditions, spatial restrictions and a strong magnetic field, it is not possible to use commercial mirror mounts for the alignment of these elements. Instead, a dedicated system was constructed, and it is shown in Fig. 3.4.

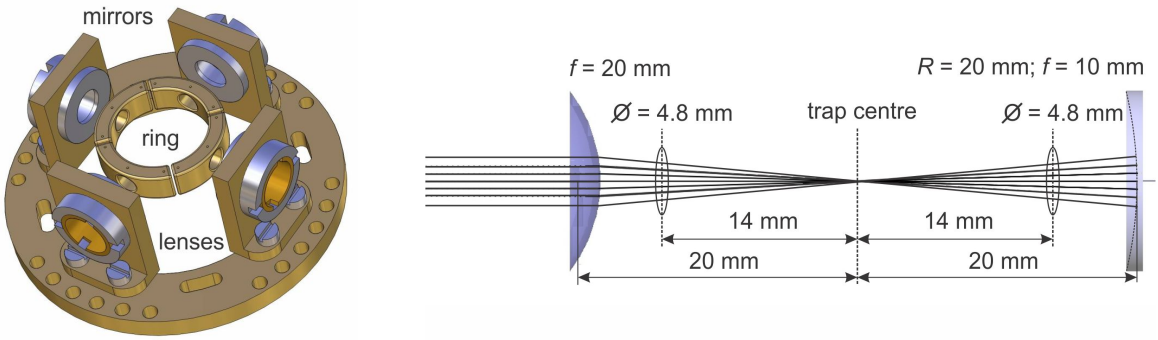

Figure 3.4: Left: ring electrode and the optical elements around it. Right: FRED ray tracing of the spherical lens - mirror system for collecting the fluorescence from the trap centre.

The central holes in the ring electrodes ($\varnothing = 4.8$ mm) are located 14 mm away from the main trap axis. They define a theoretical solid angle of $\Omega = 0.09$ sr, which is a fraction of $7 \cdot 10^{-3}$ out of the total solid angle of 4π. A collection system consisting of a spherical mirror and a plano-convex lens, as depicted in Fig. 3.4, was designed to collimate the light emitted from the centre towards the optical detection system. In that way one part of the light is directly collected by the lens, while another part is reflected back into the trap centre by the mirror and then also collected, thus increasing the overall fluorescence signal. With four holes in the ring electrode it is possible to establish two perpendicular detection axes, which can be simultaneously used for fluorescence detection.

Since the complete optical system is attached directly to the trap and not accessible from outside, it is of critical importance to accurately align the system before installation. To avoid possible post-installation misalignments, both mirror and lens mounts were custom manufactured with no horizontal and vertical rotational degrees of freedom, and good alignment has to be ensured by precise design and mechanical production. The only degrees of freedom while mounting are an adjustment of the distance from the trap centre and a vertical translation. This was optimized using a He:Ne laser beam directed along the main optical axis of the lens-trap-mirror system and observation of the back-reflected image. In case of a good overlap, the size of the reflected image indicates the focusing proportion and its position the alignment of the lens and the mirror. Ideally, the reflected beam should completely overlap with the incident beam. After careful adjustments, the reflected image in SpecTrap had the same size, but also an 8 mm offset 0.5 m away from the trap centre (where the detector is located), which could not be further

improved. Using FRED software[2] it was verified that this is caused by a small residual tilt of the optical elements, which resulted in a vertical offset of the focus by about 0.6 mm. Based on the experience of a similar experiment [55], the expected size of the trapped ion cloud is of the same order of magnitude. Hence, misalignments lead only to a blurred image of the ion cloud, instead of a sharp one, which has little relevance for photon counting, especially since the 8 mm offset on the far side is also well within the aperture of the detection system ($\varnothing = 38$ mm). Therefore it cannot compromise the collecting of fluorescence by a detector mounted at the given distance from the trap centre.

3.2. Electronic components for signal processing

The full ion trapping and non-destructive detection process in SpecTrap is automatized and regulated with the corresponding electronic components. Depending on the requirements, they were designed to operate either in the cryogenic environment of the main vacuum chamber, or outside the system, table-top or mounted in a rack and fully accessible during operation. An overview of the two main groups and the circuitry connecting them to the SpecTrap ion trap is shown in Fig. 3.5.

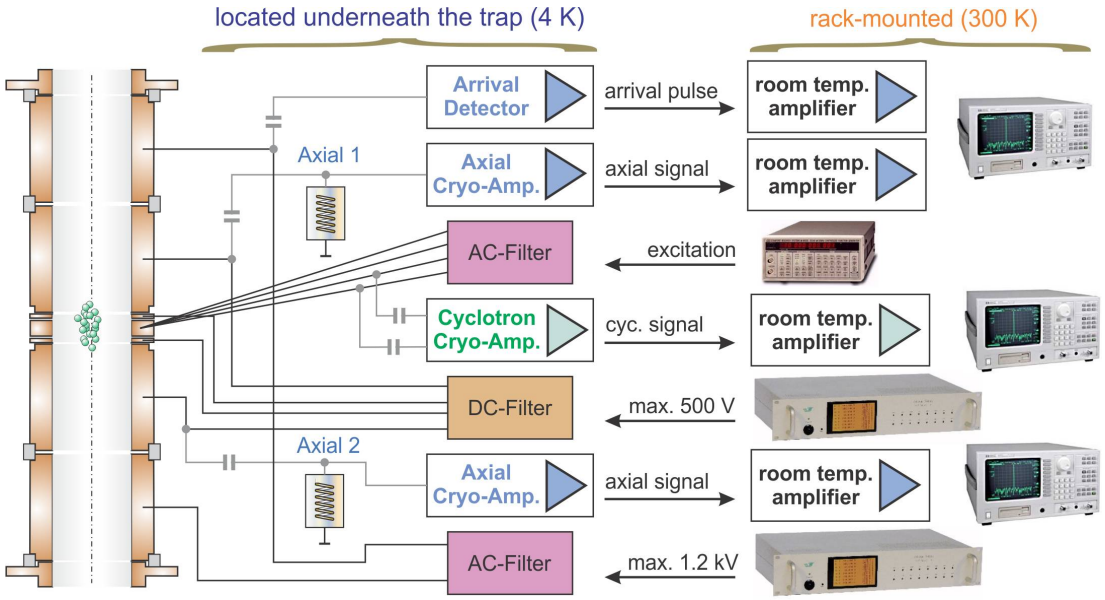

Figure 3.5: Overview of the electronic components of the SpecTrap ion trap system.

For reducing temperature related noise (mainly Johnson noise - see appendix B), it was necessary to keep some components at cryogenic temperatures. They were designed to fit directly under the trap and the liquid helium reservoir and include:

- filters for all signal lines going *towards* the trap electrodes. Although all are different versions of low-pass filters, some were equipped with an override option for transmitting

[2]Fred Optical Engineering Software is a commercial 3D ray tracing software, used to simulate illumination through optical systems.

high-frequency signals with amplitudes above a defined threshold. They are accordingly indicated as DC and AC filters in Fig. 3.5.

- pre-amplifiers for axial and cyclotron frequency signals going *from* the trap electrodes. The former are connected via resonant circuits (Axial 1 and 2 in Fig. 3.5) to the endcaps, while the latter are inductively coupled to the segments of the ring electrode.

- a so-called "arrival detector", or a special pre-amplifier connected to the capture electrode and dedicated to detection of short (Schottky) pulses of the incoming ions.

Since in several cases the same trap electrode has to be used for both ion trapping and detection, electronic signals going in and out of the corresponding electrodes needed to be capacitively decoupled, as can be seen in Fig. 3.5 indicated with dimmer lines. Not shown in the diagram, but equally important for operation of the system, are the power supply lines for the active components of the circuitry.

3.2.1. Filters and signal shaping

Using Eq.(2.60) it can be directly calculated that one singly charged ion creates a voltage signal of the order of a few nV in the trap electrodes, assuming an energy of a few eV, a parasitic trap capacitance of 50 nF and $Q = 1$. On the other hand, Johnson noise of a 10 kΩ resistor at room temperature and 10 kHz bandwidth has a value of the order of μV. Even though the trap and the attached amplifiers are kept at cryogenic temperature, noise picked up from the outer components can be transmitted to the trap electrodes and significantly disturb ion motion and detection. Therefore it is necessary to install filters on all lines connecting the cryogenic parts with the room-temperature electronics. These filters also have to be kept at low temperature. A brief overview of the main filter types can be found in appendix B.2, while the circuit diagrams of those used in SpecTrap are shown in Fig. 3.6, and some important parameters are summarized in Tab. 3.2.

The first filter type is located on the voltage supply lines for the endcaps and the correction electrodes. It is a second-order low-pass filter, whose cut-off frequency ν_c can be calculated according to

$$\nu_c = \frac{1}{2\pi\sqrt{R_1 R_2 C_1 C_2}} \tag{3.5}$$

where $R_1 = 240$ kΩ, $R_2 = 120$ kΩ and $C_{1/2}$ are the capacitors in front of them (not to be mistaken for the trap coefficients). The filter is bypassed with two antiparallel BAS70 Schottky diodes, which transmit signals with an amplitude bigger than their forward voltage drop (approximately 400 mV at 1 mA of current). Finally, the ballast resistor $R = 9.4$ MΩ limits the peak current passing through the circuit and determines the rise time of the potential. Since the filter assembly is located directly under the trap and is not easily accessible, its proper installation can be tested any time by measuring the resistance of $R = 20$ MΩ from the outside, e.g. the vacuum feedthrough.

The second filter type is located on the voltage supply lines going towards the ring electrode segments and shares the same operation principle as the first type, with a different value of ν_c. No

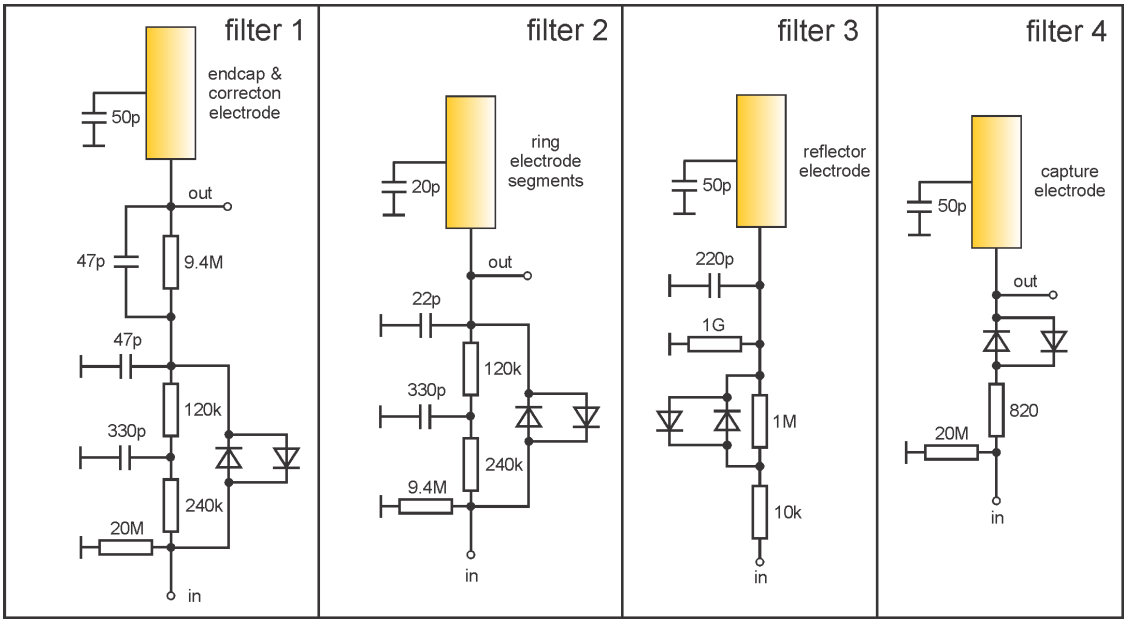

Figure 3.6: Four filter types used in SpecTrap cryogenic electronics. They are connected to endcap/correction, ring, reflector and capture electrode, respectively. The capacitors attached to the electrodes (in yellow) are symbolic parasitic capacitances of the corresponding electrodes. Signal "out" denotes the place from where the resonance is picked up.

ballast resistor was included in the circuitry in order to ensure small rise time of the electrode's potential, necessary for transmitting high-frequency signals for detection and excitation of the ions' radial motion. The maximum current and the voltage rise time, as listed in Tab. 3.2, are instead defined by the input impedance of 50 Ω and the diode's residual resistance of about 10 Ω. Proper connection can also be tested by measuring the resistance $R = 9.4$ MΩ.

The third filter is connected to the reflector electrode supply line without a signal pick-up option. It is a first-order low-pass filter with a bypass option analogous to the first two filter types. The fourth circuitry from Fig. 3.6 is connected to the capture electrode, and it is not a filter in the strict definition of the term. However, the two anti-parallel diodes remain non-conductive for small amplitude signals, which effectively eliminates all static noise from the supply line. It also incorporates a ballast and a test resistor.

For full control of the ion trapping and storing process it is important to know the time constants of all input signals going through the attached filters. The *rise time* of a low-pass RC network can be defined as the time period in which the voltage signal behind the filter changes its value from 10% to 90 % of its final amplitude, or vice versa for a signal *drop time*. If the system has a Gaussian response (as typically the case), it can be evaluated by using the output response of the network

$$V(t) = V_0 \left(1 - e^{-t/\tau}\right) \tag{3.6}$$

where $\tau = RC$ is the time constant of the system. For $V_1 = 0.1 \cdot V_0$ and $V_2 = 0.9 \cdot V_0$ it can be calculated that the rise time t_r is given by

$$t_r \approx 2.2 \cdot \tau. \tag{3.7}$$

Since all described filters have a bypass option, the rise time is calculated by using the ballast resistance and the parasitic capacitance. These values, as well as other characteristics of the filters used at SpecTrap, are listed in Tab. 3.2.

Table 3.2: Overview of the main characteristics of the supply line filters in SpecTrap. The parasitic capacitances include the values from Fig. 3.6, the parasitic capacitances of the attached diodes (10 pF) as well as the contribution of non-coaxial connection cables (≈ 30 pF). The values were used to calculate the cut-off frequency coming from the diodes, as well as the rise time according to Eq.(3.7).

	filter 1	filter 2	filter 3	filter 4
electrode	endcap/corr.	ring segments	reflector	capture
filter cut-off frequency [kHz]	7.5	11	0.7	0
parasitic capacitance [pF]	70/30	40	100	100
diode cut-off frequency [MHz]	≪0.01	56	0.02	2
rise time [μs]	200/85	≪0.1	2	0.2

3.2.2. Cryogenic amplifiers and resonant circuits

In order to amplify the small voltage signals generated between the trap electrodes by the oscillating ions before they are lost in the thermal noise present in the room temperature electronics, it is necessary to use pre-amplifiers in the cryogenic region of the system. They were developed in collaboration with Stahl Electronics[3] on the basis of novel ultra-low noise gallium arsenide (GaAs) metal semiconductor field effect transistors (MESFETs). A simplified circuit diagram is shown in Fig. 3.7.

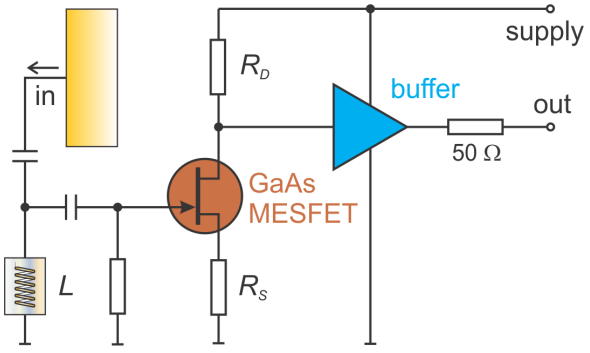

Figure 3.7: A simplified diagram of the gallium arsenide MESFET-based cryogenic amplifier, designed by Stahl Electronics and used in SpecTrap. A trap electrode is connected to the amplifier and an inductive coil L, which enhances the signal by a factor of Q. After amplification, the impedance of the signal is set to 50 Ω by a buffer stage.

The voltage gain A_v of such an amplifier is given by [47]

$$A_v = -\frac{g_m R_D}{1 + g_m R_S} \tag{3.8}$$

where R_D and R_S are the drain and source resistances, respectively, and g_m is the transconductance, which is an intrinsic characteristic of a transistor. For this type of MESFETs typical values of g_m range from $1 \cdot 10^{-3}$ to $3 \cdot 10^{-3}$ Ω^{-1}, which results in amplification factor of around $A_v \approx 3$

[3] Stahl Electronics is a private company specialized in general and cryogenic electronics and engineering services - www.stahl-electronics.com

for drain and source resistances of around 1500 Ω. Such an amplified signal goes then through a buffer stage in order to match its impedance with the coaxial cable and post-amplifiers located at room temperature.

As discussed in section 2.3.3, axial or cyclotron resonance signals can be significantly enhanced using a resonant circuit. In a so-called free running system, this is done by adding a coil between an electrode of interest and the pre-amplifier, as indicated in Fig. 3.7. Such an arrangement increases the non-amplified signal by the quality factor Q of the circuit, which directly depends on the residual resistance, as can be seen from Eq.(2.44). The coil in SpecTrap was constructed out of a PTFE insulated constantan cable, in contrast to commonly used superconductive material, in order to keep the quality factor low for the sake of a larger bandwidth of the circuit. For adding more flexibility to the system, two such resonant circuits were built, attached to each of the endcap electrodes and set for different resonant frequencies. The number of coil windings, i.e. the coil inductance was designed for approximately 500 kHz and 1 MHz resonant frequencies, resulting in $L_1 = 1.8$ mH and $L_2 = 0.5$ mH with about 50 pF parasitic capacitance.

The same basic design from Fig. 3.7 was used also for amplification of the ion cyclotron oscillation signal, but without a resonant circuit because of space restrictions. Instead, a MESFET with a higher transconductance g_m was used in order to achieve a larger amplification factor.

Finally, a novel detector type was designed for the purpose of shot-noise detection of ions flying into the trap through the capture electrode, based on the Schottky-pick-up technique. It was accordingly named *arrival detector*, since its purpose is to create a trigger upon arrival of an ion bunch that can be used to close the trap. With the expected noise level, its design should allow detection of around 2000 elementary charges or more, grouped in a bunch shorter than the capture electrode length [58]. In the case of highly charged ions, this number corresponds to some 150 $^{40}Ca^{14+}$ or only 25 $^{208}Pb^{81+}$, which is easily achievable with the HITRAP facility.

3.2.3. Room temperature electronics

Although the cryogenic environment brings significant reduction in thermal noise, it also leads to carrier freeze-out of most semiconductor materials, which is a serious problem when designing active electrical components that should remain fully operational under such conditions. Additionally, available space in cryostats is usually very limited and sensitive to thermal load. This is also the case at SpecTrap and therefore most of the electrical components associated with the SpecTrap ion trap were located outside the vacuum and cryogenic environment of the superconducting magnet. They are used to

1. generate low and high-voltage signals for the trap electrodes,
2. supply the active parts of the cryogenic circuitry,
3. generate the high-frequency excitation signals to be applied to the trap electrodes,
4. post-amplify the signals coming from the trap and the cryogenic electronics and
5. perform frequency analysis of the signals.

Figure 3.8: Overview of the main room temperature electronics and data acquisition devices used in SpecTrap. From top to bottom:
Agilent 33250A - frequency generator
HP 3589A - spectrum/network analyser
HP 3336A - synthesized function generator
Cryo Bias - power supply and room temperature amplification for cryo-electronics
HV-500-8 - precision voltage supply
QUAD 1-10 - rotating wall drive
Not shown are DS345 function generators, HV power supplies and switches. The timing for switching the trap electrodes is relized with two DG535 digital delay generators, which are also not visible on the photo.

A photo of some of these elements, as they are mounted in the experimental setup, is shown in Fig. 3.8

Potentials for the trap electrodes are supplied by a LabVIEW controlled HV-500-8 precision voltage source from Stahl Electronics. It offers eight unipolar channels which provide up to ±500 V, with a typical absolute accuracy of 0.01% and short-term fluctuations of the order of 5 mV. All seven trap electrodes (counting the four ring segments as one) can be independently supplied, with one spare channel.

The signal for excitation of the ion motion can be supplied by three different frequency generators: Stanford Research DS345, Hewlett Packard 3336A and Agilent 33250A. Each has its own different set of characteristics and operation modes, and they are used based on the specific frequency, noise and amplitude requirements. The cyclotron excitation signal is prepared by a Stahl Electronics QUAD 1-10 Rotating Wall Drive, which splits a sinusoidal input signal into four parts with a 90° phase offset between the consecutive channels, which are then amplified and applied to the ring segments.

Finally, analysis of the signals from the trap is performed with a Hewlett Packard 3589A network analyser. It can perform broadband swept spectrum measurements as well as narrowband-zoom measurements, both of which are necessary for analysis of ion motion and resonances. The analyser is also equipped with the time-gated sweep option for both measurement types, necessary for observing ion cyclotron or axial resonance directly after excitation.

3.3. Trap loading

An important feature of the SpecTrap ion trap is the ability to trap externally produced ions. Therefore, the trap is kept geometrically open, but it also requires specialized potential switching for establishing ion confinement in all dimensions of space. This section will describe one such typical experimental cycle, where ions are captured in-flight, compressed towards the trap centre and ejected for counting.

3.3.1. Dynamic ion capture

Externally produced ions in SpecTrap have to be injected into the Penning trap along the magnetic field axis, set as the z-axis of the system. Radial confinement is in that case provided by the magnetic field, and ion capture is realized along the z-axis by changing the axial trapping potential as depicted in Fig. 3.9.

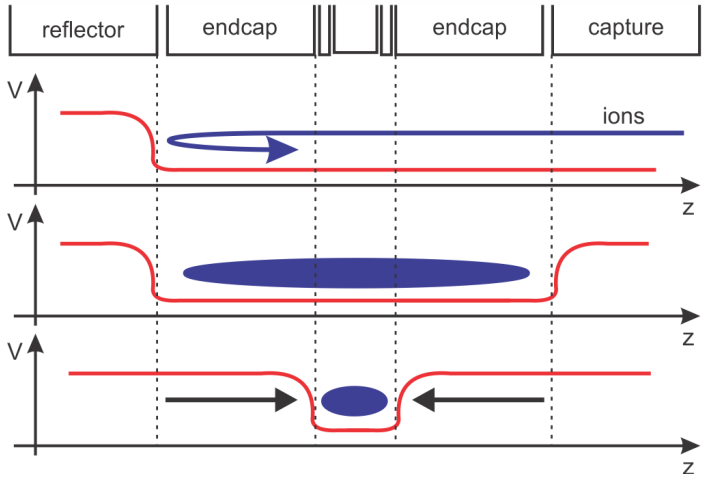

Figure 3.9: Illustration of one dynamic ion capture cycle. Ions (in blue) are guided into the trap, with all but the reflector electrode grounded. Axial confinement is established after raising the capture electrode potential. The trapped ion cloud can then be compressed towards the trap centre by slowly raising the endcap potential. The potential (in red) is drawn for illustrative purposes only and does not correspond to the real trap depth.

An ion bunch with a charge q per ion, created and extracted from an external source with energy $E = qV$ and temporal spread Δt, passes the grounded capture electrode, enters the trap and gets reflected by the second capture electrode (in further text the reflection electrode). The bunch is then confined by rapidly raising the potential of the capture electrode. The maximum bunch size which can be captured in such way is called *trap acceptance*, and it can be defined with the time an ion needs to make a round trip inside the trap

$$\Delta t = \sqrt{\frac{2m}{qV}} L \tag{3.9}$$

where m is the mass of the ion and $L = 65.6$ mm the distance between the capture and the reflector electrode. For extraction voltages up to 1 kV and larger ion mass-to-charge ratios, this time is of the order of a μs. For instance, the trap can accept 200 eV ion bunches with temporal spread of

$$\Delta t(^{24}\mathrm{Mg}^{+}) = 1.6\ \mu\mathrm{s}; \qquad \Delta t(^{40}\mathrm{Ar}^{+}) = 2.1\ \mu\mathrm{s}; \qquad \Delta t(^{208}\mathrm{Pb}^{+}) = 4.8\ \mu\mathrm{s}.$$

However, ions with smaller mass-to-charge ratio are much faster for the given energy (per unit of charge), and the trap acceptance becomes

$$\Delta t(^{40}\mathrm{Ca}^{14+}) = 0.56\ \mu\mathrm{s}; \qquad \Delta t(^{208}\mathrm{Pb}^{81+}) = 0.53\ \mu\mathrm{s}.$$

By taking into account that typical ion transport energies in SpecTrap are of the same order of magnitude as used in this calculation, or even larger, ion bunches which have a temporal spread that is larger than the calculated values either have to be cut, limiting the capture efficiency, or decelerated by the drift tube in front of the trap (drift tubes are described in section 4.3.3).

The described process establishes ion trapping between the capture electrodes. However, SpecTrap requires well-defined ion oscillation frequencies and decoupled motional energies, hence ion confinement between the endcap electrodes has to be established. This is relized by adiabatically raising the endcap potential, which compacts the trapped ion cloud in the trap centre without changing its energy. The potential rise can be considered adiabatic if the voltage rise time is smaller than the ion oscillation period. Simultaneously, the voltage of the correction electrodes is also adjusted to ensure a harmonic oscillation.

It is obvious that a fast rise time and precise triggering of the electrode potentials are of crucial importance for capturing a bunch of externally produced ions. Trap timing and triggering of the potentials is controlled by two DG 535 digital delay generators, with a precision better than 10 ps. Raising the potential of the capture electrode within a μs requires high-voltage switches, and three home-made switches with an internal rise time of 10 ns are used for this purpose. With the additional capacitances of the cables and the electrodes, a rise time of the order of 200 ns is obtained, which is even fast enough for the small mass-to-charge ratios. The switches are triggered by the ion arrival detector described before, or alternatively by measuring the time of flight between the ion source and the trap. On the other hand, the rise time of the endcaps needs to be comparably slow in order to ensure an adiabatic compression. Hence, the exact timing of the switching trigger is less important, since it only has to arrive after closing the trap. The desired slow rise time is provided by the electronic components that filter the voltage signals applied to the endcaps. According to Tab. 3.2, the rise time is of the order of 200 μs, which is much longer than the typical ion axial oscillation period.

3.3.2. Multiple ion bunch capture - ion stacking

In the previous section a single ion dynamic capture cycle was described, where the total number of trapped ions is limited by the number of ions in a single bunch. In order to increase the fluorescence signal it is desirable to capture as many ions as possible, and the SpecTrap ion trap was designed to store large ion clouds. However, it is not always possible to produce a satisfactory number of ions in a single bunch, and the only solution is capturing multiple ion bunches, also known as *ion stacking* or *ion accumulation*.

The main difficulty of the technique is that the capture electrode needs to be reopened, i.e. its potential lowered, to admit the next bunch. This gives the ions that are already stored a possibility to leave the trap. It can be readily seen that the potential of the capture electrode needs to be gated and not switched, meaning that it is constantly kept high and lowered only long

enough to allow the new bunch to enter. In a simplified picture, the theoretical maximum number of stored ions is reached when an equilibrium between gain and loss processes is established, i.e. when the number of newly captured ions equals the loss during the capturing event. If a single bunch has n ions equally distributed in time and its size relative to trap acceptance is α, the maximum number of stored ions is

$$N = n \cdot \sum_{k=0}^{\infty} (1-\alpha)^k = \frac{n}{\alpha} \qquad \text{for } \alpha < 1. \tag{3.10}$$

In other words, if the bunch is two times smaller than the trap acceptance, the maximum number of stored ions is $2n$. In reality this number will be even smaller because of phase, timing and energy dispersion, and the result of Eq.(3.10) can be taken only as an upper limit.

The number of trapped ions can be improved if the ions are prevented from leaving the trap while the capture electrode is open. The necessary condition is that a cooling mechanism is present between two openings of the capture electrode. Instead to ground, the potential of the capture electrode is lowered only to a value which prevents already stored and pre-cooled ions to leave the trap, but allows new ion bunches to enter, as shown in Fig. 3.10. The maximum is reached when the ion loss between two capture events equals the number of ions in a single bunch, and it is typically much higher than any possible result of Eq.(3.10).

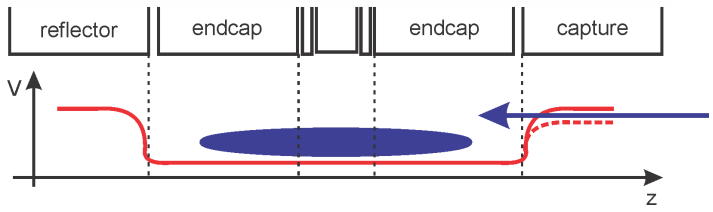

Figure 3.10: Ion stacking procedure with cooling, where the potential of the capture electrode is lowered to a non-zero value, enough to admit new ions into the trap, but still high enough to prevent the pre-cooled ions from escaping the trap.

During the process of stacking, the ions are stored between the capture electrodes with an energy which is of the same order as the transport energy. Laser cooling is rather inefficient under these conditions - due to the large Doppler shift, ions can interact with a laser beam only around the turning points in the trap when their velocity approaches zero. SIMION simulations have shown that a trapped 200 eV Mg ion will be on average for 2 ns in the necessary velocity domain in order to absorb a photon from a laser red detuned by 1 GHz. In this period of time an ion can on average absorb only a single photon per turning point, which translates into several eV deceleration per second for a typical ion axial oscillation frequency of 500 kHz. However, ion axial energy can still be reduced by transferring a part of it into the radial energy, as will be discussed in section 4.3.3 and Eq.(4.8). This is provided by non-parallel ion propagation axis and magnetic field lines during the injection process, as well as by non-harmonic trapping conditions between the capture electrodes and energy mixing according to Eq.(2.30) after closing the trap. It was experimentally observed that around 50 eV out of 200 eV is transferred into radial motion through these mechanisms (see section 6.2.1), which is sufficient for the described ion accumulation technique.

3.3.3. Ion ejection and counting

Based on the same principle as ion dynamic capture, SpecTrap also offers the possibility to extract trapped ions if the process in Fig. 3.9 is reversed. The potential on the endcaps and correction electrodes is lowered to ground, and ions are pushed out of the trap by a rapid drop of the reflector electrode potential. As during ion capture, the time scales of the potential changes are significantly different: the change at the inner electrodes has to be adiabatic, or slow in comparison to ion motion in order not to perturb it, while the reflector electrode potential has to be lowered ideally within one ion oscillation period inside the trap.

A retractable micro channel plate (MCP) is located beneath the trap and the magnet. It is used to monitor ion transport through the beamline or to detect ions ejected from the trap. The detector can be operated in two modes: standard counting mode for lower rates, or a Faraday-cup mode for large signal rates. On overview of the two modes is given in Fig. 3.11. If both plates of the detector are biased with a high voltage (left in Fig. 3.11), incident ions create 10 ns electron avalanches, which are seen as a voltage drop across the anode. The signal from the anode is then amplified, discriminated and sent to a counter. Continuous count rates up to 1 Mcps can be measured in this mode before the detector starts showing saturation effects; pulsed rates can be as high as 100 kcps, depending on the pulse duration. Higher count rates remain hidden in the detector's dead time and can in extreme cases lead to overloading and damage of the channel plates. An alternative detection method is possible at high currents (right in Fig. 3.11). There, the first channel plate is used as a Faraday cup, without any bias voltage and the collected ion current gives rise to a voltage drop across a resistor, which can be amplified or directly observed. The resulting signal is in that case directly proportional to the product of ion number and charge, which becomes especially pronounced for large ($N \gg 100$) bunches of highly charged ions.

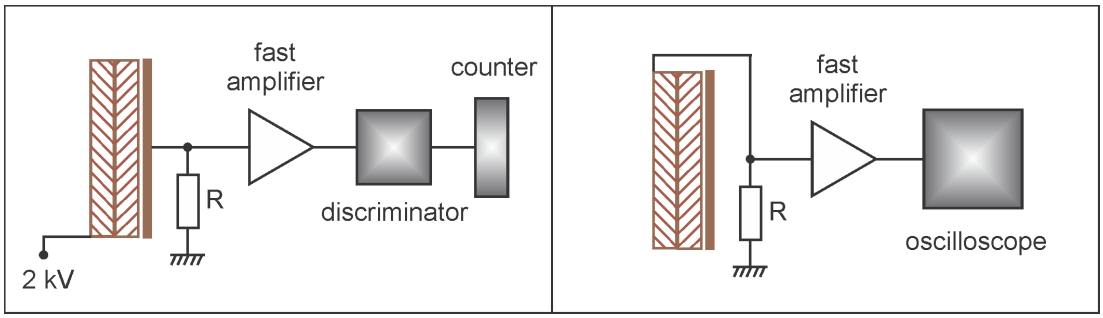

Figure 3.11: Two modes of micro channel plate (MCP) operation. Counting mode (left), where a voltage bias across the channel plate stack creates an electron avalanche, and the Faraday cup mode (right), where the ion current is collected directly from the front plate.

Finally, it should be noted that propagation of ions ejected from the trap, as well as transport through a grounded trap, is strongly influenced by the large magnetic field gradient present in the region. As will be discussed in section 4.3.3, the cyclotron radius of an ion is inversely proportional to the square root of the magnetic field. Consideration of this effect is very important for interpretation of experimental results, especially if the ion motional energies are allowed to mix inside the magnetic field, leading to an increase in the cyclotron radius.

3.4. Overview and limits in mass and ion number

The SpecTrap ion trap, together with its associated electronic parts, was assembled according to the specifications given in the previous sections and mounted into the superconducting magnet described in the next chapter. A photo of the complete ion trap assembly before installation is shown in Fig. 3.13. Since the installation requires breaking the vacuum and a complete disassembly of the ion beamline and magnet housing, it is not desirable to repeat it often. Therefore, the aim was to design the trap and the electronics sufficiently flexible for a broad range of experimental concepts, differing mostly in ion number, energy, mass and m/q ratio. It can be seen from Fig. 3.12 that the frequency of the ion axial motion can be tuned to resonance with at least one of the axial coils for all mass-to-charge ratios up to ∼35. This is necessary both for effective resistive cooling and non-destructive detection of ion axial motion, and it sets the upper limit for the mentioned techniques. However, although they cannot actively interact with the resonant circuits, ions with an even higher m/q ratio can still be stored and used for experiments. The detection is in that case limited only to destructive or optical methods and energy reduction to sympathetic cooling. Singly charged ions with larger masses become increasingly more difficult to store, and the upper limit is set by the maximum trap depth for a given magnetic field, which can be calculated from Eq.(2.17).

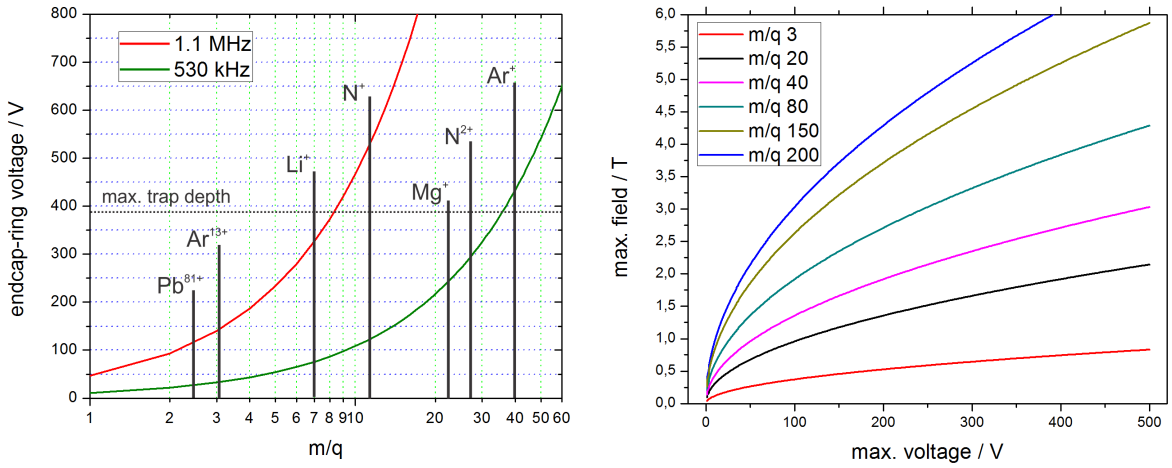

Figure 3.12: Left: voltage necessary to bring the ion axial motion of different mass-to-charge ratios into resonance with one of the two resonant circuits. The dotted line marks the maximum trap depth, as discussed in section 3.1.1. Right: maximum voltage that can be applied between the endcaps in order to ensure stable trapping conditions for a given magnetic field, calculated according to Eq.(2.17). Several lines were plotted for different m/q ratios, in units of elementary mass over elementary charge.

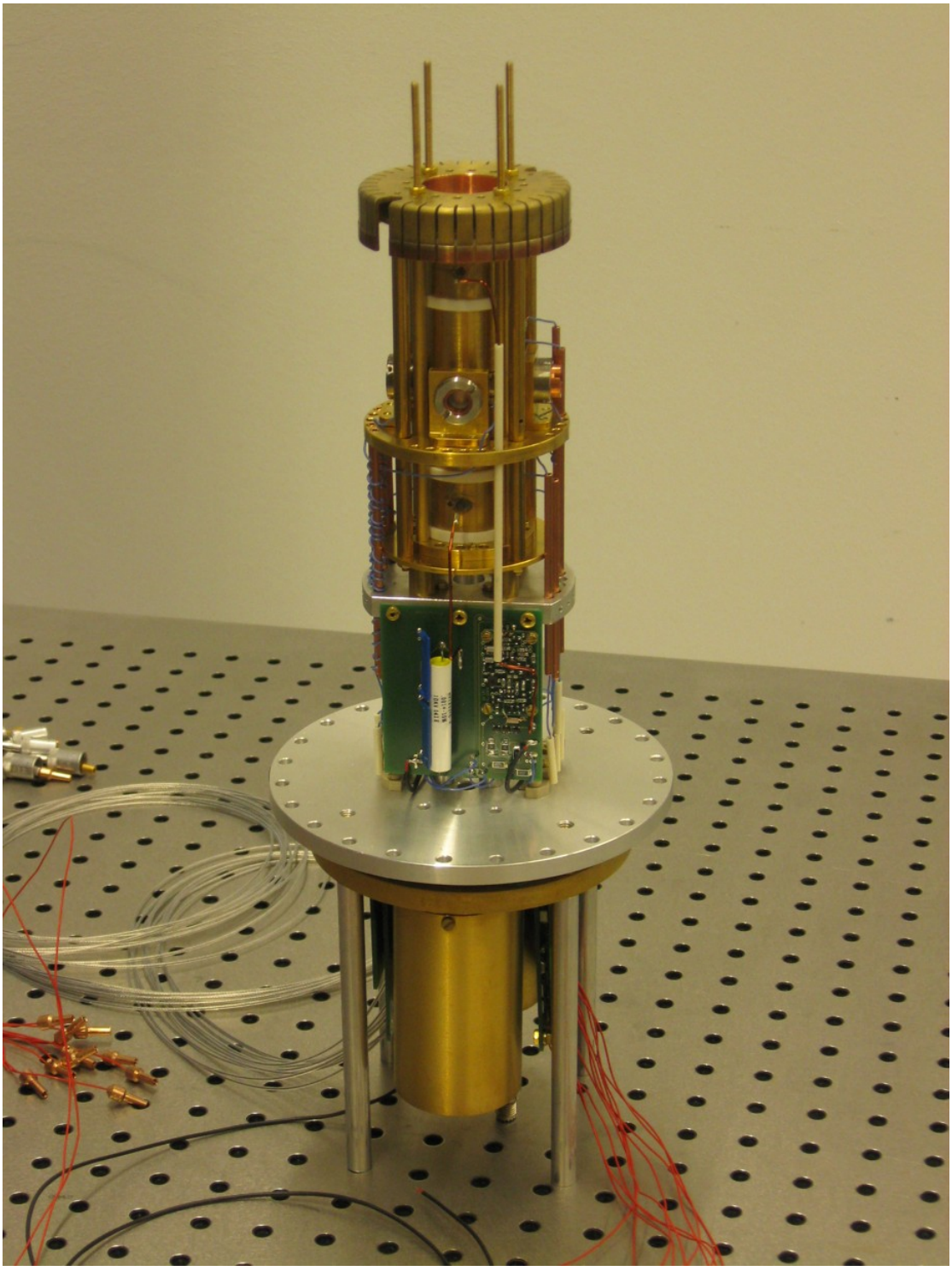

Figure 3.13: A photo of the complete ion trap assembly, together with the cryogenic electronics, taken prior to mounting into the magnet. The design follows the technical drawings from Figs. 3.1 and 3.2. The electronic board seen in the front contains the arrival detector and the filter for the reflector electrode. The biggest part of the electronics is located on the gold-plated mount under the main aluminium flange. Connected directly to it from the lower side are the two coils inside gold-plated housings, as well as two filter boxes. Connected to the latter are two sets of cables - coaxial in metallic colour and standard non-shielded ones in red. The black cables are the two HV lines for the capture and reflector electrodes.

Chapter 4

Experimental requirements for laser spectroscopy in a Penning trap

Laser spectroscopy and Penning trap ion confinement are two powerful experimental techniques, which, however, cannot be easily combined. For instance, if the trap consists of cylindrical electrodes, as in the case of SpecTrap, laser light can be introduced axially, but because of the superconducting magnet coils there is usually no independent axis left for detection of ion fluorescence. An additional difficulty is the external production of ions, which need to be transported and stored, with a system flexible enough to accept different q/m ratios and energies. SpecTrap reconciles all these often contradictory requirements and offers an experimental setup which can be used for a broad spectrum of measurements, both with locally produced low-charge ions and highly charged ions decelerated in HITRAP.

This chapter describes the experimental equipment needed for operation of the SpecTrap Penning trap described in chapter 3, external ion production and investigation of their interaction with laser light. The SpecTrap experimental setup can be divided into three main parts

- the superconducting magnet and the LHe cryostat[1],
- the ion production and transportation setup and
- lasers and fluorescence detectors

and the following sections address them accordingly.

4.1. The SpecTrap superconducting magnet

The magnetic field required for stable operation of the SpecTrap Penning trap is provided by a Nalorac NMR[2], vertical, cold-bore, split-coil superconducting magnet, calibrated to roughly 0.1 T/A field strength. Even though superconducting magnets are expensive with respect to both purchase and operation cost, they are the best option for producing strong magnetic fields

[1] Consigned to GSI in collaboration with Lawrence Livermore National Laboratory and Texas A&M University

[2] NMR stands for nuclear magnetic resonance. Such magnets are standard commercial tools for medical or research applications.

of $B > 1$ T. Besides the absence of resistive losses in the coils, superconducting magnets provide a very high field stability and homogeneity, as compared to electromagnets which are inevitably influenced by the electrical noise of the power supplies.

The magnet coil of the SpecTrap magnet is made out of a single Niobium-Titanium wire with several thousand windings in the so-called split-coil (Helmholtz) arrangement. This is a special feature of the magnet allowing for six radial optical ports to the homogeneous field region. The coil is mounted inside a 50 l liquid helium reservoir, with a 76.2 mm (3") central bore in which the trap and further experimental equipment is located. A cross-section of the SpecTrap magnet and cryostat with the specifications is presented in Fig. 4.1 The vacuum of the bore is the same as the insulating vacuum of the chamber, enabling cryopumping of the system and a direct cooling of the inserted trap and the associated cryogenic electronics.

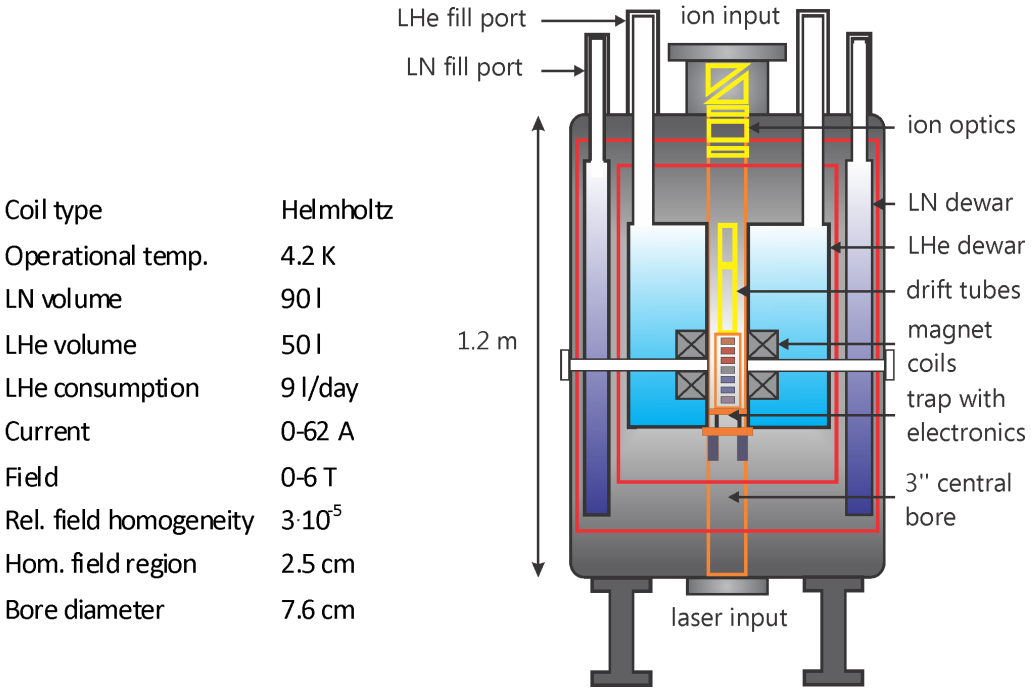

Figure 4.1: Cross section of the Helmholtz-type superconducting magnet used in SpecTrap. It shows the internal layer structure of the magnet with the cryogenic liquid reservoirs and radiation shields (in red). The split coil configuration can be seen, which allows installation of radial ports (six in total) for direct optical access to the trap centre. Indicated are also the ports used for injection of external ions and laser radiation. Besides the ion optics and the trap, the diagram is true to scale.

Several intermediate temperature stages around the liquid helium reservoir are necessary to avoid a direct thermal contact to room temperature and therefore a huge helium evaporation rate (see appendix A.3). The liquid helium reservoir is therefore surrounded by a passive radiation heat shield, which represents the next temperature stage and decreases the radiation heat load to the main chamber. The emissivity coefficient of both the LHe reservoir and the radiation shield was further decreased with an additional layer of highly reflective aluminium foil. The final temperature level before room temperature is defined by a 100 l liquid nitrogen reservoir and a second passive radiation shield around it.

The whole magnet and cryostat system is suspended from the mounting flange on the top, with a diameter of 800 mm. Thermal contact between different temperature stages is established only inside the liquid helium fill ports. Next to them are the liquid nitrogen fill ports, which however provide no mounting support and are in thermal contact only with the LN reservoir. There is a pair of both LN and LHe fill ports, and one set of ports is used for filling the cryogenic liquids, while the other is used for venting. The mounting flange contains also HV feedthroughs for the drift tubes, the central flange for connecting the magnet chamber with an external beamline and a spare flange.

The bottom side of the magnet chamber is closed with another $\varnothing = 800$ mm flange, but with no contact to any of the low temperature stages. It houses several smaller openings used for different purposes - vacuum pumping, a pressure monitor, a flange with electrical feedthroughs and the central flange of the bore which is used for ion ejection and coupling of a laser beam.

4.1.1. Cryogenic design of the system

Due to the rising price of liquid helium and the fact that its latent heat of evaporation is extremely low, every cryogenic system needs to be carefully designed in order to minimize losses. There are two main contributions to the energy flow, i.e heat load, into the cryostat. These are:

1. thermal black body radiation between parts of the system at different temperatures and
2. thermal conductivity along the material connecting different temperature stages.

A possible third transfer mechanism - convection through gas particles - can be safely neglected due to the vacuum insulation of the cryostat.

The surface of the SpecTrap liquid helium reservoir is 1 m^2 and of the first radiation shield 1.6 m^2 and their estimated respective temperatures 4 and 20 K. Using Eq.(A.5) and Tab. A.4 it can be easily calculated that the radiation heat load to the liquid helium reservoir is only 0.3 mW, which is quite low in comparison to the specified total load of some 300 mW. The SpecTrap magnet also has a total of six radial windows 2.5 cm in diameter, which establish direct optical contact between room temperature and the liquid helium reservoir. The heat load from a single window can be estimated using Eq.(A.4) and amounts to some 3 mW. Since four windows were internally blinded at all temperature stages for purposes of this work, the heat load coming from the optical ports is around 6 mW, which is also low in comparison to the total load.

Special care was taken choosing the electrical feedthroughs and vacuum-side cables. They have to fulfil several requirements:

- high-frequency compatibility, i.e. they need to be coaxial shielded cables,
- high electrical conductivity, i.e. low internal resistance,
- low thermal conductivity, i.e. they need to be cryogen-friendly, since they establish a direct connection between the room temperature environment and the cryostat,
- vacuum compatibility, i.e low outgasing rate.

These conditions are very difficult to fulfil simultaneously since good electrical conductivity is usually accompanied by good thermal conductivity and the shielding of coaxial cables typically has a high thermal load compared to the cable core. A solution was found in the cryo-coax cable GVLZ081[3] with a thin central conductor made out of copper and a copper-nickel mesh around it, as shown in Fig. 4.2. Unshielded cables were used where it was not necessary to transfer high-frequency signals. The cable of choice was a PTFE insulated constantan cable with specific thermal conductance of only 300 μW/m. This cable was also used for the high-voltage lines, but reinforced with an additional 0.25 mm insulation layer. The main characteristics of the cable connections used in SpecTrap are listed in Tab. 4.1.

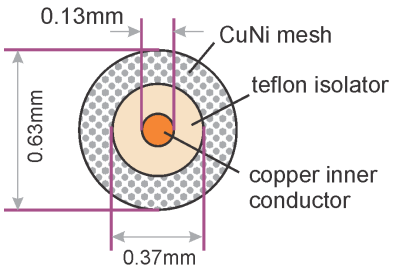

Figure 4.2: Cross-section of the GVLZ081 CryoCoax cable. The inner conductor is actually a twisted pair of two copper wires with a thin layer of Kapton coating. Around the CuNi shield there is an additional thin Teflon coating.

Table 4.1: Specifications of electrical connections used in SpecTrap and a comparison to standard copper cables with the same voltage ratings.

type	thermal cond. [mW/m]	voltage rating [V]	length [m]	no. used
CryoCoax	1.2	800	1.5	11
Constantan	0.3	1100	1	12
copper coax.	7	800	1.5	0
copper standard	3.5	1100	1	0

Summing up the thermal radiation, optical windows and the heat load from the cable connections, the total load of the SpecTrap magnet should be some 25-30 mW, which would result in only 0.8 to 1 l daily helium consumption. In reality this number was found to be about 9 l/day, which is an order of magnitude bigger. The reason lies in the remaining thermal conductivity through the liquid helium fill lines, shield joints and the transition spokes that hold the different shields together. Nevertheless, it was shown how critically important the thermal design of a cryostat is, and that neglecting just a single aspect like electronic wiring could easily double the expensive cryogen consumption.

Finally, although not relevant for helium consumption of the system, it should be noted that the coaxial cables were all terminated with MDC 9922135 type D cable termination kits. This was important because only that model provided the needed flexible vacuum side connection, with full electrical shielding, but still mechanically sensitive enough for the very fragile GVLZ081 CryoCoax cables.

[3]Distributed by the company GVL Cryoengineering.

4.1.2. Magnetic field of Helmholtz coils

In a so-called Helmholtz magnet configuration the current is guided through two identical spiral loops around the magnet centre rather than a closed solenoid. The two coils are placed on a common axis, spaced by distance l equal to their radius R, as illustrated in Fig. 4.3. The electrical currents in the two coils are equal and flow in the same direction (as opposed to the anti-Helmholtz configuration).

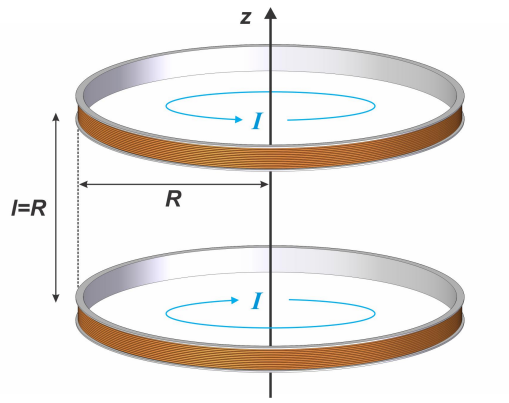

Figure 4.3: An illustration of the Helmholtz coil configuration. The radius R of the coils is the same as the spacing between them and they conduct an equal current I. Real Helmholtz coils (magnets) are however significantly different from this picture, since they typically contain several thousands windings on top of each other.

The magnetic field of two Helmholtz wires can be calculated according to the Bio-Savart law along the coil axis and is given by

$$B_z = \frac{\mu_0 I}{2R}\left[\frac{1}{\left(\gamma^2+\gamma+\frac{5}{4}\right)^{3/2}}+\frac{1}{\left(\gamma^2-\gamma+\frac{5}{4}\right)^{3/2}}\right] \tag{4.1}$$

where $\gamma = z/R$ is the ratio of the distance from the centre and the coil radius, $\mu_0 = 4\pi \cdot 10^{-7}\ \frac{\mathrm{T\cdot m}}{\mathrm{A}}$ the permeability of free space and I the current. A good approximation for calculating the on-axis magnetic field of a real Helmholtz magnet can be made using Eq.(4.1) and the current I multiplied by the number of coil windings n. The results for the SpecTrap magnet ($R = 3.81$ cm) are plotted in Fig. 4.4 together with SIMION simulation results. It can be seen that the simulated field in the near field region drops faster than the calculated one, which can be explained by non-ideal, radially extended coils - an effect that is not considered in Eq.(4.1). The design value of the 2.5 cm long homogeneous field region is well reproduced by the simulation. This size is sufficient for ion confinement since the expected ion oscillation amplitudes are of the order of a few mm. Further away from the centre the simulation and calculation results are similar. This is shown in Fig. 4.4 right and was expected since at larger distances coil imperfections become less visible. It can be seen that the field drops quite rapidly, which is typical for Helmholtz coils. This steep gradient has to be considered for successful injection of externally produced ions, as will be discussed in section 4.3.3.

In the special case of $z = 0$, Eq.(4.1) becomes

$$B_0 = \left(\frac{4}{5}\right)^{3/2}\frac{\mu_0 n I}{R}. \tag{4.2}$$

Since the exact number of coil windings is not known, a value of $n = 4200$ has been chosen. According to Eq.(4.2), this results in a value of $B = 6$ T for a current of $I = 60$ A, which resembles the field of the SpecTrap magnet.

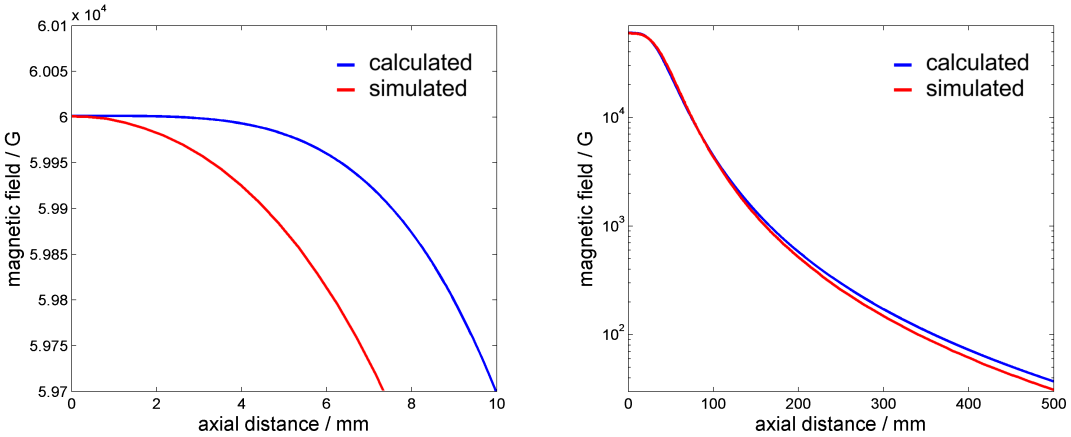

Figure 4.4: Axial magnetic field of the SpecTrap Helmholtz coils, calculated (blue) according to Eq.(4.1) and simulated with SIMION (red). Two typical areas of interest are shown - close to the trap centre (left) and the fringe field outside the magnet (right). The $z = 0$ field is scaled to 6 T.

An analytical solution for the magnetic field at an arbitrary point in space has a much larger mathematical complexity, but it is here not of large interest. Important is only the radial field at the $z = 0$ plane, since it can potentially disturb other instruments mounted close to the magnet (like a photomultiplier). A SIMION simulation of the magnetic field strength along the $z = 0$ plane was done to that end, and the results are plotted in Fig. 4.5. The left graph shows that the magnetic field is quite homogeneous over the extent of the central bore ($r = 38.1$ mm), especially in the region where ion trapping is expected, i.e. $r \leq 10.5$ mm - the inner radius of the trap electrodes. However, the fringe field on the outer edge of the magnet vessel ($r = 400$ mm) is still close to 100 Gauss, which is also in reasonable agreement with the measured fringe field of about 60 G. At such field strength normal operation of many photomultipliers is not possible, and they have to be either mounted farther away or equipped with appropriate magnetic shielding.

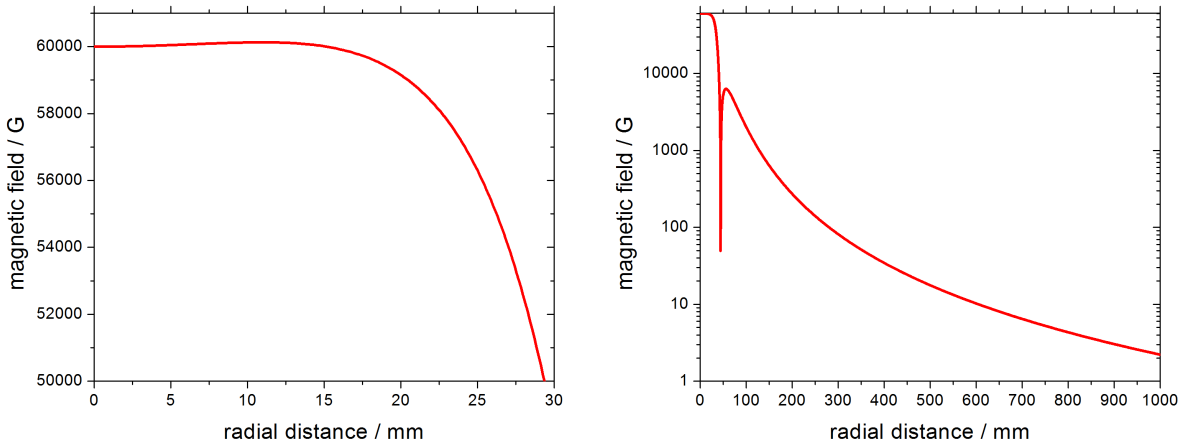

Figure 4.5: Magnetic field of the SpecTrap Helmholtz coils for $z = 0$, plotted for the close (left) and far field region (right). The $r = 0$ field was scaled to 6 T. The field drop around $r = 40$ mm is inside the region of the coils themselves. Both graphs are SIMION simulation results.

4.2. The ultra-high vacuum system

The storage time of an ion or an ion cloud inside a Penning trap is directly dependent on the residual gas pressure [59]. Therefore special care was taken in the design and assembly of the SpecTrap vacuum system. Due to the specific vacuum and temperature requirements of the system, several different types of vacuum seals were used across the vacuum chamber. They include:

1. standard copper sealing, with flange sizes ranging from CF16 to CF150
2. home-made PEEK® gaskets for sealing of flat surfaces
3. high-purity, thick aluminium foil, for sealing of the CF800 mounting flange
4. Armstrong A-12 epoxy for sealing of the LN and LHe reservoir joints.

The SpecTrap vacuum tubing and magnet housing was constructed out of 304 and 316 stainless steel because of its favourable outgassing properties. The beamline guiding the ions into the magnet, described in the next section, and the connecting ports on the magnet vessel were based on the CF100 flange size. All the joints were carefully cleaned of residual impurities and sealed with a knife edge pressed into a copper gasket.

Because of its size ($\varnothing = 800$ mm), it was not possible to seal the top mounting flange with a knife edge and a copper gasket. An alternative was found in high purity, thick aluminium foil, shown in Fig. 4.6. The gasket is prepared by cutting out a large piece of aluminium foil and

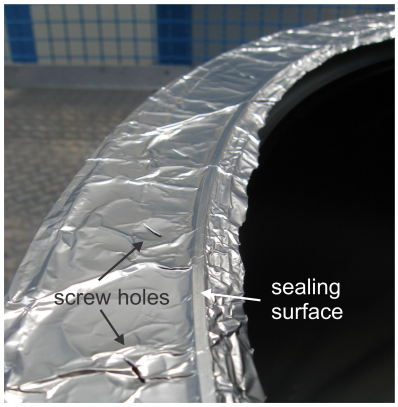

Figure 4.6: A section of the aluminium foil sealed top flange of the SpecTrap magnet. Although the foil is overall of an irregural shape, the sealing surface was checked for imperfections and additionally flattened by fingers and soft sandpaper. The screw holes have a cut through each, for easier insertion of screws after joining the two flanges.

placing it on the top of the (empty) SpecTrap magnet housing. It is then checked to be hole and wrinkle free on the area of the sealing edge and additionally flattened using fingers and fine sandpaper. After cutting out the screw holes the gasket is ready for the mounting flange.

The LN and LHe fill ports, as shown on Fig. 4.7, required non-conventional sealing techniques due to the special vacuum and temperature conditions. The lower part of the ports was screwed into the corresponding fine-thread station on the reservoirs and sealed with Armstrong A-12 two component epoxy (Fig. 4.7 left). The mixing ratio of 1:1 was chosen such to obtain a more rigid bond and better vacuum sealing and cured for 1 hour on 100 °C and 1 week on room temperature. The sealing of the upper part of the fill ports was originally designed with Helicoflex® C-seals

(Fig. 4.7 right). Because of their high cost they were at a later stage replaced with self made PEEK® seals of the same basic form [60].

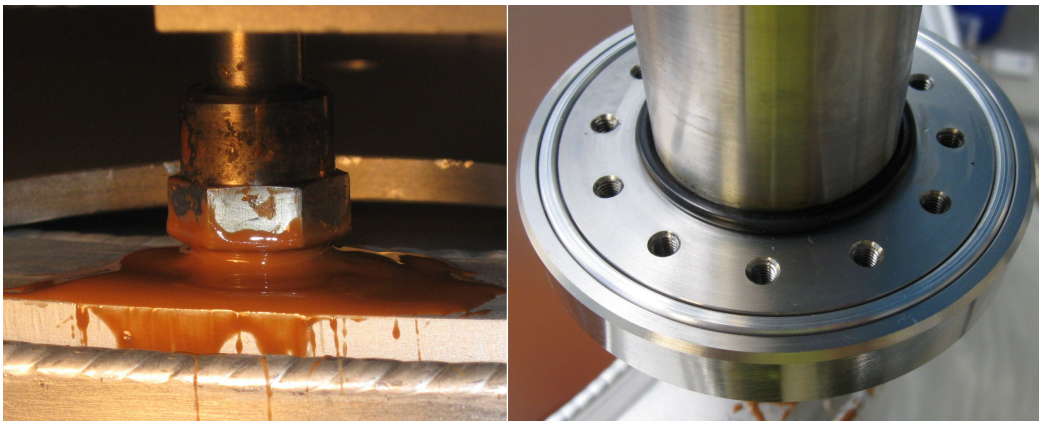

Figure 4.7: The two sealed contacts on the liquid nitrogen fill ports. Left is a picture of the epoxy sealed lower part of the port. Right is a two stage sealing surface with a Helicoflex® seal, which was later replaced with a PEEK® seal.

The main part of vacuum pumping was done with an EBARA ET-300-WS and a BOC Edwards EXT250M turbo molecular pumps, mounted on the bottom and top of the system, respectively. They were backed with two BOC Edwards RV5 rotary vane pumps. Additional pumping was provided by two Varian 300 l/s ion getter pumps.

After sealing, the system was baked on a turbo molecular pump for one week in order to reach the needed ultra-high vacuum conditions. The baking temperature was limited by the A-12 epoxy, which remains rigid up to maximum 150 °C (it should be noted that in the opposite extreme, the epoxy remained rigid even after multiple cooling cycles to liquid nitrogen temperature). This was enough to reach a residual pressure of $1 \cdot 10^{-7}$ mbar, which dropped further to $2 \cdot 10^{-8}$ mbar after another month of pumping and switching on the ion getter pumps. Introduction of cryogenic liquids during magnet operation and the associated cryopumping decreased the pressure to a value of $5 \cdot 10^{-9}$ mbar. It is important to emphasize that the pressure sensors giving these readings were located in the warm region. The pressure in the cold bore of the magnet was significantly smaller (as will be discussed in section 6.2).

4.3. SpecTrap ion beamline

The SpecTrap beamline serves two purposes: in a later stage, when SpecTrap is connected to the HITRAP facility, it will be used to receive highly charged ions that are delivered from the cooler trap or the EBIT and guide them into the Penning trap. Additionally, for purposes of this work, it contains a local ion production and transport system, conceived so that locally produced ions can be transported into the trap. Before the details of the beamline are discussed, an overview is given in Fig. 4.8.

Starting from the top of Fig 4.8, low-charge-state ions can be produced by two different ion sources, described in the next section. An ion beam can be shaped with help of two einzel lenses

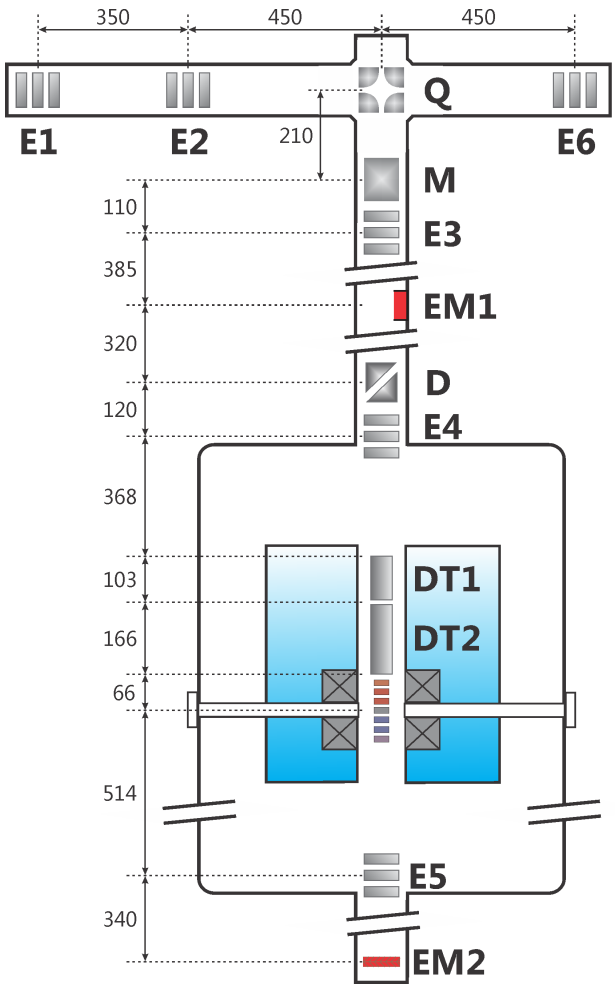

Figure 4.8: Diagram of the SpecTrap beamline with ion optic elements. Legend:
Ex - einzel lens
Q - quadrupole bender
M - multipole
EMx - electron multiplier
D - deflector
DTx - drift tube
Ions are injected through the horizontal part of the beamline on top, either from the left (SpecTrap ion sources) or the right (HITRAP or any other source), and deflected towards the magnet and the trap. The units of the indicated distances are millimetres. The diagram is true to scale.

(E1 and E2), before reaching the 90° quadrupole bender, where it is guided down into the vertical part of the beamline. This bender has been chosen because of its flexibility - with a correct choice of the potentials the ion beam can be deflected either way from any of the four entrance points, including transmission in forward direction when the electrodes are grounded. This means that a mere polarity switch is in principle enough to bend an ion beam coming both from SpecTrap and from HITRAP. Ions arriving from HITRAP will enter the beamline from the right hand side of Fig. 4.8. Here, the einzel lens E6 can be used for beam shaping additionally to the ion optics in the connecting beamline. In that way both locally produced ions (like Mg^+ for laser cooling) and highly charged ions from HITRAP can be trapped at the same time. The bender electrodes also do not disturb a laser beam, which is coupled from the bottom flange of the magnet through the trap centre and the vertical beamline.

After bending, an ion beam typically gets slightly focused on one axis and defocused on the other. To correct for this asymmetry, a multipole is installed directly behind the bender. Two more einzel lenses in the vertical beamline (E3 and E4) guide the ions into the magnetic field of the superconducting magnet and eventually into the trap. Finally, two drift tubes (DT1 and DT2) are located in the central bore of the magnet in front of the trap, which can be used to decelerate an ion bunch.

Fig. 4.8 also shows the position of two secondary electron multipliers (EM1 and EM2), used for ion detection. A channeltron® (EM1) was placed between the quadrupole bender and the magnet, where it can be used to check the efficiency of ion transport and bending, before entering the strong magnetic field region. If it is switched off and grounded, because of its off-axis mounting position, the channeltron blocks neither the laser beam, nor the ion beam. A micro channel plate (MCP or EM2 in Fig. 4.8) is located on the far end of the beamline behind the trap. There it is used to monitor ion transport into and out of the strong magnetic field, or to count ions ejected from the trap. An einzel lens (E5) was installed under the trap to aid this process and re-focus the transported or ejected ions onto the MCP. Since the MCP blocks the laser beam path when used for detection it is mounted on a mechanical feedthrough so that it can be moved out of the central position.

4.3.1. Ion sources

Production of singly charged magnesium ions for purposes of laser cooling is accomplished with a self-designed ion source, shown in Fig. 4.9. It is a two stage source, where a beam of neutral particles is created in the first stage and then ionized in the second stage. The first stage is a cylindrical tungsten oven, resistively heated by a high current. It creates a cone-shaped beam of neutral particles which can be ionized by electron impact. This is performed in the second stage, where electrons emitted from a negatively biased filament (thoriated tungsten) are accelerated towards a positively biased grid. The electron energy is then defined by the potential difference of these two elements:

$$E_e = (|U_f| + |U_g|)e \tag{4.3}$$

where e is the elementary charge. Because of their small mass the electrons can penetrate the electrical field of the grid and ionize the neutral particles found inside. The half-open cylindrical geometry of the grid creates a potential gradient towards the open end and accelerates the created ions in the same direction in case of a positive bias $U_g > 0$. In order to enhance this process, a negatively biased extraction electrode is placed in front of the grid. Finally, an einzel lens collimates the emerging divergent ion beam, which is then ready for transport.

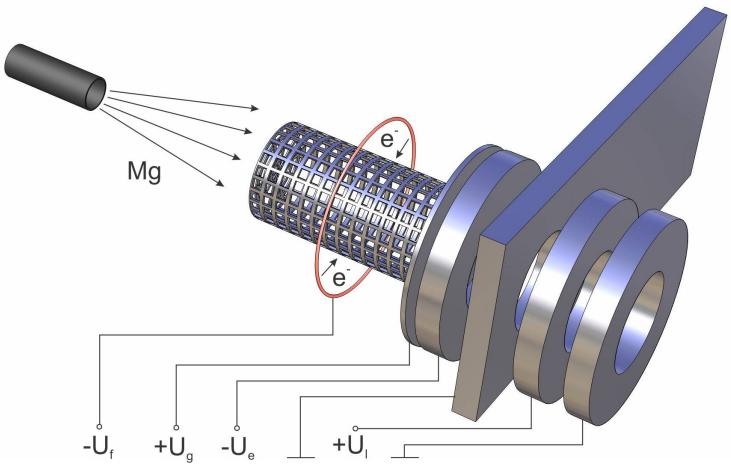

Figure 4.9: Drawing of the Mg ion source. It shows the oven producing Mg atoms, which get ionized by the electrons emitted from the filament. The signs of the applied voltages indicate the polarity of the corresponding element; U_e and U_l stand for extractor and einzel lens voltage, respectively. The rectangular electrode serves both as a ground reference and a mounting point.

A second ion source used in SpecTrap is a commercial RIBER model CI-10 N6199 sputter gun. The basic operation principle of this source is the same as illustrated in Fig. 4.9, but with a different (smaller) geometry of the ionizer and no neutral creation. Instead, the source works with inert gases, which are inserted through a needle valve just above the ionization region. It is significantly easier to operate than the Mg source and in SpecTrap it was used for production of several charge states of argon (Ar^{+} to Ar^{4+}) mainly for ion transport test. However, the beamline pressure increases significantly due to the introduction of gas into this source; an undesirable feature during magnet operation because of the gas flowing into the trapping region and freezing on the cold surfaces.

Both ion sources can be operated in a continuous and pulsed mode, depending on the way the grid voltage U_g is applied. If U_g is constantly on, the electron ionization energy is given by Eq.(4.3), and a continuous beam of ions with charge q at energy $E_i = U_g \cdot q$ is created. The situation is slightly different if the grid voltage is applied in short pulses. In that case most of the time $U_g = 0$ and ions are continuously created, but not accelerated. The electron ionization energy is then given by $E_e^{\text{pulsed}} = |U_f| \cdot q$, i.e. it depends only on the filament bias.

4.3.2. Ion optics

The ions created by external sources need to be transported into the trap through a 3 to 4 m long beamline. Taking into account a large span of desired transport energies (100 to 5000 eV/charge) this is not an easy task, and the system needs to have universal parameters which would ideally scale linearly with the energy. Propagation of ion beams can be described with a formalism similar to that of light propagation [61]. The steering elements used for it are called *ion optics*, following the same analogy. This section will give an overview of such elements, as used in SpecTrap.

An *einzel lens* focuses or defocuses an ion beam in a similar way as an optical lens focuses a beam of light. It comprises three hollow cylindrical electrodes, whose inner radius defines the aperture of the lens. A larger value insures smaller aberration effects in the lens, but also requires comparably higher operation voltages, which can take any value between a few tens of volts and several kV. As can be seen on Fig. 4.8, there are six einzel lenses in SpecTrap: E1 is the internal lens of ion sources from the previous chapter, E2 optimizes the ion beam for bending (same for E6 from the opposite side), E3 and E4 take care of magnetic field injection and E5 is used for optimization of ion transported through the magnet. Lenses E2-5 share the same design parameters, illustrated in Fig. 4.10, middle. The aperture of all lenses is 50 mm, the electrode length 30 mm and inter-electrode spacing 5 mm, providing a good compromise between beam envelope acceptance, aberration effects and voltage requirements.

An *electrostatic bender* is used to deflect an ion beam, typically in a 90° angle. It can be realized in two versions - as planar or quadrupole bender, and the latter version is used in SpecTrap. An ideal quadrupole bender comprises four hyperbolic electrodes in a quadratic array, with opposite potential on neighbouring electrodes. Since a hyperbolic shape is difficult to machine, a quadrupole deflector can be realized with four round electrodes and additional correction electrodes to compensate for a non-ideal potential. The type used in SpecTrap is quadrupole bender model QID-900 from the company Beam Imaging Solutions, shown in Fig. 4.11. It features also

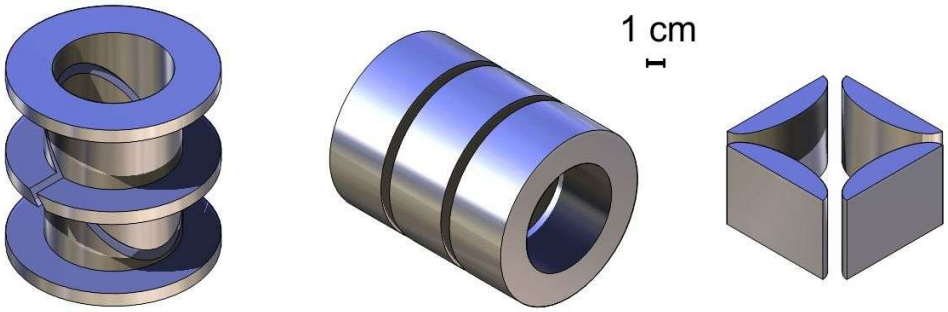

Figure 4.10: Drawing of a deflector, einzel lens and a multipole, respectively left to right, true to scale as used in the SpecTrap beamline.

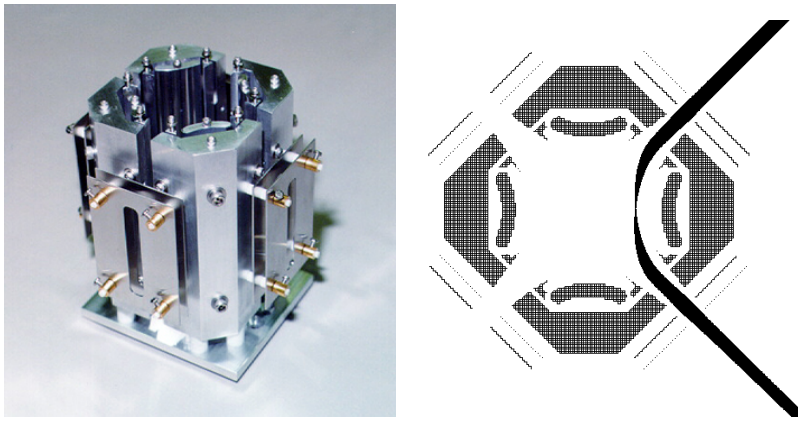

Figure 4.11: Left: a picture of the QID-900 quadrupole bender, the type used in the SpecTrap beamline. Right: a SIMION simulation picture of ion propagation through the bender. The electrode configuration can be clearly seen, as well as thin einzel lens electrodes on each entry/exit port of the bender. Pictures reproduced from the internet site of Beam Imaging Solutions.

a small einzel lens assembly for beam shaping in front of every ion input/output port.

The *multipole* M behind the bender consists of four hyperbolic electrodes, extended parallel to the ion propagation axis. It is the analogue of a cylindrical lens, which focuses light on a line instead of a point, and it is used to correct for astigmatism that may be introduced by the bender. It should be noted that a multipole doublet or a triplet can create a beam equally divergent in all directions and as such are used the same way as einzel lenses. They require however much lower potentials than einzel lenses since this electrode configuration is more favourable for creating transverse potentials needed for focusing and defocusing an ion beam.

The *deflector* D in front of the magnet is realized as a hollow cylinder diagonally split into two sections, which can be separately addressed, as illustrated in Fig. 4.10. It is used for final adjustment of the ion propagation axis before the injection into the magnetic field.

4.3.3. Ion deceleration and magnetic field injection

Ions delivered by HITRAP or the Dresden EBIT will have a transport energy of 5 keV/q. This value is too large for a dynamic capture in the SpecTrap Penning trap, and a system for reducing the ion energy prior to trap injection is required. It is realized with two extended drift tubes,

pulsed at an appropriate high voltage. If a bunch of ions with charge q enters the drift tube which is biased with a voltage U_{hi}, it will be decelerated, i.e. its kinetic energy will be reduced by $\Delta E = U_{\mathrm{hi}} \cdot q$. The bunch will regain the same amount of energy when leaving the tube, unless the tube bias is changed while the ions move through the field-free region inside the tube. If the tube potential is lowered to U_{lo} the ions will lose the energy $\Delta E = (U_{\mathrm{hi}} - U_{\mathrm{lo}}) \cdot q$ after they leave the tube. That is the principle of *pulsed drift tube ion deceleration.*

The beam emittance is a characteristic of every ion beam and has to be considered in order to properly understand what happens to an ion bunch during deceleration. Emittance is usually defined in the phase space of an ion: if the beam propagates in the z direction, its six-dimensional phase space $\{x, y, z, p_x, p_y, p_z\}$ can be broken down into two two-dimensional planes (x, p_x) and (y, p_y). The beam will then occupy the areas $S_x = \Delta x \cdot \Delta p_x$ and $S_y = \Delta y \cdot \Delta p_y$, and the beam emittance can be defined by normalizing these areas to the momentum in the direction of propagation p_z:

$$\epsilon_x = \frac{S_x}{p_z} = \Delta x \frac{\Delta p_x}{p_z} \qquad \text{and} \qquad \epsilon_y = \frac{S_y}{p_z} = \Delta y \frac{\Delta p_y}{p_z} \tag{4.4}$$

If $p_{x/y} \ll p_z$ then $\Delta p_x / p_z = \tan(\alpha) \approx \alpha$, where α is the angle of the beam envelope with respect to the propagation axis. This makes the emittance a measure of beam divergence.

It can be seen from Eq.(4.4) that a reduction of the longitudinal momentum p_z will lead to an increase in beam emittance. This is a direct consequence of Liouville's theorem, stating that the phase space volume stays constant under canonical transformations. The effect makes the pulsed drift tubes yet another ion optical element which strongly influences ion propagation through the beamline. A wrong setting of U_{hi} and U_{lo} can lead to strong focusing or defocusing and a complete loss of the ion beam. Simulations and praxis have shown that an optimal setting of these potentials for removing 90% of the ion energy E is around $U_{\mathrm{hi}} = +0.6 \cdot \frac{E}{q}$ and $U_{\mathrm{lo}} = -0.3 \cdot \frac{E}{q}$; a more detailed analysis can be found in [62].

In SpecTrap, the drift tubes are located inside the magnetic field, as can be seen in Fig. 4.8. Hence, ion deceleration and propagation is also strongly influenced by the large magnetic field gradient present in that region. In order to see what happens to an ion beam entering a magnetic field, it is again convenient to treat it as a mechanical system with canonical coordinates (q_i, p_i). As already pointed out, the three eigenmotions of the system are decoupled and Liouville's theorem states that their action areas are conserved

$$I = \oint p_i \mathrm{d}q_i = \oint \boldsymbol{p}_\varphi \mathrm{d}\boldsymbol{l} = \mathrm{const} \tag{4.5}$$

where $\boldsymbol{p}_\varphi$ is the transversal momentum and $d\boldsymbol{l}$ the line element along the cyclotron orbit. The integral from Eq.(4.5) can be taken by considering that $\boldsymbol{p}_\varphi = m\boldsymbol{v}_\varphi + q\boldsymbol{A}$ and using Stokes' theorem

$$I = \oint m\boldsymbol{v}_\varphi \mathrm{d}\boldsymbol{l} + \oint q\boldsymbol{A} \mathrm{d}\boldsymbol{l} = m v_\varphi r \oint \mathrm{d}\varphi - q\,\mathrm{rot}\boldsymbol{A} \int_S \mathrm{d}S = m\omega_c r^2 2\pi - qBr^2\pi \tag{4.6}$$

where r is the cyclotron radius, $\boldsymbol{A}$ the vector potential of the magnetic field B and ω_c the cyclotron frequency defined by Eq.(2.10). Replacing ω_c results in a more convenient form

$$I = r^2 Bq\pi = \mathrm{const.} \tag{4.7}$$

Thus, an ion beam flying through an axial magnetic field gradient will have a beam envelope that scales with the square root of the magnetic field strength. This magnetic lens effect can be used to compensate the increasing divergence due to ion deceleration in the SpecTrap drift tubes. As an example, Fig. 4.12 shows two SIMION simulations for a deceleration from 200 eV to 20 eV ion energy (voltage switch from +120 V to -60 V) without (top) and with a magnetic field (middle). The bottom figure shows beam transport results through the trap without switching of the drift tubes. The emittance blow-up in the top figure and the magnetic focusing in the middle are clearly visible.

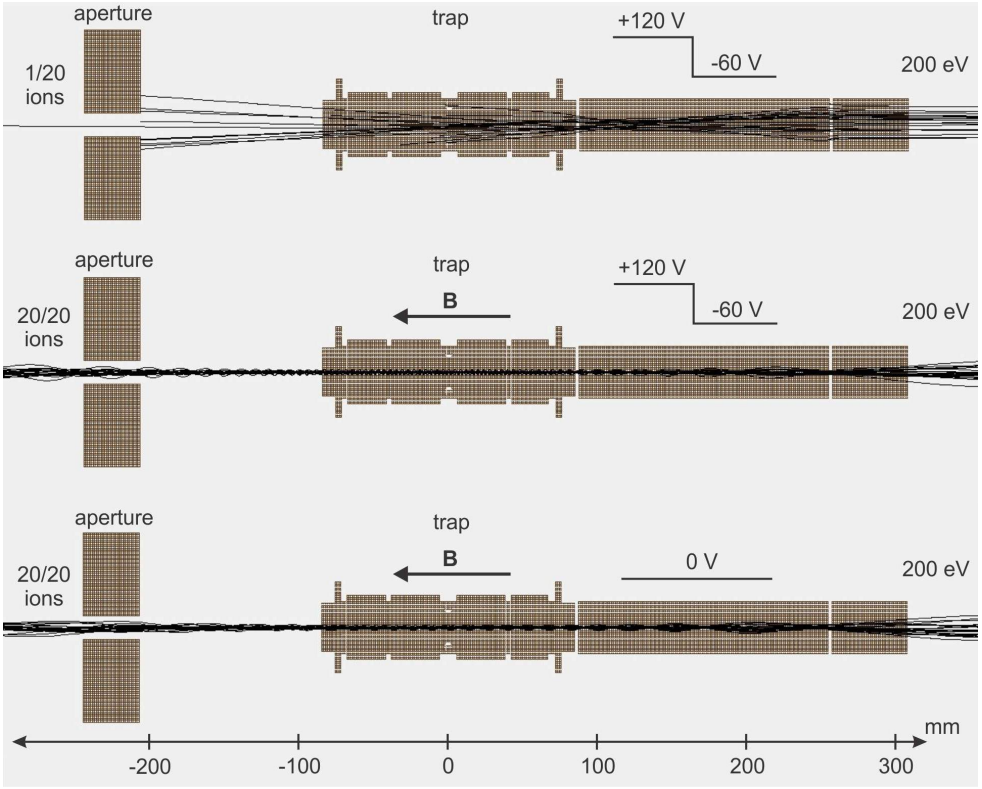

Figure 4.12: Three SIMION simulations of ion transportation through the region with the strongest magnetic field gradient in SpecTrap. The first is an illustration of emittance blow-up in drift-tube deceleration, without a magnetic field. The middle figure shows a pulsed drift-tube ion deceleration with 6 T magnetic field and the indicated parameters. The bottom figure shows ion transportation through a grounded drift tube without any deceleration. The last two figures clearly show the magnetic lens effect on ion propagation.

The amount by which an axial magnetic field can compensate for non-parallel beam propagation is limited by the so-called *magnetic mirror effect*. The reason lies in the non-zero radial component B_r of the magnetic field away from the central field axis. This field creates a force F_z which opposes ion motion as they move from the low field region to the high field region. The intensity of this force is given by

$$F_z = q v_\varphi B_r. \tag{4.8}$$

This force is always directed oppositely to the ion axial motion and can be quantified by taking Maxwell's equation for the magnetic field $\mathrm{div}\boldsymbol{B} = 0$ and extracting the radial component of the

field from the expansion in cylindrical coordinates (a detailed analysis can be found in [63]). An important consequence of Eq.(4.8) is that the magnetic mirror effect will scale with the incident angle between ion motion and the main axis. Several simulations of this effect were done for the SpecTrap beamline, and the results are shown in Fig. 4.13. They are plotted as total ion beam kinetic energy against the deviation angle of the incident ion beam from the main propagation axis. In this graph the area above each curve defines the beam acceptance; the area under each curve leads to magnetic reflection. It can be seen that the transversal energies that lead to reflection are smaller for ions with a larger mass-to-charge ratio. This can be explained by the fact that their cyclotron radius $r_c = mv_\varphi/qB$ is also larger, leading to a higher B_r component seen by such particles.

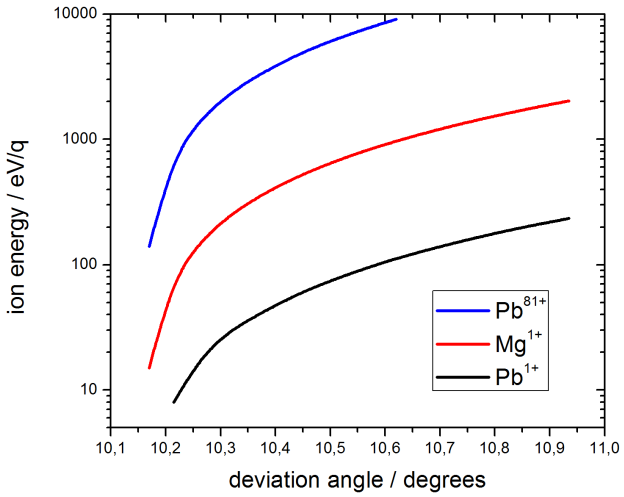

Figure 4.13: SIMION simulation results of the magnetic mirror effect in SpecTrap. The graph shows the minimum ion energy required to avoid the effect for a given incident angle (measured from the axis). Only ions located in the area above the curves can be transported into the trap; those with parameters below the curves are reflected.

In SpecTrap the distance between the last focusing point (E4 from Fig. 4.8) and the trap centre is 703 mm, and the beamline diameter inside the magnet is 21 mm. This means that the biggest possible beam divergence angle before ions strike the wall is around 0.9°, which is much smaller than the critical angle of around 10°, both for singly charged ions transported on $E > 100$ eV/q and highly charged ions on $E > 1$ keV/q. It can, however, be reached in case of unfavourable potential selection for pulsed drift tube deceleration and an optimum needs to be selected for different ion energies or m/q ratios.

The necessary condition for the analysis behind Eqs.(4.5)-(4.8) is the so-called adiabatic limit. In this model, the rate by which the magnetic field strength changes should be smaller (or ideally much smaller) than the relevant ion motion frequency. This condition is given as

$$\frac{1}{B_z}\left(\frac{\mathrm{d}B_z}{\mathrm{d}t}\right)_{r=0} < \frac{\omega_c}{2\pi} \tag{4.9}$$

which can be rewritten as

$$2\pi\sqrt{\frac{2mE}{q^2}}\frac{1}{B_z^2}\left(\frac{\mathrm{d}B_z}{\mathrm{d}z}\right)_{r=0} < 1 \tag{4.10}$$

where E is the ion energy and the magnetic field gradient can again be calculated from Eq.(4.1). The results for the SpecTrap magnet are plotted in Fig. 4.14. It can be seen that the full extent

of both drift tubes is inside the adiabatic limit. However, the left hand side of Eq.(4.10) becomes significantly smaller than one only very close to the trap centre. This can also be seen in the simulations shown in Fig. 4.12, where the beam envelope gets strongly compressed only around 260 mm from $z = 0$. It also suggests that the drift tube ion deceleration is more efficient with the second tube, which is located in a stronger magnetic field.

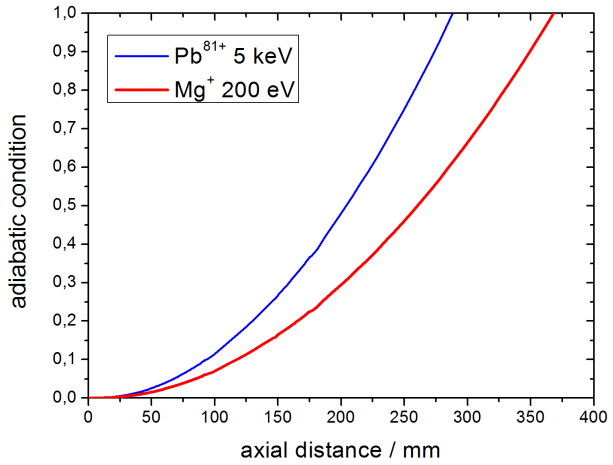

Figure 4.14: Adiabatic condition for the magnetic field change rate in comparison to the cyclotron motion in the SpecTrap beamline close to the magnet. The axial distance is normalized to the trap centre. Two typical cases are shown - locally produced singly charged Mg ions with 200 eV transport energy, needed for laser cooling, as well as highly charged Pb with 5 keV, planned after connecting to the HITRAP facility.

4.3.4. Experimental control system

The control of the complete ion transport system described in this section is done remotely via a personal computer. All voltages applied to the ion source and the ion optical elements are controlled by a data acquisition software based on LabVIEW. Additionally, the user has the option to use the program to remotely control two DG535 digital delay generators and three DS345 synthesized function generators. They are used to provide the trap electrode triggers, the frequencies for the system clock, ion excitation and laser scan. Also included into the control software are the voltage controls for the trap electrodes, supplied as a custom order from Stahl Electronics, and a control program for a SR430 multichannel scaler, used for time-of-flight measurements. An overview is shown in Fig. 4.15.

4.4. Lasers and photon detectors

As a laser spectroscopy experiment, SpecTrap also requires different laser systems and fluorescence detectors, whose design and operation principle is strongly dependent on the wavelength of interest. Detailed descriptions of some individual components are provided in the corresponding articles [64, 65, 66]. Here only a brief overview is given, emphasizing the experimental equipment currently installed at SpecTrap and used for the first measurements described in this work.

Laser systems for this experiment require a well controlled and safe environment for their operation. A laser laboratory was constructed under the SpecTrap magnet platform for that purpose. An schematic overview of the ion beamline - superconducting magnet - laser laboratory arrangement is shown in Fig. 4.16. Laser light is guided through the laboratory ceiling axially into

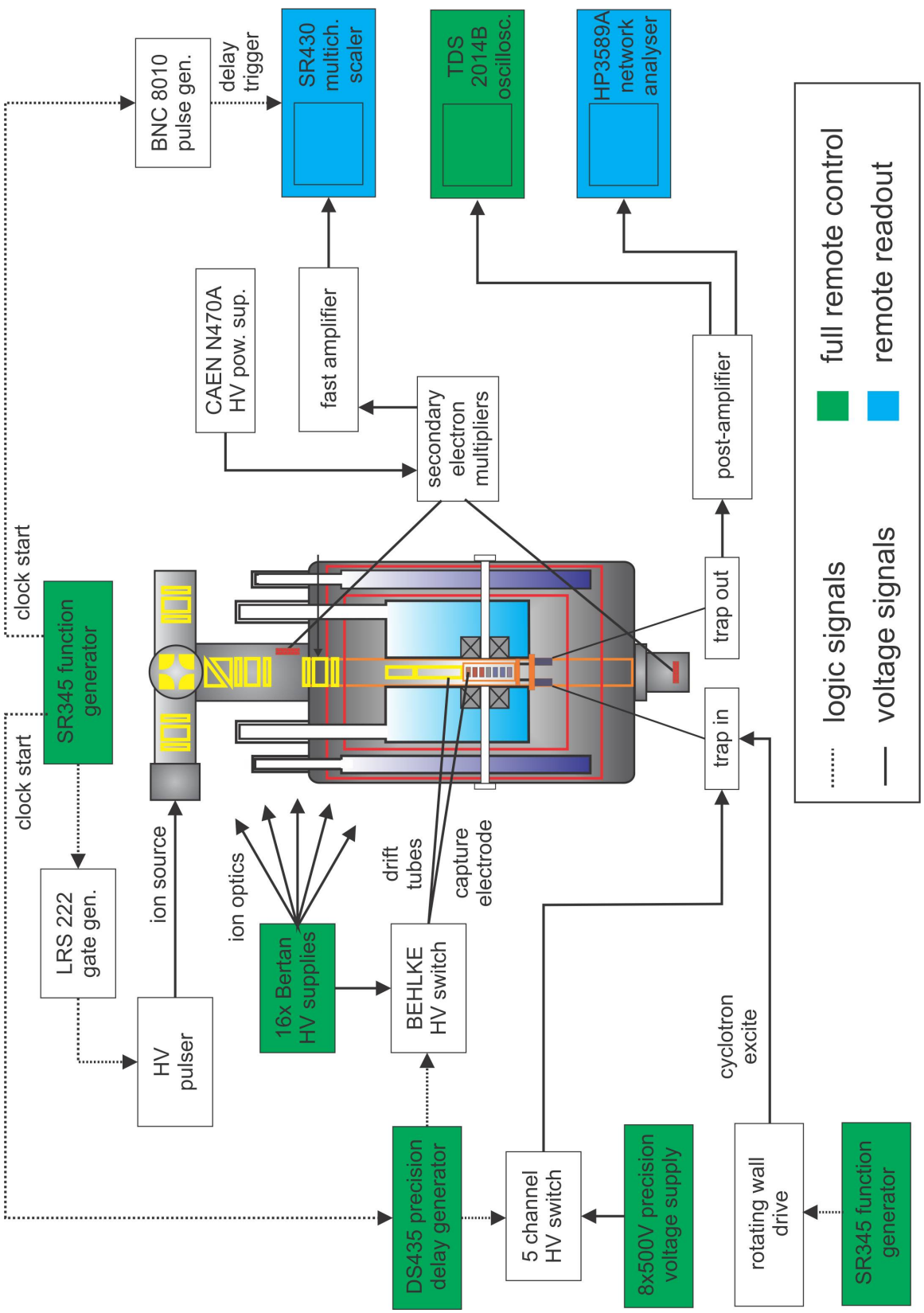

Figure 4.15: Overview of the experimental control and data acquisition system in SpecTrap.

the magnet and the trap where it can interact with the stored ions, and the induced fluorescence can be observed radially. The laser laboratory itself is shielded from external acoustic noise (−20 dB), temperature stabilized (±0.3 °) and has room for three laser tables (approximate size 0.8 × 1.5 m) with the corresponding electronics.

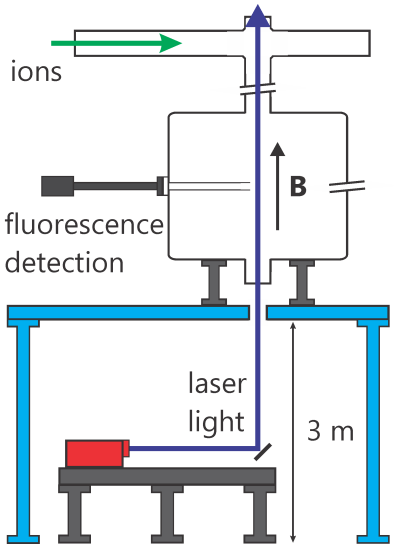

Figure 4.16: A schematic overview of the full SpecTrap experimental setup, including the ion beamline, the superconducting magnet and the laser laboratory (not true to scale). The platform (in light blue) is constructed out of steel, while the enclosed laser laboratory beneath it is shielded from external acoustic noise and temperature stabilized.

4.4.1. The cooling laser

Laser cooling of Mg^+ is performed on the $^2S_{1/2} - {}^2P_{3/2}$ transition at 279.6 nm (typically the the most abundant isotope ^{24}Mg is used). This is a rather inconvenient laser wavelength, which can hardly be generated directly. Instead, its production usually involves second-harmonic generation (SHG) schemes [67]. In SpecTrap, the fundamental laser source chosen for this purpose is a Koheras Boostik fibre laser, which produces up to 0.6 W of single mode radiation at 1118 nm. The fourth harmonic of this radiation provides the needed 279.6 nm. Hence, SHG steps are required and Fig. 4.17 shows the corresponding laser setup, including two frequency doubling stages. It was constructed at Mainz University, transported and installed at GSI in 2010, after the completion of the laser laboratory. It is described in [64, 68].

The 1118 nm laser light is first guided through two wave plates and a Faraday isolator in order to avoid any backscattered light disturbing the laser oscillator. The first frequency doubling stage involves a lithium triborate (LBO) crystal with non-critical phase matching. The SHG cavity is locked to the fibre-laser frequency using the Hänsch-Couillaud locking scheme and an efficiency of some 31% relative to the power coupled into the cavity was observed. Thanks to the non-critical phase matching, the output is a round Gaussian beam with an excellent beam profile, easy to mode-match and couple into the second doubler.

The second SHG-stage is constructed using a β-barium borate (BBO) crystal with critical phase matching. The cavity is also locked using the Hänsch-Couillaud locking technique, and the efficiency is around 10%. Due to the critical phase matching, the output is in this case non-Gaussian and elliptic and requires reshaping with two cylindrical lenses (depending on the application and not shown in Fig. 4.17). Using both doubling stages it was possible to make

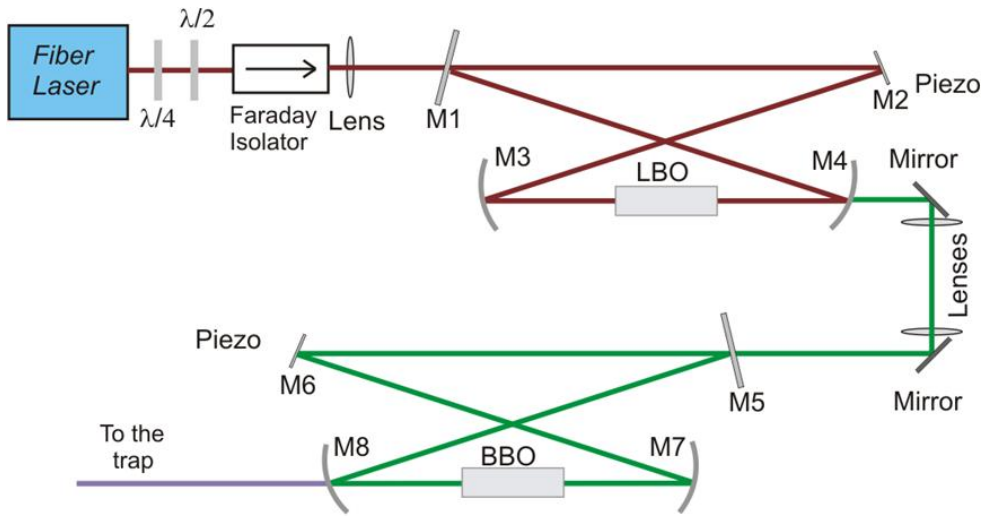

Figure 4.17: A schematic overview of the experimental setup for generation of 280 nm laser light needed for laser Doppler cooling of Mg^+. LBO and BBO are the non-linear crystals, Mx are the mirrors of the enhancement cavities and λ/x the quarter and half-wave plates. Details can be found in [68].

up to 5 mW of single mode 279.6 nm laser radiation available for the experiment. During the experiment, however, the power was typically kept on a much lower level (around 1 mW) because of higher laser stability and lifetime.

4.4.2. Fluorescence detection

Depending on the desired wavelength sensitivity, there are several photon detectors foreseen to be used at SpecTrap, each of them with a different set of properties and sizes. A list of these characteristics for the main three types is given in Tab. 4.2.

Table 4.2: Characteristics of the main three detector types foreseen to be used in SpecTrap (PMT stands for photo-multiplier tube, APD for avalanche photo diode and NIR for near infra-red).

wavelength range	200-400 nm	400-1050 nm	950-1700 nm
type	Channel PMT	APD	NIR-PMT
model	C1993P	RMD S0223	H10330-75
active area	$\varnothing = 15$ mm	$\varnothing = 2$ mm	$\varnothing = 1.6$ mm
quantum efficiency	18%	20-75%	18%
dark count rate	20 Hz	10-1000 Hz	100 kHz

A general trend can be clearly seen - photons with lower energies (i.e. longer wavelengths) become increasingly more difficult to detect. This, together with the fluorescence rate of a transition of interest, has to be taken into account when estimating the feasibility of a desired laser spectroscopic measurement. A simple estimation of the lower limit of the necessary measurement time, based on a saturated transition, is provided by the following argumentation: in order to be detected, a fluorescence signal S needs to be comparable or bigger than the noise of the detector. If the fluorescence rate is given by $s = An$, where A is the transition rate (i.e. the Einstein A

coefficient, inversely proportional to the excited level lifetime) and n the number of stored ions, the measurement time t for reaching a satisfactory signal-to-noise ratio is given by

$$S = s \cdot t \cdot \epsilon \geq n_\sigma \sqrt{d \cdot t} \qquad \Rightarrow \qquad t \geq \left(\frac{n_\sigma}{s \cdot \epsilon}\right)^2 d \tag{4.11}$$

where ϵ is the detection efficiency, n_σ the confidence level in units of a standard deviation and d the dark count rate. Under the assumption that the detection efficiency is a product of the quantum efficiency (18-75% from table 4.2) and the fluorescence collection efficiency ($\approx 10^{-5}$ out the full solid angle), the number of trapped particles is $n = 10^5$ and that the transition intensity is 100 s^{-1}, Eq.(4.11) gives $t = 0.6$ s for APDs and $t = 2250$ s for NIR-PMTs at a 3σ confidence level. However, due to laser fluctuations, stray light and other non-statistical contributions to the noise, these measurement times will be even larger and strongly depend on the specific experimental setup. They need to be compared to the trapping time, in the sense that the detection can take place only during the time particles are available for excitation and fluorescence detection. If an increase in the number of trapped particles or the trapping time is not possible, the signal-to-noise ratio can be improved by employing separated pulsed excitation/detection cycles.

The detector used for monitoring the fluorescence of laser-cooled Mg ions in SpecTrap is a channel photo-multiplier (CPM), with the characteristics from Tab. 4.2. Because of the fast cooling transition and low dark count rate the necessary measurement time was not an issue. However, this type of detector is highly sensitive to the stray magnetic field of the SpecTrap superconducting magnet and required an extended mounting point, as well as additional magnetic shielding.

Chapter 5

Commissioning of the ion beamline and the Penning trap

5.1. Ion transport and deceleration

The assembly and commissioning of the SpecTrap ion production and transport system began in 2009, with the first investigations of the beam quality, alignment and deceleration, and the results were presented in the diploma thesis of B. Sommer [69]. The system saw further upgrades since that time, namely the introduction of the Mg ion source and additional ion optical and beam bending elements. This section presents the latest results and discussion of ion production and manipulation in the SpecTrap beamline, as an important step towards laser cooling of Mg^+, as well as for the future connection to the HITRAP beamline and access to highly charged ions.

5.1.1. Time of flight spectrometry

The SpecTrap ion beamline, described in section 4.3, consists only of electrostatic elements, while the static magnetic field close to the superconducting magnet coils acts on the ions solely through its magnetic lens effect, described in section 4.3.3. A well-known method for a momentum analysis of an ion beam transported under such conditions called *time of flight (TOF) spectrometry* is used in SpecTrap. Alternative beam analysis methods capable of separating different ion momenta require combined electro-magnetic elements, such as a Wien filter or a magnetic bender, and are beyond the scope of this work.

The general equation of motion of a particle propagating in an electrostatic field is given by

$$m\frac{\mathrm{d}^2\mathbf{r}}{\mathrm{d}t^2} = q\mathbf{E} \tag{5.1}$$

where $\mathbf{E}$ is the electric field, for instance inside an einzel lens or electrostatic bender. Since m/q is a constant of motion for a given ion, it can be normalized to unity without changing the kinematics of the system, which makes Eq.(5.1) take the following form

$$\left|\frac{\mathrm{d}^2\mathbf{r}}{\mathrm{d}t^2}\right|_{\frac{m}{q}=1} = \mathbf{E}. \tag{5.2}$$

Obviously the solution $\mathbf{r}(t)$ of Eq.(5.1) depends explicitly neither on ion mass nor its charge. That means that all particles with velocities proportional to m/q, i.e. particles extracted with the same potential, will follow exactly the same trajectories in space.

Low-energy beams are usually produced by accelerating the ions by a static potential difference. That is also the case in SpecTrap, where this potential is defined by the cup-shaped grid, shown in Fig. 4.9. Thus, all ions have the same potential energy U upon creation, i.e. the kinetic energy K after acceleration by the voltage V

$$U = qV = K = \frac{1}{2}mv^2 \tag{5.3}$$

except for the thermal energy distribution inside the source, which is typically small compared to V. This energy is then conserved along an electrostatic beamline. If the distance to the detector is given with l, the time of flight can be expressed as

$$t = l\sqrt{\frac{m}{2K}} = l\sqrt{\frac{m}{2qV}}. \tag{5.4}$$

For a given acceleration potential, ions with different m/q ratios will all have different times of flight, which can be used for identification and separation of ion species. Two such time-of-flight spectra are presented in Fig. 5.1. The graph on the left shows a typical spectrum of the magnesium ion source described in section 4.3.1, and the graph on the right shows the spectrum of the Ar-ion source. The pulse length was set to 1 μs, which is of the order of the trap acceptance for the given energy and mass-to-charge ratio as defined by Eq.(3.9).

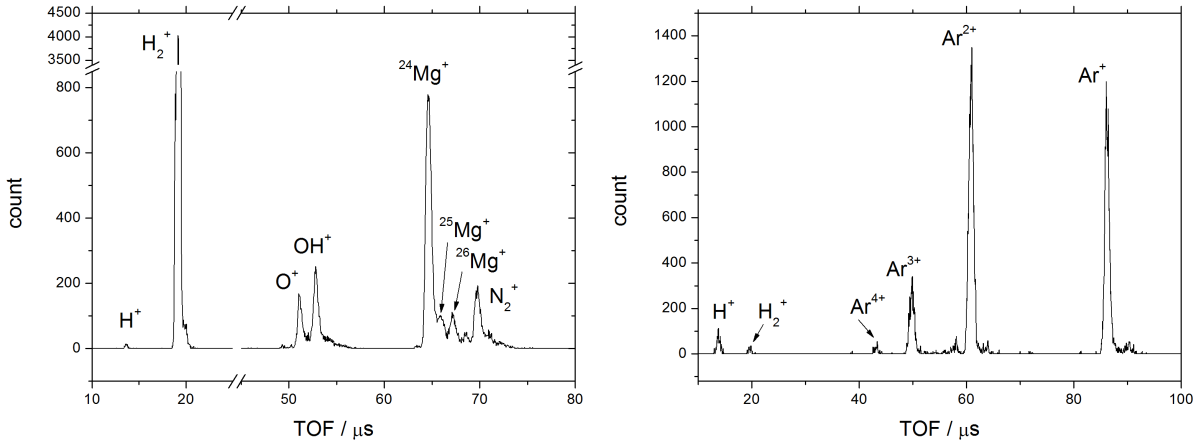

Figure 5.1: Time of flight mass spectrum of the beam produced with the magnesium (left) and argon (right) ion source in SpecTrap, summed over 1000 shots with a multi-channel scaler. Data was taken with a micro channel plate, located on the bottom of the magnet, some 3.5 m away from the source. Mg atoms are evaporated in an oven, while Ar is introduced as a gas, before they are both ionized in the second stage and extracted with an energy of 400 eV/charge.

This two source types give access to different ion species: while the Mg source can be used with all elements that can be evaporated by a crucible, particularly all non-refractory metals, the Ar source can be operated with any inert gas and can produce also charge states higher than

one. Figure 5.1 shows that the typical isotope ratio of naturally occurring Mg (79% ^{24}Mg, 10% ^{25}Mg and 11% ^{26}Mg) is well reproduced in the TOF spectrum, followed by several contaminants also evaporated by the oven or ionized from the residual gas. In the case of Ar the amount of contaminants is smaller and charge states up to Ar^{4+} were produced. It can also be seen that the bunch size is well preserved throughout the beamline, amounting up to 1.1 μs upon impacting the micro channel plate. The overall number of ions with a desired mass and charge state detected in a single shot can be derived by integrating the data from Fig. 5.1, and it amounts to 15 in the case of Mg and 32 in the case of Ar. By increasing the oven temperature or background gas pressure, for Mg and Ar respectively, the yield can typically be made several times higher, but for the price of a higher pressure in the beamline and Mg deposition on the chamber walls (coating). However, even after taking this boost and the expected detection efficiency of some 10-30% into account, the overall number of produced ions is relatively small and indicates that accumulation of several ion source shots in the trap, as discussed in section 3.3.2, is required.

Resolution of a mass spectrometer is usually defined as the ability to distinguish ions with close mass-to-charge ratios and is given by

$$R = \frac{\tilde{m}/\tilde{q}}{\Delta(\tilde{m}/\tilde{q})}, \tag{5.5}$$

where $\tilde{m}$ and $\tilde{q}$ are mass and charge numbers, respectively. The resolution the SpecTrap time-of-flight "mass spectrometer" is dictated primarily by the ion bunch size, i.e. for a given ion flight length and energy two different mass-to-charge ratios can be distinguished only if their respective times of flight are separated by a value equal or bigger than the bunch temporal width. Equation (5.4) can be used to calculate this separation

$$\Delta t = t_2 - t_1 = l\sqrt{\frac{m_u}{2eV}}\left[\sqrt{\tilde{m}/\tilde{q} + \Delta(\tilde{m}/\tilde{q})} - \sqrt{\tilde{m}/\tilde{q}}\right] \tag{5.6}$$

where m_u is the atomic mass unit. By taking into account the 3.5 m distance between the ion source and detector in the SpecTrap beamline, Eq.(5.6) can be used to estimate the maximum mass-to-charge ratio $\tilde{m}/\tilde{q}$ which can be resolved for a given ion energy per charge and desired resolving power $\Delta(\tilde{m}/\tilde{q})$

$$\tilde{m}/\tilde{q} = \left(\frac{M^2 - \Delta(\tilde{m}/\tilde{q})}{2M}\right)^2, \qquad M = \frac{\Delta t}{l}\sqrt{\frac{2eV}{m_u}}. \tag{5.7}$$

Figure 5.2 gives an overview of the maximum resolution of the SpecTrap mass spectrometer, under the assumption that $\Delta t = 1$ μs. For example, at beam energy of 100 eV two neighbouring masses of singly charged ions can be resolved up to mass 150, whereas it is possible only up to mass 50 at 300 eV beam energy.

5.1.2. Pulsed drift tube deceleration

As described in section 4.3.3, there are two drift tubes in SpecTrap, located next to each other inside the superconducting magnet bore in front of the trap. Depending on the requirements, experimental conditions and desired efficiency, they can be used

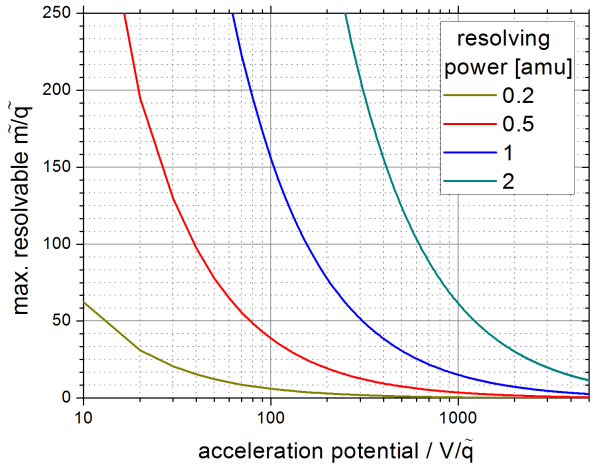

Figure 5.2: Resolution of the SpecTrap beamline time-of-flight mass spectrometer. The graph shows the maximum resolvable mass-to-charge ratio for a given resolving power. The assumed temporal bunch size is 1 μs, and the distance between the ion source and detector is 3.5 m.

- individually,
- in parallel, where each one takes away a part of the ion energy, or
- together, offering a bigger effective length, suitable for longer ion bunches.

In the presence of the magnetic field, as it is the case in SpecTrap, it is adventageous to use a drift tube which is located within the adiabatic limit, as discussed in section 4.3.3 and shown in Fig. 4.14. Therefore, only the second drift tube was used for ion deceleration in SpecTrap, with the first one as an option for accepting very long ion bunches.

Since magnesium ions for laser cooling were typically produced with 200 eV transport energy in 1 μs pulses, they were well within the trap acceptance defined by Eq.(3.9), and no deceleration was necessary. Although higher energies were accessible, it was not possible to perform a detailed analysis of drift tube deceleration in the presence of the magnetic field due to the limited magnet operation time (limited by the consumption of liquid helium). However, they were tested without a magnetic field, and the results are shown in Fig. 5.3.

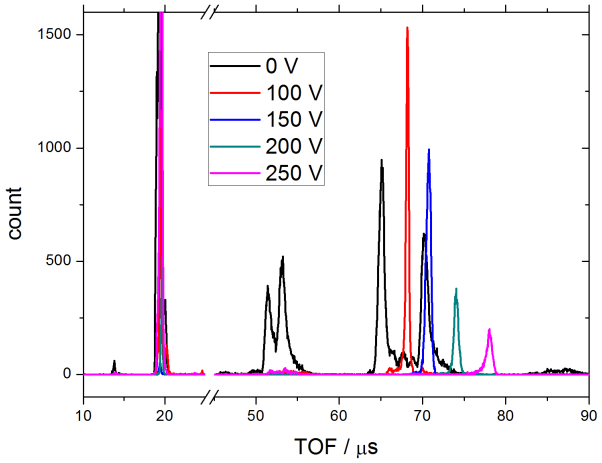

Figure 5.3: Time-of-flight spectrum of Mg^+, produced with an energy of 400 eV and decelerated by the SpecTrap drift tubes, with different deceleration voltages. Non-decelerated ions are shown in black, and have a spectrum similar to that in Fig. 5.1.

It can be seen that ions decelerated by moderate voltages are transported very efficiently. An integral of the measured curves yields an efficiency of 83% and 87% for 100 and 150 eV deceleration

energy, respectively. Although not expected, a slight increase for a larger deceleration energy can be explained by a more favourable lensing effect in that case, which resulted in more transported ions. The efficiency extracted in the same way for 200 and 250 eV deceleration energy amounts to 32% and 22%, respectively. The expected smaller temporal distribution of decelerated ions can be easily observed in the first two peaks, but becomes less pronounced for the other two. Both smaller efficiencies and temporal distributions can be attributed to the emittance blow-up and poor beam parameters.

The results show that the drift tubes operate as expected, but also that for a deceleration of more than 50% of the initial energy additional optimization is necessary. As highly charged ions from HITRAP are expected to have several keV transport energy, it will be neccessary either to perform drift tube ion deceleration inside the magnetic field, or employ a two stage deceleration, or combine both of them. Installation of an additional, external drift tube assembly is also possible, which would have the disadvantage of being completely outside the magnetic field, but also offer the possibility to install einzel lenses before and after the tubes, which could significantly improve their operation.

5.2. Ion trap system

The design of the electronic components for non-destructive ion detection at SpecTrap began in collaboration with Stahl Electronics in 2008, directly after the first tests of the trap operated in the RF mode [70]. The trap design was slightly changed since then, in order to accommodate the electrical and spatial requirements presented with the operation as a Penning trap and the superconducting magnet. The final trap design was presented in chapter 3, and this section reviews the results of the cryogenic electronic circuits attached to the trap, as well as the first commissioning results, which pointed towards some problems which were not expected, but successfully solved once they were identified.

5.2.1. Resonant circuits and cryogenic amplifiers

SpecTrap employs three different cryogenic circuit groups, each of them with different design aims:

1. Two axial amplifiers, including the resonant circuits, designed for two different axial ion oscillation frequencies. Their purpose is to pick up the trapped particle signal, as well as to cool the ion axial motion. Hence, the quality factor of the RLC circuits had to be optimized for broad-band frequency acceptance and efficient cooling simultaneously.

2. Two cyclotron amplifiers, without resonant circuits, with the same design (serving as backup for each other). Since laser excitation takes place axially, cooling of radial ion motion is not necessary, and their purpose is solely to measure the cyclotron ion frequency.

3. One arrival detector (amplifier), also without a resonant circuit, attached to the capture electrode. Its purpose is to pick-up shot noise from incoming ions, creating thus a trigger for closing the trap.

All three circuit groups were tested prior to implementation and the results of those investigations are presented in this section.

Axial amplifiers At low frequencies the noise on the axial amplifiers is dominated by the so-called pink noise which has approximately a $1/f$ spectrum. At higher frequencies the thermal (Johnson) noise becomes dominant, and it is given for a resistance R at a temperature T by [47]

$$V_{\text{Johnson}} = \sqrt{4k_B T R \delta} \tag{5.8}$$

where δ is the measurement bandwidth (a brief discussion of different noise sources is presented in appendix B). The $1/f$ noise is clearly visible in Fig. 5.4, which shows the room temperature noise level on both axial resonant circuits, recorded by broadband frequency sweeps. At around 420 kHz an external noise source appears[1], followed by the amplified axial noise at the resonant frequencies of 525 kHz (left) and 1.08 MHz (right).

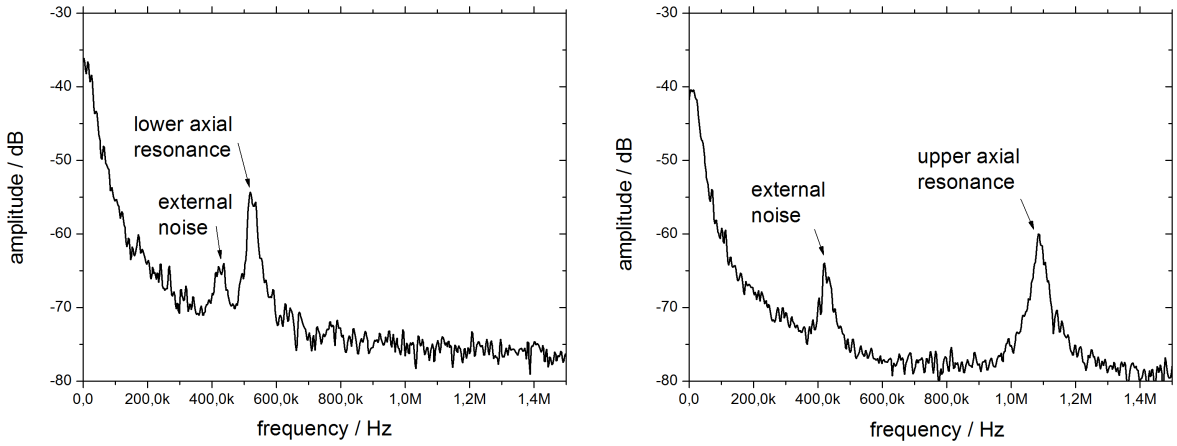

Figure 5.4: Swept frequency spectrum of the lower (left) and upper (right) resonant circuit and amplifier in SpecTrap at 300 K. The two resonances can be clearly observed, as well as an external noise source at 420 kHz.

As discussed in section 2.3.1, the quality factor of a resonant circuit is defined as the ratio of the resonant frequency and the full width on -3 dB with respect to the resonance peak. As the noise level depends not only on temperature T, but also on the measurement bandwidth δ, the fast Fourier transform measurement mode of the spectrum analyser gives much better results. Fig. 5.5 shows such a narrow-band-zoom spectrum of the two axial resonant circuits, at room temperature and liquid helium temperature.

The noise spectrum of a resonant circuit can be modelled analogous to the Johnson noise of a resistor if the ohmic resistance R is replaced by the impedance of the RLC circuit. The latter is given by the real part of the complex RLC impedance, defined by Eq.(2.40). The expected

[1] This noise peak was always present on all frequency sweeps across that range, and its source has so far not been identified. It was ignored since it did not coincide with any of the resonant frequencies.

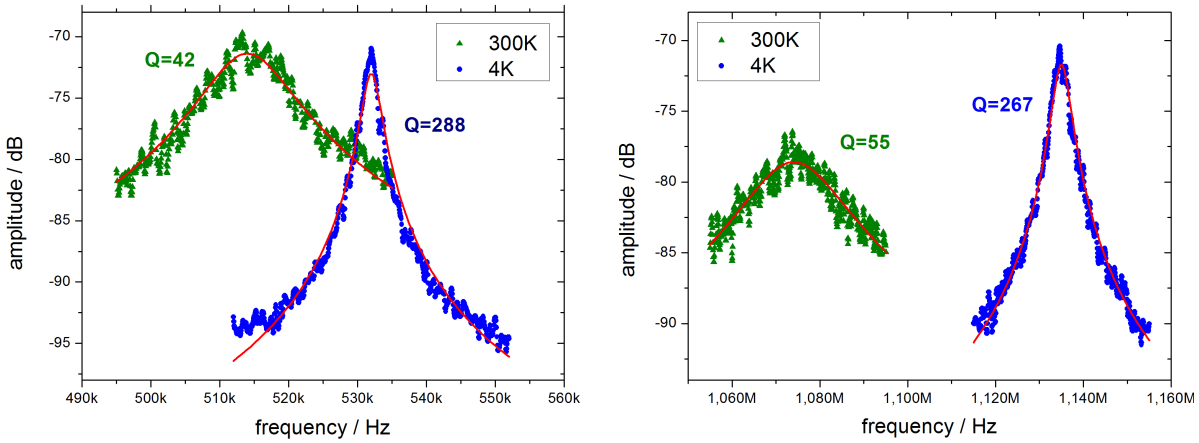

Figure 5.5: Narrow-band zoom frequency spectrum of the lower (left) and upper (right) resonant circuit and amplifier in SpecTrap at 300 K and 4 K. The data was fitted with the function from Eq.(5.10).

voltage on the free-running SpecTrap axial amplifiers takes in that case the following form

$$V_s = \sqrt{4k_B T\delta \frac{R}{1+\frac{Q^2}{W^2}\left(W^2-1\right)^2}}; \qquad W = \frac{\omega^2}{\omega_{LC}^2}. \tag{5.9}$$

This equation describes the voltage noise level of a resonant circuit, while the signal-to-noise ratio amplitude expressed in dB can be calculated according to

$$A = 10 \cdot \log\left(\frac{V_s^2}{V_n^2}\right) = 10 \cdot \log\left[\frac{4k_B T\delta}{V_n} \cdot \frac{R}{1+\frac{Q^2}{W^2}\left(W^2-1\right)^2}\right]. \tag{5.10}$$

This function has been used for fitting the data shown in Fig. 5.5 and the model describes the measured spectra very well. The quality factor is obtained as one of the fit parameters. Different values of the quality factor and the resonant frequency at different temperatures are caused by the reduction of ohmic resistance at lower temperatures, while the background noise level drops with temperature according to Eq.(5.8).

Cyclotron amplifiers Since no resonant circuits are present in the amplifiers designed for the signal induced by the ion cyclotron motion, the noise spectrum depends only on the $1/f$ and Johnson noise. Figure 5.6 shows swept noise spectra of both SpecTrap cyclotron amplifiers. Several noise sources are present in the lower frequency range, together with the 420 kHz external noise signal, which was also present for the axial amplifiers. Since the typical ion cyclotron frequency for mass-to-charge ratios planned for SpecTrap experiments is of the order of a MHz or more, this low-frequency noise does not present a problem and can be ignored.

Arrival detector The same basic analysis as for the cyclotron amplifiers applies also to the arrival detector, and the spectrum plotted in Fig. 5.7 is again dominated by the $1/f$ noise. The amplitude of the 420 kHz external noise is larger in comparison to the cyclotron amplifier because of the larger transconductance (i.e. larger amplification factor) of the transistor in use, which also

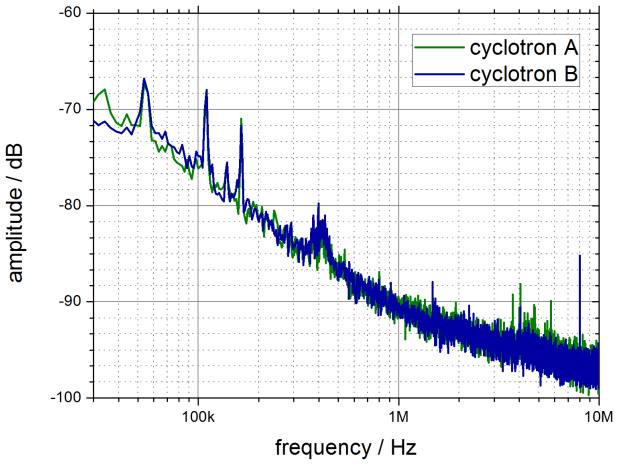

Figure 5.6: Swept frequency spectrum of the two cyclotron amplifiers in SpecTrap, measured at room temperature for the relevant frequency span. No resonance circuits are present and the noise density follows roughly the $1/f$ spectrum. Some low-frequency noise sources can be identified, as well as the 420 kHz external noise signal, present on the axial amplifiers as well.

has a larger characteristic $1/f$ noise, resulting in a larger overall noise level. Since the arrival detector was designed to pick up the signal of incoming ions, it was attached to the capture electrode, which is the first electrode that the incoming ions encounter. However, in order to capture the incoming ion cloud, this electrode needs to be quickly pulsed to a high voltage, as discussed in section 3.3.1. Hence, the arrival detector was tested before and after a 1 kV pulsing test, and the results are also presented in Fig. 5.7. No significant change in the noise spectrum is present, and the detector can be used simultaneously with the standard ion capture cycle.

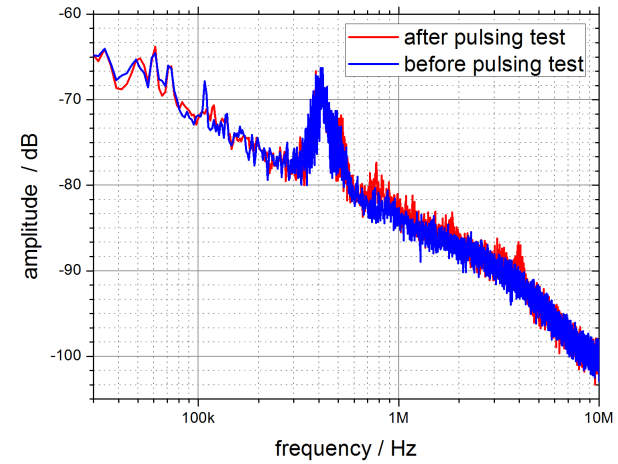

Figure 5.7: Swept frequency spectrum of the arrival detector in SpecTrap, measured at room temperature for the relevant frequency span. The noise level is determined by the same mechanism as in the cyclotron amplifier. The amplifier-detector was tested with high voltage pulses on the capture electrode, and the graph shows the spectrum before and after that test.

5.2.2. Surface charge and electron emission

During the commissioning of the ion trap inside the SpecTrap magnet several effects that disturbed stable operation of the system were observed. Eliminating them was of crucial importance for ion trapping in SpecTrap, and this section gives a description of the encountered problems, as well as the employed solutions.

Surface charge As described in section 4.1, the SpecTrap superconducting magnet has a cold bore, with no direct separation between the bore and the insulation vacuum. This feature is favourable for trap mounting, in terms that the magnet cryostat is used also for cooling the trap electrodes and the electronic components. Moreover, cryopumping improves the pressure inside the bore considerably compared to the remaining part of the system. This, however, also means that the background gas material is deposited on the cryostat surfaces, including the trap and the ion optical components located inside the cold bore. In SpecTrap, as discussed in section 4.2, the standard background pressure is of the order of 10^{-8} to 10^{-9} mbar, which should prevent the formation of a significant layer of frozen gas on the cold surfaces. However, the operation of the Ar-ion source required the introduction of Ar gas into the system, which increased the background pressure by two to three orders of magnitude. That was probably sufficient to form a micro-layer of frozen argon on the cold surfaces, which then led to inhomogeneous charging-up effects, significantly altering the ion flight path. Since this effect is essentially random, the result was a much lower and fluctuating ion transport efficiency. The only way of removing the frozen micro-layer is warming up the complete system to room temperature, and it was concluded that the Ar source must not be operated with the cryogenic system before an efficient differential pumping system is installed. In that way the background vacuum pressure was kept below 10^{-7} mbar, which presented no problem during the further operation of the system.

Electron emission Solving the problem with frozen gases and charging effects in the ion beamline enabled stable ion transport at cryogenic temperatures as well as at room temperature, and TOF spectra like that shown in Fig. 5.1 could be routinely reproduced. However, even with all ion sources switched off, it was observed that under certain conditions the MCP detector below the Penning trap recorded a continuous signal of arriving ions. It was strongly dependent on the voltages applied to some of the trap electrodes, starting with around 1 kcps for 200 V, increasing with the voltage and levelling around 10 kcps for 300 V. After reaching the 200 V threshold, this process became self-sustaining and had to be stopped by tuning all trap potentials to zero, because any further ion transport or trapping was not possible. It is assumed that the ions were created inside the trap by electrons emitted from unwanted micro field-emission points and forced into cyclotron orbits through the trap by the strong magnetic field. A series of tests was performed in order to check this assumption. Fig. 5.8 shows on the left a signal recorded on the lower axial resonant circuit during the emission process - several induced signals can be seen next to the main resonance peak, with the overall noise level higher by some 30 dB in comparison to Fig. 5.4. Although this made the identification of the observed signals very difficult, it was possible to isolate the ones coming from Ar^+ and Ar^{2+} by comparing three spectra, two with different additional background pressures of Ar introduced through the gas inlet and one with the valve closed. Figure 5.8 shows on the right a kind of autocorrelation function of the spectra, obtained by the following equation

$$S = (S_1 - S_0) \cdot (S_2 - S_0) \tag{5.11}$$

with S_0 being the spectrum recorded with the valve closed and therefore low background pressure, and $S_{1/2}$ the spectra recorded with one and two orders of magnitude higher pressure, respectively.

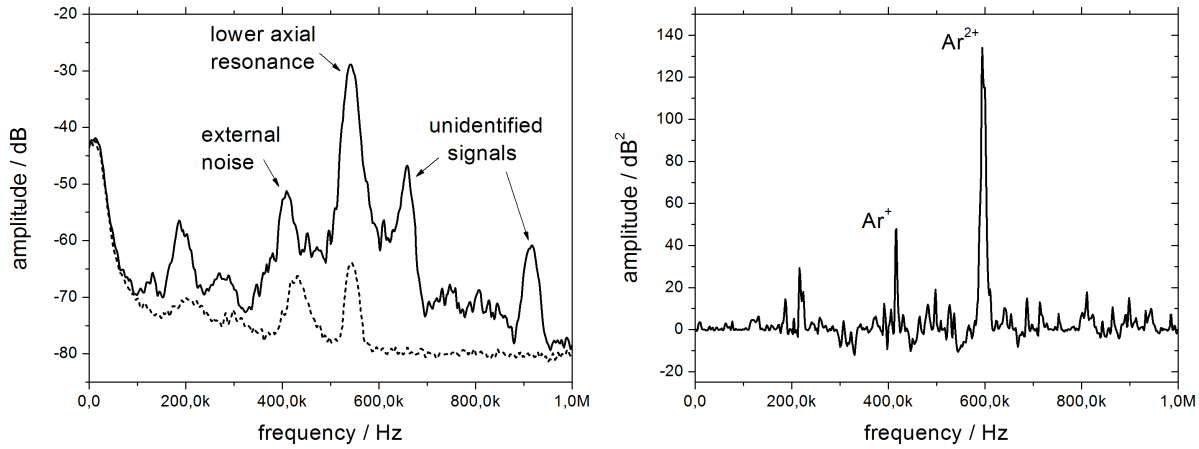

Figure 5.8: Left: lower axial resonance surrounded by unidentified noise sources, after triggering the electron emission and ion creation inside the trap. The dotted line shows the signal with the grounded trap electrodes. Right: autocorrelation of two such spectra according to Eq.(5.11), after triggering the electron emission in the trap and raising the background vacuum pressure with argon.

This analysis showed that ions were indeed created inside the trap from the background gas atoms. The fact that the process was triggered by increasing the voltage of the trap electrodes was a strong indicator that the reason for it were electrons emitted from micro-field emission points, which had to be removed. The ion trap was therefore dismantled and the inner side of all electrodes was mechanically polished to a mirror finish. Since this treatment removed the gold plating, it had to be refurbished, but this time the surface was coated with only a very thin layer in order to preserve the polished surface. After reassembling the trap and installing it into the magnet, the ion creation effect was significantly suppressed: the threshold was now reached only at much higher voltages of the order of 500-1000 V. This was tolerated since it did not pose a problem for further use of the system.

Chapter 6

First results of trapping and laser Doppler cooling of Mg ions

6.1. The measurement cycle

Ions produced by the ion sources described in section 4.3.1 were transported through the SpecTrap beamline and trapped in the Penning trap. This section gives an overview of the technique used for capturing and storing those ions, as well as an analysis of the achieved results.

In order to trap Mg ions and observe the effects of laser cooling, a measurement cycle was established, and it consisted typically of the following steps:

- initial ion trapping and stacking.
- compressing the trapped ion cloud towards the trap centre, laser Doppler cooling and fluorescence detection.
- exciting the ion motion and picking up the electronic signal from the ring electrode.
- opening the trap and dumping the ion cloud.

Each step is defined by a special set of trap electrode voltages, relative switching times and amplitudes, as depicted in Fig. 6.1. Initially, only the reflector electrode is permanently switched high (closed), while the capture electrode is switched between a confining potential and a value just below ion transport energy. The latter is repeatedly pulsed down for a period of Δt_2, with a rate of $1/\Delta t_1$. This technique, already discussed in section 3.3.2, allows new ions to enter the trap, but prevents the pre-cooled stored ions to escape and results in stacking many consecutive ion bunches in the trap. After the time dedicated to ion accumulation has elapsed, the capture electrode stays permanently closed and the voltage on the endcaps and correction electrodes is slowly ramped up. This process compresses the ion cloud towards the trap centre, where it can be efficiently irradiated with a laser beam. In this part of the cycle the strongest laser cooling takes place and laser induced fluorescence can be seen. It should be noted that the far-red detuned laser has already been present during the ion stacking process. By observing the fluorescence and changing the trapping parameters it was possible to trap between several thousands and a single

ion in SpecTrap, and the results are presented in section 6.3. In the next stage of the trapping cycle the ions can also be detected electronically by transmitting an AC voltage signal with a small amplitude on top of the DC ring electrode voltage, which excites the corresponding ion motion and increases the signal induced in the trap electrodes. This is the basis of the Fourier transform ion cyclotron resonance (FT-ICR) detection, and the results of implementing this technique in SpecTrap are presented in section 6.4. After finalizing the experimental steps, the voltages of all but the capture electrode are lowered, the remaining ions are ejected and the trap is prepared for the next cycle.

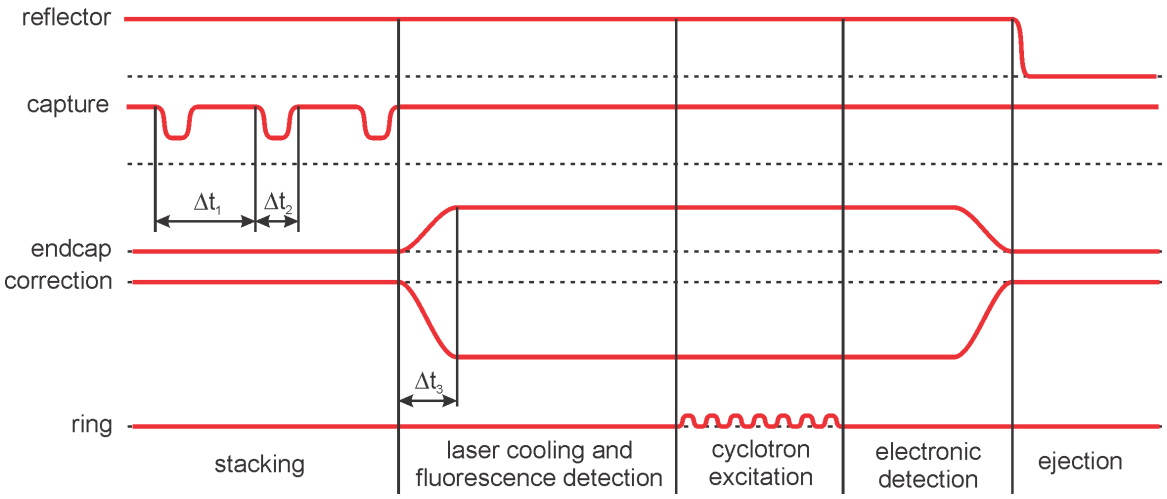

Figure 6.1: Overview of one trapping cycle in SpecTrap. Voltage amplitudes on individual electrodes are plotted against time. Neither the amplitudes, nor the time axis are true to scale. The dotted lines represent a reference level, typically ground. The intervals $\Delta t_1 = 0.33$ s, $\Delta t_2 = 2$ μs and $\Delta t_3 = 200$ μs are the stacking period, capture gate and endcap/correction electrode rise time. They were kept fixed, while all other parameters were adjusted as required. The period of stacking $t = n_i \cdot \Delta t_1$ was changed to vary the number of stored ions in the trap.

In order to properly interpret experimental results it is very important to establish reliable methods of detecting and counting the stored ions. They have already been treated by the previous chapters, and a summary of the ones implemented at SpecTrap is

1. Ejection and counting. The biggest advantage is that the standard secondary electron multipliers, as described in section 2.2, have very large detection efficiencies and the number of detected ions can be read out directly. However, in the case of Penning traps the ejected ions typically have to pass through a strong magnetic field gradient, which significantly influences their flight path, as discussed in section 4.3.3, and possibly results in a small overall number of ions that reach the detector. Another obvious disadvantage is that the method is destructive, and the trap has to be reloaded for further experiments.

2. FT-ICR. This method is non-destructive and offers the possibility to continuously monitor the evolution of the ion number and charge states inside the trap. A disadvantage is that a relatively large number of ions is required for inducing an electronic signal large enough to be detected; single-ion detection is possible only in special, dedicated high-Q systems [71].

Additionally, the results might be inconclusive, since the signal amplitude depends both on the number of ions and the ion temperature.

3. Laser induced fluorescence (LIF). In this case the observed signal is in principle directly proportional to the total number of stored ions, as long as the ion cloud does not become larger than the laser beam. If the resonant transition has a short excited level lifetime - as is the case for Mg^+ - even a single ion can produce a sufficient number of fluorescence photons to raise the signal above the noise floor. The main disadvantage is that a laser system and a fluorescence detector must be installed, which increases the complexity of the system. Moreover, only very few ion species offer the required two-level scheme, and possible dark states require even more laser systems to be operated simultaneously. This might prove difficult, especially in the initial stage of the experiment, and it is usually advantageous to use this method in combination with one of the others.

6.2. Lifetime determination

The number of stored ions inside a trap is not constant, but subject to a continuous drop, especially if large ion clouds are stored. The *ion lifetime* is defined as the average time in which the number of stored ions drops by a predefined factor, typically e (the base of natural logarithms). If the trapped ions are multiply charged, one can also define a *charge-state lifetime*, since these ions can capture one or more electrons, change their charge state, and still remain in the trap. There are different ion loss-mechanisms and the dominant ones are:

1. Charge exchange. A trapped ion captures an electron from a residual gas particle and changes its charge state

$$\mathrm{X}^{\mathrm{n}+} + \mathrm{R}^0 \rightarrow \mathrm{X}^{(\mathrm{n}-1)+} + \mathrm{R}^+.$$

   Obviously, if $n = 1$, the ion is neutralized and cannot remain trapped. However, if $n > 1$ the number of trapped ions can remain unchanged, or even be increased if the ionized residual gas particle is also trapped. Nevertheless, the number of ions in the desired charge state is decreased. If a large mixture of charge states is trapped and the state of interest $n+$ is not the highest one, also feeding of the state is possible. The process is directly proportional to the residual gas (vacuum) pressure inside the trap.

2. Elastic scattering. A trapped ion collides with a residual gas particle, changes its momentum and leaves the trap

$$\mathrm{X}^+(\mathbf{p}_1) + \mathrm{R}^0(\mathbf{p}_2) \rightarrow \mathrm{X}^+(\mathbf{p}_3) + \mathrm{R}^0(\mathbf{p}_4).$$

   It should be noted that this process does not necessarily lead to ion loss, since the scattered ion has to receive enough energy to be scattered into an unstable orbit. This process is also for a fixed temperature directly proportional to the vacuum pressure.

3. Intra-cloud scattering. This is basically the same process as the last one, but the energy exchange happens between two ions of the cloud out of which one leaves the trap, carrying

away a part of the total ion cloud energy[1]

$$X^+(\mathbf{p}_1) + X^+(\mathbf{p}_2) \rightarrow X^+(\mathbf{p}_3) + X^+(\mathbf{p}_4).$$

This process is more pronounced both for higher ion clouds and larger ion charge states, leading to a direct loss of trapped ions. It can also take place between different ion species and charge states.

4. Trap imperfections. In this case the characteristic ion motions inside a Penning trap become perturbed, and the ion cloud can expand so far that some ions strike the electrodes. This loss mechanism is an integral characteristic of the experimental apparatus and depends only weakly on the residual gas pressure and on the ion charge state.

It is not trivial to disentangle the different ion loss mechanisms, and the level to which it is possible depends on the measurement technique. Because of different scaling factors, e.g. q for elastic scattering and q^2 for intra-cloud scattering, this becomes especially pronounced when trapping different charge states of the same atom, allowing direct disentanglement of the two loss mechanisms.

As described in the previous section, there are three ways to measure ion lifetime in SpecTrap - destructively with an MCP, or non-destructively using an electronic or an optical signal from the trapped ions. Since the total number of trapped Mg^+ was insufficient for a direct, continuous electronic detection, the lifetime was measured using the MCP and the optical signal.

6.2.1. Destructive measurement

Since the method where ions are stored for some amount of time and ejected towards an MCP for counting does not require any additional instrumentation it is typically used to initially verify ion trapping and determine the trapping time constant. This was also the case in this work: Mg ions were trapped between the capture and the reflector electrode and ejected towards the bottom detector, which was used to determine both the time of flight and the number of impinging ions. The left part in Fig. 6.2 shows a time-of-flight spectrum of the ejected ions. The signal width is about 4 μs, which is considerably larger than the 1 μs pulse shown in Fig. 5.1 that is injected into the trap. The reasons for this are the loss of the bunch structure after many oscillations inside the trap, as well as the coupling of different eigenmotions that leads to a decrease of energy in the longitudinal direction.

The graph on the right in Fig. 6.2 shows the number of ions detected on the MCP as a function of trapping time. Each point was summed over 200 ion trapping/ejection cycles. Several data sets were taken and all of them showed a rapid decrease, well fitted with a single exponential function. The acquired decay time constant of 145(5) ms is, however, much shorter than expected and, as will be shown in the next section, does not correspond to the real trapping time. It is instead limited by the spatial expansion of the ejected ion bunch when leaving the magnetic field, as discussed in section 4.3.3. A large portion of ions is subsequently lost at the small apertures beneath the trap and in front of the MCP. The amount by which an ion bunch will expand is

[1] This process is the basis of evaporative cooling.

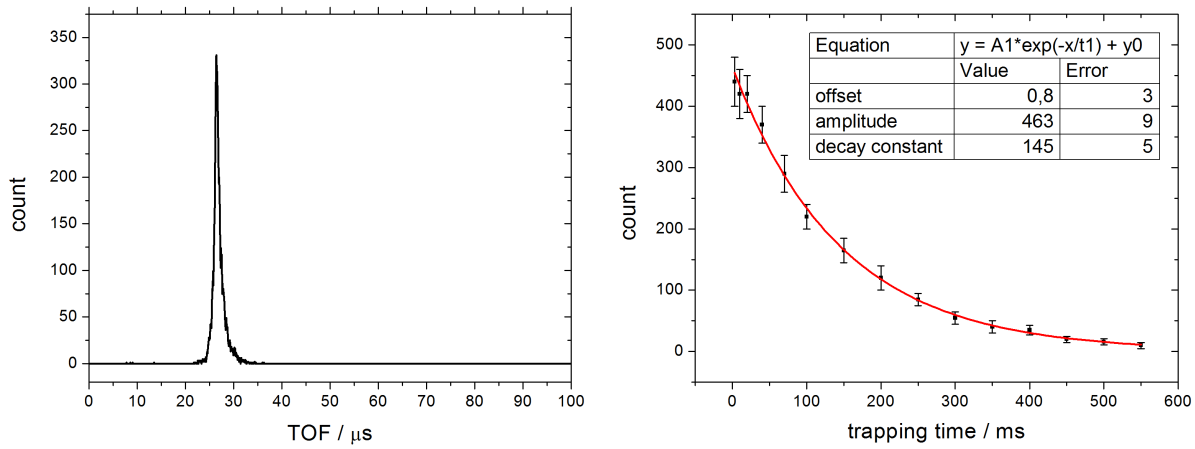

Figure 6.2: Left: Time of flight spectrum of ions ejected from the trap after 50 ms of storage, summed over 200 cycles. Right: Decrease of the number of detected ions after ejection from the trap, fitted with a single exponential function.

directly proportional to the ion transversal energy, which can be increased inside a trap in case of non-ideal trapping conditions which allow otherwise independent ion eigenmotions and energies to mix. The arrival time in the TOF spectrum on the left of Fig. 6.2 is another indication that such energy mixing takes place, since it corresponds to a kinetic energy of 150 eV, rather than the initial ion transport and injection energy of 200 eV.

A similar result was achieved when the ion cloud was compressed within a few ms between the endcap electrodes. Therefore, two conclusions can be drawn from the performed analysis:

- The trap potential is not harmonic between the outer trap electrodes (capture and reflector). This allows strong mixing of the motional energies of the trapped ion cloud. Thus, the cloud size rapidly increases after ejection and propagation through the magnetic field gradient.

- Even the magnetic field in the centre of the trap is non-ideal and needs to be rectified using the shim coils of the superconducting magnet. This can be done either by repeating the procedure described above and optimizing the decay constant, or by monitoring ion transport through the grounded trap and optimizing the MCP signal.

6.2.2. Optical measurement

After ion trapping was established, the non-destructive detection via laser induced fluorescence was used to determine the ion lifetime inside the trap. Beside its non-destructive nature, the method has also the advantage that it is highly selective and resonant only with the desired ion mass and charge state. On the other hand, it requires precise tuning of both the trap and the laser parameters at the same time.

The lifetime of Mg^+ stored in SpecTrap was determined optically by tuning the laser around 200 MHz above the $m_j = -1/2 \rightarrow m_j = -3/2$ resonance frequency and monitoring the fluorescence. Since this blue-detuning of the laser frequency leads to heating, one would expect that ions will continuously gain energy and eventually be lost from the trap. However, it is important to

note that, although the laser is blue-detuned for the this transition, it is still red-detuned for all other possible σ^- transitions, listed in Fig. C.1. Thus, a kind of equilibrium between the heating and cooling processes is established.

Two typical spectra recorded following the described procedure can be seen in Fig. 6.3. Several such data sets were taken and fitted with a single exponential function, showing decay constants between 50 and 140 seconds, with an average value of 90 seconds. This result is roughly three orders of magnitude larger than the decay time constant obtained with destructive measurement, and it supports the argumentation given in the previous section. Moreover, in this measurement the laser was blue-detuned and heated the ion cloud, which actually introduces an additional loss process, and it can therefore be regarded as a lower limit for the ion lifetime.

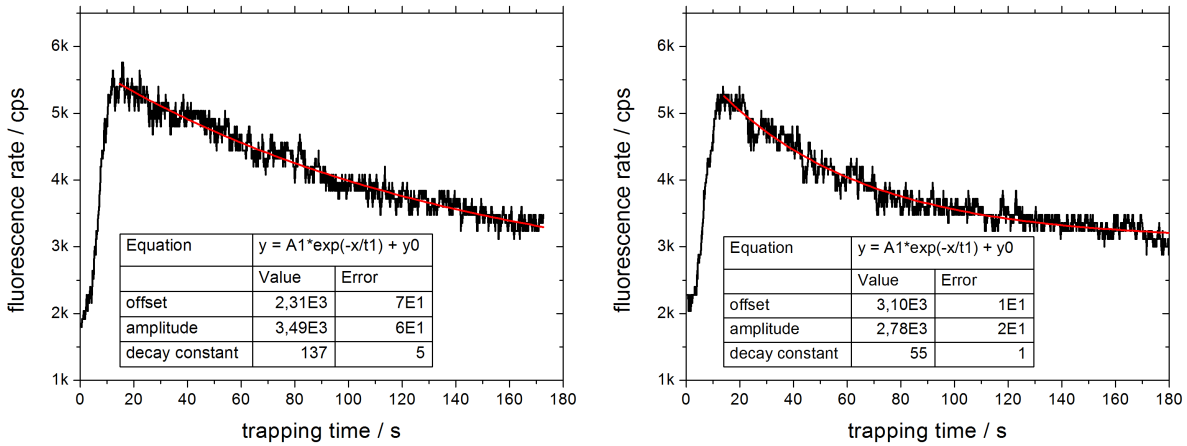

Figure 6.3: Two data sets for determining the lifetime of stored Mg ions by monitoring the laser induced fluorescence. Both were fitted with a single exponential function, which give two different decay time constants. Typical ion lifetime was between the two values throughout this experimental run.

Ion loss seen in Fig. 6.3 can in general be attributed to all four mechanisms listed above. With the exception of trap imperfections, these are collision processes and depend directly on the corresponding interaction cross sections. The geometrical collision cross section is small for atomic ions compared to e.g. stored molecular or cluster ions [72]. The Coulomb interaction cross section is in that case by far dominant and determines the interaction between stored ions and polarizable residual gas particles. It can be described using the Langevin rate coefficient [73]

$$k_L = \frac{\tilde{q}e}{2\epsilon_0}\sqrt{\frac{\alpha}{\mu}}, \qquad \mu = \frac{m_r m_i}{m_r + m_i} \tag{6.1}$$

where $\alpha = 0.8 \cdot 10^{-24}$ cm^3 is the static dipole polarizability of the hydrogen molecule[2] and μ the reduced mass with m_r and m_i as the mass of the residual gas particle and the ion, respectively. The value for H_2 was taken because the partial pressures of all other typical residual gases are much smaller at the cryogenic temperature around the trap and the SpecTrap liquid helium reservoir. Now the collision rate can be obtained by multiplying the coefficient from Eq.(6.1)

[2]In the CGS system cm^3 is a common unit for polarizability. It can be converted to SI units with a factor $\frac{4\pi\epsilon_0}{10^6}$.

with the neutral particle density n

$$k = k_L \cdot n = \frac{\tilde{q}e}{2\epsilon_0}\sqrt{\frac{\alpha}{\mu}} \cdot \frac{p}{k_B T}. \tag{6.2}$$

Assuming a residual gas pressure of $p = 10^{-11}$ mbar and a temperature of $T = 4$ K, the equation yields $k = 0.025$ collisions per second per ion. Both values used for the evaluation of k are conservative estimates: the pressure measured in the warm region of the vacuum chamber was of the order of 10^{-9} mbar, and due to cryopumping the pressure inside the trap is expected to be significantly lower. The temperature of the residual gas is influenced by the room temperature of the the beamline, the temperature inside the cryostat (4 K) and the ion temperature (which is below 1 K after laser cooling as will be shown below).

Not every collision described by the rate k leads to ion loss. In case of elastic scattering the ion is lost only if its resulting kinetic energy E_k divided by its charge q exceeds the trap depth at the position of the ion. This is rather unlikely in SpecTrap, since the trap depth is typically several orders of magnitude larger than E_k/q of the ion. It should be noted that, if the trap depth is smaller, as often the case in ion trapping experiments, ion-neutral elastic scattering can become a significant or even the dominant loss mechanism (see e.g. [74]). The same stands for intra-cloud scattering - a trap depth large in comparison to the ions' energy over charge ensures that almost no ions are lost through ion-ion elastic scattering. It can be concluded that only non-elastic collisions from the total Langevin rate given by Eq.(6.2) lead to ion loss.

The cross-section for electron capture in ion-neutral collisions at lower energies can be approximated with the semi-empirical Schlachter formula [75]

$$\sigma = 1.43 \cdot 10^{-16} \cdot (\tilde{q})^{1.17} \cdot I^{-2.76} \ \left[\mathrm{m}^2\right] \tag{6.3}$$

where I is the ionization potential of the residual gas particle expressed in eV. Under the assumption that the largest fraction of the residual gas in SpecTrap consists of H_2 it is $I = 15.44$ eV [76]. The rate k_{ec} of electron capture can be calculated by multiplying the cross-section from Eq.(6.3) by the neutral particle density n and the relative velocity v_r of the two colliding particles. The ion lifetime is given through the reciprocal value of the electron capture rate

$$t = k_{\mathrm{ec}}^{-1} = \frac{1}{\sigma n v_r} = \frac{k_B T_r}{\sigma p}\left(\frac{3k_B T_i}{m_i} + \frac{3k_B T_r}{m_r}\right)^{-\frac{1}{2}} \tag{6.4}$$

where T_r is the residual gas temperature and T_i the ion temperature. It should be noted that, although in a closed system the temperatures T_r and T_i quickly equalize, it is not the case with residual gas since new particles can any time enter the trapping region from the room temperature part of the system. In general, Eq.(6.4) has three parameters which cannot be measured directly, but must be estimated: the ion temperature, the residual gas temperature and the residual gas pressure. Although the ion temperature can to some degree be determined by measuring the transition linewidth (see section 6.5), best results can be achieved by trapping different ion species and charge states and measuring the corresponding charge state lifetimes. That will become possible after connecting SpecTrap to the HITRAP facility.

Figure 6.4 shows the expected storage times calculated according to Eqs.(6.3) and (6.4) for Mg^+ and two different values for the H_2 residual gas pressure. A comparison of the trapping

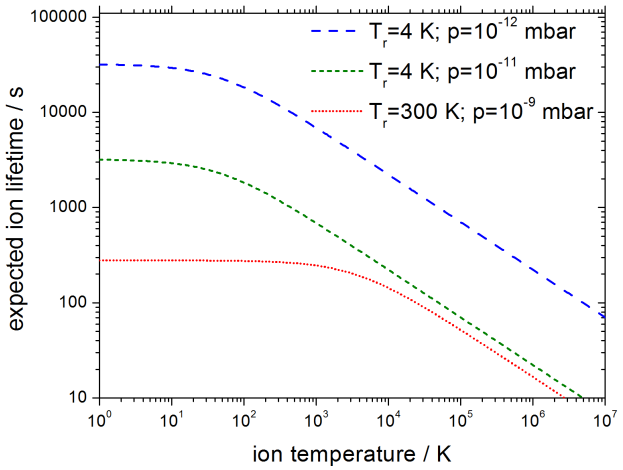

Figure 6.4: Lifetime of Mg^+ at different residual gas pressures, calculated according to Eq.(6.4). As a comparison, the dotted line shows the expected trapping time for residual gas at room temperature, with a neutral particle density similar to the one under cryogenic conditions.

time expected under room temperature and a similar neutral particle density is also given. The experimental data agrees best with the $p = 10^{-11}$ mbar residual gas pressure, which was also expected for the given trapping conditions since the spectra from Fig. 6.3 were taken with a fixed, blue-detuned laser frequency, and the ions were thus not cooled to sub-K temperatures. The exact temperature however, as well as the pressure are difficult to determine.

According to Eq.(6.3), the lifetime of a highly charged ion charge state is expected to scale with $(\tilde{q})^{1.17}$, resulting in $t(Ca^{14+}) = 5$ sec and $t(Pb^{81+}) = 0.5$ sec under the same trapping conditions in terms of residual pressure and temperature. These times are typically insufficient for laser spectroscopy of forbidden transitions. However, as can be observed in Fig. 6.4, they can be significantly increased by rapid cooling to near-K temperatures by resistive or sympathetic cooling or a combination of both. Further improvement is possible by reducing the residual gas pressure by more efficient pumping of the warm part of the beamline, or by separating it better from the cryogenic region by differential pumping.

6.3. Ion number and single ion confinement

Using laser induced fluorescence it was possible to isolate and identify single trapped ions. The spectra shown in Fig. 6.5 were recorded by scanning the laser from -1 GHz with 100 MHz/s across the resonance, applying 0.9 mW continuous wave power. Taken under identical conditions and trapping times, they show quantized changes of the laser induced fluorescence, associated with single trapped ions on top of the continuous background signal.

The area below the resonance peaks seen in Fig. 6.5 represents the total number of photons detected during the scanning time of the respective region. It includes the background events, originating mostly from the laser stray light, and the fluorescence signal. This can be represented by the equation

$$S = b + s \cdot N_i \tag{6.5}$$

where S is the total signal, b the background, s the signal from a single ion and N_i the assumed number of trapped ions. If each scan is associated with a number of stored ions and plotted

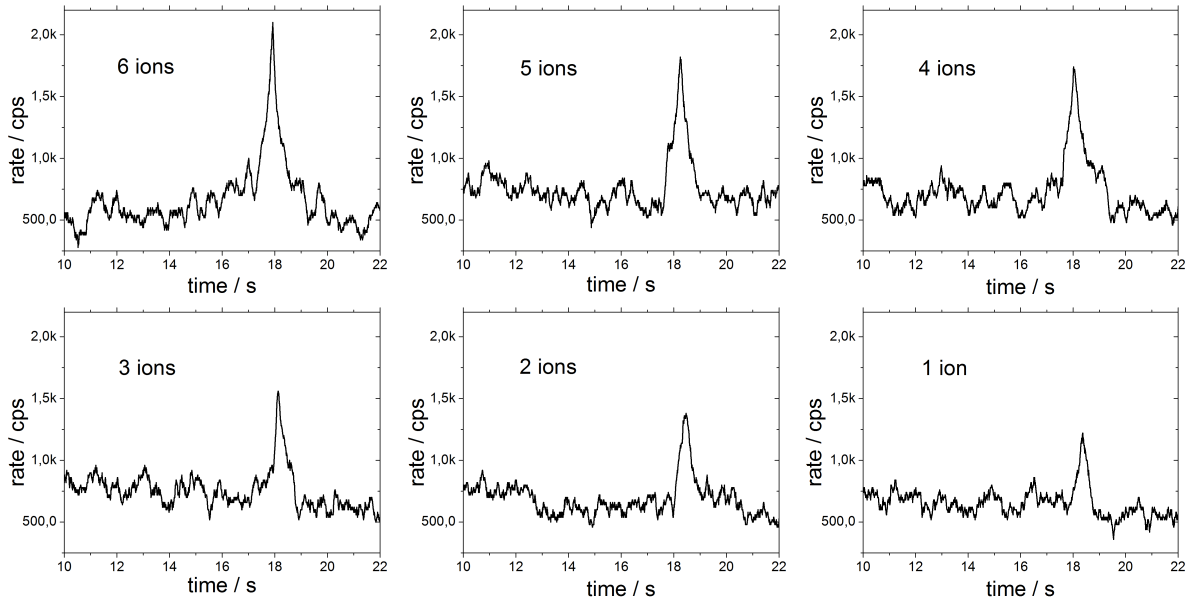

Figure 6.5: Spectra with quantized fluorescence leaps of ions trapped in SpecTrap, associated with single trapped ions. The x-axis is directly proportional to frequency with a factor of 100 MHz/s. The total number of photons per peak was obtained by integrating the recorded fluorescence signals over one second, with the middle of the integration region coinciding with the maximum.

against the observed fluorescence signal, the parameters b and s can be extracted directly from a linear fit of the data. Fig. 6.6 shows this fit, where the area under the resonance peak of each individual laser scan is plotted against the assumed number of ions trapped during the scan.

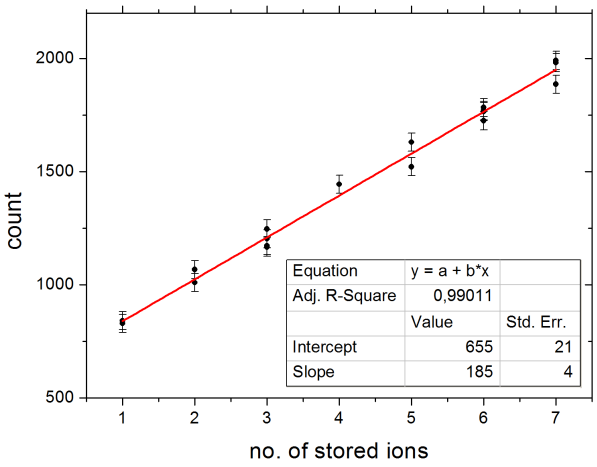

Figure 6.6: Graph showing the integrated number of photons per resonance against an assumed number of ions for the given peak. The linear fit reveals the average number of photons per ion (s) as well as the average background (b). The data are used to verify the assumed number of ions in the spectra from Fig. 6.5.

It can be seen that according to this analysis a single stored Mg ion yields around 185 fluorescence photons per scan, on top of around 650 background photons per second. The uncertainty of these values is, however, significantly larger than the value given by the linear fit from Fig. 6.6. It is mainly dominated by the fluctuations in the background, which can be estimated by using the same spectra shown in Fig. 6.5. The average width of the resonance is 1 second, which is also the time period used for integration of the resonance signal, while the standard deviation of

the measured noise distribution without the fluorescence signal is 90 photons/s. Having that in mind it can be concluded that under the given conditions (0.9 mW laser power and 100 MHz/s scanning) from a single ion a fluorescence signal of

$$s = 180 \pm 90 \text{ photons/s} \tag{6.6}$$

is detected. Even though the uncertainty of s is around 50%, it is an important result, that can be used to benchmark other system parameters and measurements. One of them is the fluorescence collection efficiency, defined as the ratio of detected and emitted photons. The latter can be calculated using Eq.(1.22) and amounts to $A = 2.6 \cdot 10^8$ photons/s for a single saturated magnesium ion (the saturation intensity can be calculated according to Eq.(1.25), and the laser beam size inside the trap was kept around 1 mm in diameter). Since the transition was not fully saturated during the measurements, the expected fluorescence rate amounts to approximately 10^8 photons/s. Thus, it is possible to estimate the fluorescence detection efficiency in SpecTrap for this measurement

$$\xi_{\text{tot}} = 2 \cdot 10^{-6} \qquad \text{and} \qquad \xi_0 = 10^{-5} \tag{6.7}$$

where ξ_{tot} is the total efficiency including the quantum efficiency of the detector, which is around 18% for the wavelength of $\lambda = 280$ nm, as listed in Tab. 4.2. The value ξ_0 assumes 100% detector quantum efficiency and represents the solid angle for fluorescence collection in SpecTrap.

Equation (6.6) can also be used to estimate the number of stored ions according to the recorded fluorescence, if the results are normalized to the laser scanning rate and power. Such a spectrum is shown in Fig. 6.7. It was recorded with 100 MHz/s laser scanning speed and 0.7 mW power. The integrated sum over one second amounts to some $3 \cdot 10^5$ photons, which according to the result of Eq.(6.6) corresponds to around $(2 \pm 1) \cdot 10^3$ trapped Mg ions. This was achieved with 1 min stacking time at 3 Hz, during which time the laser was not scanned, but kept 1 GHz red detuned. A further increase in stacking time did not improve the number of accumulated ions due to the loss processes in the trap.

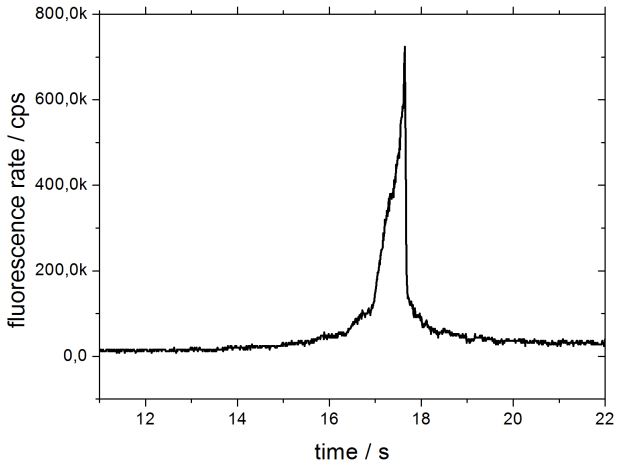

Figure 6.7: Graph showing the fluorescence of around 2000 Mg ions trapped in SpecTrap. The laser was scanned with 100 MHz/s at 0.7 mW power. This value represented the upper limit in the number of stored ions, without significantly changing the parameters of the ion source.

The results show that ion stacking works well when exploiting the longitudinal energy loss the ions experience in the process of injection into the magnetic field and the trap and combining it

with laser cooling. An analogous technique can be used for trapping and accumulating other ion species with sympathetic cooling by the pre-cooled Mg ions used as a cooling mechanism for ion stacking.

However, although the achieved number of trapped ions is sufficient for purposes of laser cooling, it is insufficient for laser spectroscopy of much slower, forbidden transitions found in highly charged ions. An increase is possible if a different ion source is used, such as a HITRAP decelerated ions or the Dresden EBIT. They are both designed to deliver μs bunches with several thousand ions, i.e. a number of ions several orders of magnitude larger than the present output of the Mg ion source. That way, Mg^+ and a HCI species could be simultaneously transported into the trap through the two horizontal branches of the SpecTrap beamline and mixed in the trap.

6.4. Fourier transform ion cyclotron resonance

The maximum number of approximately 2000 ions in the trap was insufficient for direct electronic detection. Thus, it was necessary to excite the ion motion in order to increase the electronic signal. Such a possibility was not foreseen for ion axial oscillation and is actually prohibited due to the filters attached to the endcaps. Another option is to use the capture electrode for axial excitation, which was not attempted in this experimental run, but remains an option for future experiments.

However, it was foreseen to address the ion radial motion for applying the rotating wall technique. Hence, a signal for ion excitation was generated by an Agilent 33250A frequency generator and processed by the SpecTrap rotating wall drive, which was set to produce two signals with the same amplitude and frequency, but 180° phase difference. These two signals were transmitted to two opposing ring segments, while the remaining two were kept at the DC potential. This electric dipole excitation, carried out close to the ion cyclotron frequency, forced all ions to oscillate in phase and increased their motional amplitudes. Once the excitation stops, this coherence is quickly lost due to the strong Coulomb interaction between the ions. Therefore, the electronic signal induced in the trap electrodes has to be recorded immediately after excitation. This was performed with an HP3589A spectrum analyser, which received the signal from one of the SpecTrap cyclotron amplifiers, triggered by the end of the excitation period. The observed resonance signal is plotted in Fig. 6.8.

Due to the different magnetron radii, different ions experience slightly different magnetic field strengths and will thus differ in their reduced cyclotron frequencies. This results in a dependence of the width of the stored ion cloud's frequency distribution on the total number of ions. In Fig. 6.8 the resonance width is around 100 Hz, while the central frequency of the ion cyclotron oscillation can be determined with an accuracy of a few Hz. The extracted central frequency can be used to determine the magnetic field strength according to Eq.(2.12) with a ppm resolution. Since this value is already more precise than the designed magnetic field homogeneity of the SpecTrap superconducting magnet, as presented in Fig. 4.1, any further improvement in determining the central frequency is pointless. However, this accuracy is sufficient for the purpose of non-destructive detection and identification of stored ion species.

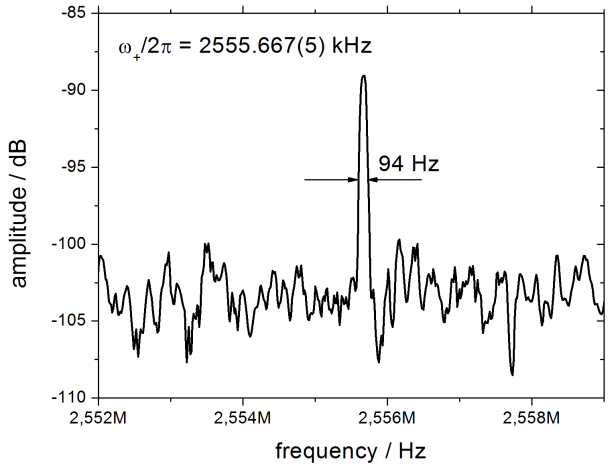

Figure 6.8: Fourier transform of Mg^+ ion cyclotron resonance signal. Approximately 2000 ions were trapped at a magnetic field of 4 T and excited with 5000 cycles of a 2.555 MHz signal, with an amplitude of 400 mV_{pp}. The signal induced in the ring electrode was recorded with an HP3589 spectrum analyser.

6.4.1. Ion cyclotron frequency measurement using laser induced fluorescence

An additional measurement of the ion cyclotron resonance was performed, by monitoring the laser induced fluorescence while changing the excitation frequency. The idea behind the measurement is that the transfer of energy into the cyclotron motion will push the ions into larger orbits, where they either have a smaller overlap with the narrow laser beam, or are even lost from the trap, while the possibility of a change in the fluorescence due to Doppler broadening is excluded because of strong simultaneous laser cooling. Both processes result in a reduced fluorescence and become more pronounced as the excitation frequency approaches the resonance.

The result of this measurement is plotted in Fig. 6.9. The trap was reloaded under identical conditions for each point, the ions were laser-cooled and their fluorescence recorded while applying the dipole excitation frequency to the ring electrode. The excitation frequency was changed stepwise across the expected cyclotron resonance, while the amplitude was not changed. This resulted in a fluorescence dip seen in Fig. 6.9, fitted well with a Gaussian function, with the central frequency marking the ion cyclotron resonance. It was noticed that the range of possible excitation amplitudes was rather narrow - excitation with more than 400 mV_{pp} resulted in a total loss of fluorescence or even ion loss, i.e. the fluorescence did not return after switching off the excitation. Contrary, amplitudes smaller than 100 mV_{pp} had little or no observable influence on the ion motion.

Although not as precise as FT-ICR, this method can be used to determine the ion cyclotron frequency with around 200 Hz precision. However, it can be seen that the central frequencies from the two measurements, shown in Fig. 6.8 and Fig. 6.9, differ by 1.33 kHz. This was found as a systematic shift from several repeated measurements and corresponds to a magnetic field difference of 2 mT. The discrepancy is ascribed to the non-ideal magnetic field and the different spatial positions where the two measurements were performed: while the FT-ICR induces a signal directly in the trap electrodes, the laser induced fluorescence depends on the optical axis of the detector system, which is not necessarily aligned exactly along the trap radial axis[3]. Nevertheless, it was demonstrated that electronic and laser induced fluorescence ion detection methods can be

[3]It is indeed offset by a few mm.

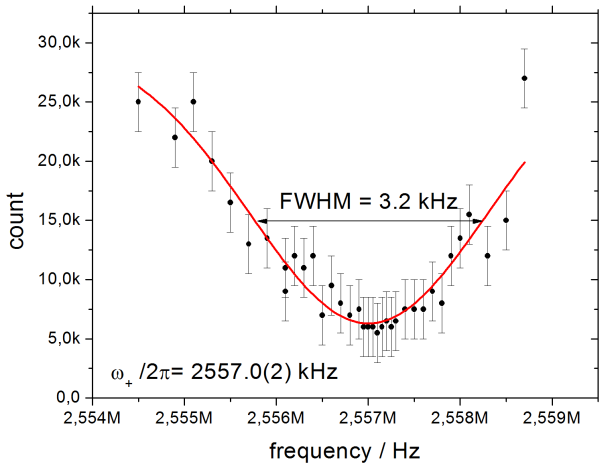

Figure 6.9: Results of ion cyclotron resonance measurement using laser-induced fluorescence. The ion trap was reloaded for each step, the ions were laser cooled and dipole-excited with 400 mV_{pp}. A Gauss fit of the recorded data points reveals the central frequency.

used simultaneously, with a reasonably good agreement. This feature of the experimental setup is unique under Penning traps in operation and offers many possibilities for future experiments, such as research of ion cloud and non-neutral plasma dynamics [55, 57].

6.5. Ion temperature and evidence of crystallization

The most important figure of merit in laser cooling experiments is the final temperature of the ions, and in this work it was obtained using laser-induced fluorescence of the stored Mg^+. Determining the transition linewidth $\Delta\nu$ and assuming the absence of line-broadening mechanisms other than Doppler broadening, the ion temperature T can be calculated according to Eq.(1.24) as

$$T = \frac{\Delta\nu^2 mc^2}{8\nu_0^2 k_B \cdot \ln 2}. \tag{6.8}$$

A common problem of this measurement technique is the fact that the scanning laser also significantly changes the properties of the ion cloud under investigation. As long as the laser is red-detuned it cools the ions and sharpens the transition. As soon as it crosses the central frequency ν_0 it starts rapidly heating the ion cloud, causing a rapid drop of fluorescence. This can be avoided by using a second transition in the same ion as a probe for the temperature measurement [55]. However, without such a transition or a second laser system, only the upper limit for the transition linewidth can be determined.

A series of measurements was performed in order to determine the transition linewidth of the laser-cooled Mg^+ in SpecTrap. The ion source was set to 3 Hz repetition rate, and Mg ions were stacked for 10 seconds. After ion stacking, the trap was permanently closed and made harmonic by raising the endcap and correction electrode voltages to the required values, resulting in 230 V trap depth. The laser frequency was kept 1 GHz red detuned during ion stacking, as well as for another 10 seconds after closing the trap. It was observed that due to the large initial ion energy this pre-cooling time was necessary for efficient laser cooling to lowest temperatures. After pre-cooling, the laser frequency was scanned over the central transition frequency of Mg^+ and the fluorescence recorded. A typical result is shown in Fig. 6.10, where the recorded fluorescence rate

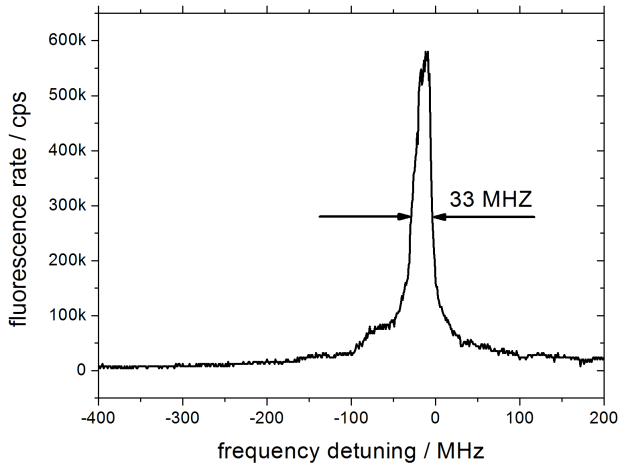

Figure 6.10: Laser induced fluorescence of trapped and laser-cooled Mg ions. As the laser frequency is swept across the resonance frequency, cooling turns into heating, and the fluorescence experiences a rapid drop. The width of the measured transition can be used to determine the upper limit of the ion temperature.

was plotted against the laser frequency detuning. The absolute frequency was determined with a High-Finesse WS/7 wavelength meter, offering an accuracy of about 100 MHz for wavelengths between 370 and 1100 nm. Since the wavelength of the transition in Mg^+ is not within the specified range of the wavelength meter, the second harmonic of the fundamental 1118 nm laser light was used for the frequency measurement, resulting in 200 MHz absolute accuracy at 280 nm.

The peak in Fig. 6.10 clearly exhibits the discussed asymmetry. After crossing the resonance frequency, ion cooling turns into heating and the fluorescence drops quickly to zero. It can therefore be safely assumed that the total FWHM of the Voigt profile is less than twice the observed width of 33 MHz indicated in Fig. 6.10. This value is of the same order of magnitude as the natural linewidth of the transition (42 MHz), and a deconvolution of the Doppler and the natural linewidth contribution to the line profile needs to be performed. A deconvolution of the two full widths at half maximum, accurate down to 0.02%, can be performed with the expression [77]

$$\Delta\nu_V = \frac{1}{2}\left(1.0692 \cdot \Delta\nu_L + \sqrt{0.86639 \cdot \Delta\nu_L^2 + 4 \cdot \Delta\nu_D^2}\right) \tag{6.9}$$

where $\Delta\nu_V$ is the measured FWHM of the Voigt profile, $\Delta\nu_L$ the natural linewidth (Lorentz) contribution and $\Delta\nu_D$ the FWHM of the Doppler (Gaussian) contribution. After deconvolution according to Eq.(6.9), the value for the Doppler width can be inserted into Eq.(6.8) and an upper limit for the ion temperature is obtained

$$\Delta\nu_D \leq 39 \text{ MHz}, \qquad \text{T} \leq 60 \text{ mK}. \tag{6.10}$$

By experience from a similar experiment [55], the typical volume of such an ion cloud is of the order of 0.5 mm^3, resulting in an ion number density of around $n = 4000$ ions/mm^3 for Mg ions stored in SpecTrap. Under such conditions the singe-particle description begins to break down and the ion cloud has to be treated as a non-neutral plasma. This can be seen from the Debye length

$$\lambda_D = \sqrt{\frac{\epsilon_0 k_B T}{2nq^2}} \approx 0.5 \ \mu\text{m} \tag{6.11}$$

which is much smaller than any ion cloud dimension. The plasma coupling parameter, describing the ion Coulomb coupling intensity in one-component plasmas, is given by [78]

$$\Gamma_p = \frac{q^2}{4\pi\epsilon_0 a_s k_B T}; \qquad a_s = \sqrt[3]{\frac{3}{4\pi n}} \tag{6.12}$$

where a_s is the Wigner-Seitz radius. Theory predicts that for coupling parameters $\Gamma_p \geq 2$ the plasma goes through a phase transition and starts exhibiting liquid properties [78]. According to Eq.(6.12), for Mg^+ trapped and cooled in SpecTrap ($n = 4000$ ions/mm^3 and $T \leq 60$ mK) the plasma coupling parameter amounts to $\Gamma_p \geq 7$, making ion crystallization possible.

Studies have already shown that for sufficiently low temperatures, a trapped ion cloud exhibits an abrupt structural change and its spectrum resembles the one of single ions [79, 80]. A similar behaviour was observed for the trapped Mg ions in SpecTrap, and the recorded spectra are presented in Fig. 6.11. A small pre-cooling peak appears in the moment when the transition's Doppler broadened half-width becomes smaller than the laser detuning, after which the fluorescence disappears and can be observed again only close to the natural linewidth of the transition. Such structures were observed also in [79, 80] and mark the phase transition of the stored ion plasma from a non-correlated state to a crystalline structure. The fluorescence close to the central transition frequency is characterized by a sharp asymmetric shape, similar to single-ion spectra from Fig. 6.5, followed by an abrupt drop to zero after crossing the central frequency.

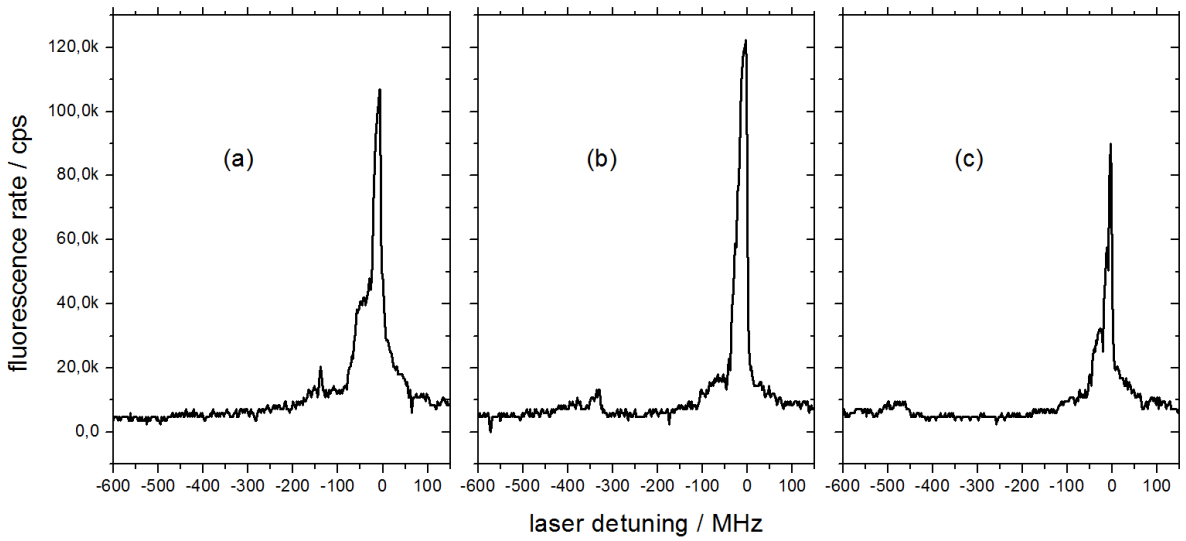

Figure 6.11: Laser induced fluorescence spectra of Mg ions trapped in SpecTrap, recorded for different pre-cooling times: (a) 13 s, (b) 14 s and (c) 15 s.

The spectra shown in Fig. 6.11 were recorded with 1.1 mW of laser power and a 100 MHz/s frequency sweep. It was observed that different precooling times cause different positions of the precooling peak, which itself becomes smaller at larger detuning frequencies, i.e. ion temperatures. This structure was not observed for short precooling times, which were also typically followed by much smaller or no fluorescence at the position of the central transition frequency. However, after allowing sufficiently long precooling time and observing the crystalline structure, a smaller,

sharp fluorescence peak was observed at resonance even when scanning the laser frequency in the opposite direction.

It should be noted that the calculation of the coupling parameter strongly depends on the assumed ion density in the trap, which could not be measured in this experiment. It had to be taken from a previous experiment using the same magnet and Be ions in a hyperbolic trap. Hence, there is circumstantial evidence for crystallization, but a final proof can only be provided using a camera and an imaging system. This, as well as further experiments will be discussed in the final chapter.

The results show, nevertheless, that extremely low ion temperatures can be reached using laser cooling of Mg ions, well into the region where formation of Coulomb crystals is expected. Laser-cooled ions can be used to sympathetically cool any other ion species simultaneously trapped, to a temperature of the same order of magnitude. In comparison to resistive cooling, naturally limited to the temperature of the cryostat, sympathetic cooling offers an additional reduction in the transition Doppler width by at least one order of magnitude. Furthermore, as sympathetic cooling is expected to work quicker than resistive cooling, low ion temperatures can be reached faster. This is also advantageous since it decreases ion loss due to electron capture, as presented in Fig. 6.4, and therefore increases the charge-state lifetime.

As the plasma coupling parameter defined by Eq.(6.12) scales with q^2, for highly charged ions the formation of Coulomb crystals becomes possible at much higher temperatures. In that sense, SpecTrap offers the opportunity to form Coulomb crystals even without laser or sympathetic cooling. On the other hand, by using the rotating wall technique as presented in [57], the plasma coupling parameter can be increased by achieving larger ion number densities, which leads to formation of solid crystals even at moderate charge states and temperatures.

Chapter 7

Conclusions and outlook

A new Penning trap for precision laser spectroscopy of externally produced highly charged ions - SpecTrap - has been installed and commissioned within this work. It is one of the precision experiments associated with the HITRAP facility for deceleration of heavy highly charged ions produced at the GSI accelerator facility. With addition of an EBIT as an off-line source for medium-heavy highly charged ions, SpecTrap has access to a broad range of ions and charge states, delivered in μs-bunches at several keV/charge kinetic energy and containing up to 10^5 particles [4, 23].

The design of the SpecTrap ion trap follows the studies of Gabrielse and co-workers [43], who investigated ion motion in an open-encdap Penning trap, and goes beyond by implementing an optically transparent ring electrode for direct observation of the ion fluorescence. This is possible since the superconducting magnet has a split-coil arrangement. The crucial part of the ion trap development was the design and implementation of the electronic components used for non-destructive ion detection, signal filtering and amplification. In order to reduce temperature-related noise, many components were tested and constructed to operate in a cryogenic environment at liquid helium temperature and fitted directly below the trap. In SpecTrap, this offers the unique opportunity to conduct simultaneously electronic and optical ion detection.

The Helmholtz-type superconducting magnet and parts of the ion beamline were provided from the Lawrence Livermore National Laboratory. Due to transport damage and in order to meet the experimental requirements at GSI, the complete cryostat, vacuum and ion beamline system was reassembled, optimized and installed on a platform next to the HITRAP horizontal beamline and equipped with the new and dedicated cylindrical Penning trap. The experimental setup now includes a home-made ion source, ion optic and bending elements, as well as drift tubes for ion deceleration and secondary electron multipliers for ion detection. The beamline was constructed to accept ions from two independent sources, thus preparing the planned connection to HITRAP and access to highly charged ions. Additionally, a laser laboratory was built directly underneath the experimental platform holding the SpecTrap magnet and can be used for installing various laser systems needed for laser spectroscopy of the trapped ions. At the moment it houses a fibre laser with two frequency doubling stages, developed in parallel to this thesis [68] and used for laser cooling of Mg^+.

This work has shown that externally produced Mg^+ ions can be captured in-flight, accumulated from many bunches, and laser-cooled to temperatures sufficiently low for formation of Coulomb crystals of even singly charged ions. These ions can be used for sympathetic cooling to temperatures of the same order of magnitude in future experiments. This is a significant result for several reasons. On one hand, due to stronger coupling, ions with higher charge states form Coulomb crystals with very large plasma coupling parameters at these temperatures. This offers the opportunity to conduct highly charged ion plasma and crystal research in combination with the rotating wall technique and a direct optical access for an imaging system, which has so far not been performed. On the other hand, precision laser spectroscopy of ground-state transitions in highly charged ions benefits from the lower temperatures through the reduced Doppler width and the absence of ion energy uncertainty. If compared to the same types of measurements in EBITs or storage rings, SpecTrap offers an improvement in relative accuracy by three to four orders of magnitude. Finally, as a by-product of all these types of experiments, SpecTrap can also conduct measurements of electron capture cross sections at ultra-low energies, which are the dominant ion loss process in the trap and largely unknown.

Laser spectroscopy is usually performed on the lowest-lying long-lived level of the ion of interest, preferably a ground state, with a transition wavelength roughly between 200 and 1600 nm. This is fulfilled for ground-state fine-structure transitions in medium-heavy highly charged ions, listed in Tab. 7.1, and ground-state hyperfine structure transitions in heavy highly charged ions, listed in Tab. 7.2.

Table 7.1: List of highly charged ions with fine-structure transitions suitable for laser spectroscopy measurements. The electronic configuration and the corresponding states are listed to emphasize the similarity to the corresponding group of elements (B-like, C-like, etc.). The relative accuracy of the listed wavelengths is typically of the order of 10^{-4}, with an exception of $\Delta\lambda/\lambda = 10^{-7}$ for Ar^{13+}. All listed transitions are ground-state M1 transitions.

Group	Ion	Configuration	Transition	λ [nm]	A [1/s]
IIIA	$(16)S^{11+}$	$2s^22p$	$^2P_{1/2} - {}^2P_{3/2}$	761.31 [12]	21 [12]
	$(18)Ar^{13+}$	$2s^22p$		441.24 [7]	104 [7]
	$(26)Fe^{13+}$	$3s^23p$		530.43 [12]	60 [12]
	$(27)Co^{14+}$	$3s^23p$		435.18 [12]	109 [12]
IVA	$(20)Ca^{14+}$	$2s^22p^2$	$^3P_0 - {}^3P_1$	569.60 [12]	95 [12]
	$(21)Sc^{15+}$	$2s^22p^2$		435.55 [81]	208 [81]
	$(22)Ti^{16+}$	$2s^22p^2$		337.18 [12]	440 [12]
	$(23)V^{17+}$	$2s^22p^2$		263.44 [12]	921 [12]
	$(33)As^{19+}$	$3s^23p^2$		243.73 [82]	1070 [83]

Precision laser spectroscopy measurements of these transitions represent a sensitive test of corresponding calculations, including the quantum electrodynamics (QED) effects in the extreme fields that exist around the nuclei of highly charged ions. The comparably large nuclear contributions to the transition energies can be eliminated to a large degree by comparing the transition

Table 7.2: List of highly charged ions with hyperfine structure transitions suitable for laser spectroscopy measurements. The measurements were done either in a storage ring (ESR) or an electron-beam ion trap (EBIT). For $^{235}U^{91+}$ a calculation according to Eq.(1.17) and (1.20) is given. All listed transitions are ground-state M1 transitions.

Type	Ion	Transition	λ [nm]	A [1/s]	reference
H-like	$^{165}Ho^{66+}$	F=3 → F=4	572.8(2)	-	EBIT [36]
	$^{185}Re^{74+}$	F=2 → F=3	456.0(3)	-	EBIT [37]
	$^{187}Re^{74+}$	F=2 → F=3	451.7(3)	-	EBIT [37]
	$^{203}Tl^{80+}$	F=0 → F=1	385.82(3)	-	EBIT [84]
	$^{205}Tl^{80+}$	F=0 → F=1	382.18(4)	-	EBIT [84]
	$^{207}Pb^{81+}$	F=0 → F=1	1019.7(2)	20	ESR [6]
	$^{209}Bi^{82+}$	F=4 → F=5	243.87(4)	2849	ESR [5]
	$^{235}U^{91+}$	F=3 → F=4	1538	9	theory [9]
Li-like	$^{209}Bi^{80+}$	F=4 → F=5	1511(48)	12	EBIT [16]

energies in an isonuclear sequence, e.g. H- and Li-like ions [30]. As seen in Tab. 7.2, such a comparison is possible in the case of Bi. The recent successful measurements of the hyperfine splitting in $^{209}Bi^{80+}$ at the GSI experimental storage ring [85] have eliminated the large wavelength uncertainty present in the EBIT measurements [16] and increased the relative accuracy to about 10^{-4}. Together with the already existing value for $^{209}Bi^{82+}$, this offers the opportunity to conduct both measurements in SpecTrap with ions at much lower temperatures and further increase the accuracy by several orders of magnitude. This will provide an important test of QED in the strongest static magnetic field that are available in the laboratory.

Appendix A

Cryogenics

Cryogenics is defined as the science and technology of temperatures below 120 K [86], i.e. extremely low temperatures which do not naturally occur on Earth and their influence on matter. A temperature can be designated as *low* when the Boltzmann thermal energy $k_B T$ is small in comparison to the energy of the process itself. A list of such processes is given in Tab. A.1.

Table A.1: List of characteristic temperatures of some low-temperature phenomena.

Process	Temperature / K
Debye temperature of metals	a few 100
High temperature superconductivity	~ 100
Low temperature superconductivity	~ 10
Cryopumping	< 10
Helium 4 superfluid	2.2
Bose-Einstein condensation	$\sim 10^{-6}$

In order to reach such low temperatures in a laboratory one usually needs to work, directly or indirectly, with cryogenic liquids, which require specialized equipment and handling techniques. This chapter will give an overview of those techniques, especially related to superconducting magnet operation and experimental work in an ultra low temperature environment.

A.1. Cryogenic liquids

Liquid nitrogen (LN) is a liquid state of nitrogen, usually produced by fractional distillation of air. At atmospheric pressure it boils at 77 K making it a cryogenic liquid. Its latent heat of evaporation is 199 kJ/kg, causing it to boil immediately upon contact with a warmer object. On the other hand it freezes already at 63 K - the latter has to be kept in mind if cooling down to lower temperatures, since LN leftovers after precooling can easily solidify and present a serious problem for further usage of the system. Because of its low temperature, most materials in direct contact with LN freeze and become very brittle (especially if they contain water). Therefore, although it is relatively easy to handle, the correct choice of tubing has to be made (for example stainless steel), and any contact with skin has to be avoided.

Liquid helium (LHe) is a liquid state of helium, formed at extremely low temperatures. At atmospheric pressure liquid ^{4}He boils at 4.2 K and remains liquid down to absolute zero. Since its latent heat of evaporation is only 21 kJ/kg, or two orders of magnitude less than water, it has very low cooling capacity: 1 W of heat load will evaporate 1.4 litres per hour. It also means that LHe is very difficult to handle. As an addition to the safety risk coming from the low temperature, improper equipment can result in a complete loss of the liquid without any effective cooling. A comparison of LN and LHe properties to those of water is given in Tab. A.2.

Table A.2: Comparison of liquid helium and liquid nitrogen properties to those of water.

Property	Helium	Nitrogen	Water
Normal boiling point [K]	4.2	77	373
Critical temperature [K]	5.2	126	647
Liquid density [kg/m^3]	125	808	960
Liquid viscosity [μPl]	3.3	152	278
Latent heat of evap. [kJ/kg]	20.4	199	2260
Vaporization rate at 1 W [l/h]	1.38	$2 \cdot 10^{-2}$	$1.6 \cdot 10^{-3}$

From tables A.1 and A.2 it is clear that low-temperature superconductivity can be achieved only by liquid helium cryogenics; the same is true for effective cryopumping. The simplest way of reaching a low cryogenic temperature is by immersing the magnet coils into a liquid helium bath and to making use of its latent heat of evaporation. Therefore the useful temperature range of cryogenic liquids is the one where latent heat exists, i.e. between the triple and critical point. In case of helium, typical operation is very close to the critical point where the difference between the liquid and vapour phases is much less pronounced, making the liquid to vapour densities and the latent heat much smaller. It is still a medium of choice for superconducting applications because, beside having the necessary low temperature, unlike liquid nitrogen, liquid helium is much lighter and less viscous than water. This property allows it to permeate small channels inside superconducting magnet windings and stabilize it.

A.2. Using cryogenic liquids for magnet cooldown

In order to reduce the amount of LHe needed to cool down a cryostat (like a superconducting magnet), a precool procedure is usually performed by filling the LHe reservoir with LN. This procedure takes advantage of the much higher latent heat of LN and precools the cryostat to 77 K. However, although both LN and LHe are bad coolants in terms of their latent heat of evaporation, their vapours both have a very high enthalpy and need much more heat to be warmed up to room temperature. This can be used for further precooling to intermediate temperatures and decreasing the necessary amount of cryogenic liquids. If perfect heat exchange with the liquid and the vapour is assumed, the heat balance equation can be expressed as relative temperature change $\mathrm{d}T$ as a function of mass of a cryogenic liquid $\mathrm{d}m$ vaporized in the process:

$$m_0 C_0(T)\mathrm{d}T = [L_v + C(T - T_v)]\,\mathrm{d}m \tag{A.1}$$

where m_0 is the mass of the object to be cooled, $C_0(T)$ its specific heat, T the temperature, L_v the latent heat of evaporation of a cryogenic liquid with a saturation temperature T_v and vapour specific heat C. Now using Eq.(A.1) the specific cryogen mass required for a cool-down from temperature T_0 can be given by

$$\frac{m}{m_0} = \int_{T_0}^{T} \frac{C_0(T)\mathrm{d}T}{L_v + C(T - T_v)} \tag{A.2}$$

If a good heat exchange between the escaping vapour and the cooled mass can be provided, the $C(T - T_v)$ term from Eq.(A.2) makes a significant difference in the required amount of the cryogenic liquid. In practice this means that helium transfer to a cryostat not yet completely cooled to 4 K should be done at a very slow rate (around 50 mbar of LHe reservoir overpressure) in order to give the escaping gas enough time to exchange heat with the walls. After the temperature is reached, which can be seen in a rapid drop of the He exhaust pressure, and the liquid starts condensing, the rate should be increased (to 200-300 mbar overpressure) in order to minimize the losses in the transfer tube.

A.3. Thermal conductivity and design

A significant contribution to the amount of heat load transferred to a cryogenic vessel is provided by electrical connections from the room temperature to the cryogenic environment. Heat conduction in solids is represented by Fourier's law, and in one dimension, for a solid rod of length L it reads

$$Q = \frac{S}{L} \int_{T_1}^{T_2} k(T)\mathrm{d}T \tag{A.3}$$

where S is the rod (cable) cross-section and $k(T)$ thermal conductivity of the material which varies with temperature. Thermal conductivity integrals of standard materials can be found in literature [87], while Tab. A.3 gives the values relevant for SpecTrap. It can be seen that copper, a typical material used for electrical cables, is undesirable when making a direct connection between room temperature and a 4 K cryostat. Instead, one should rather use constantan (a copper-nickel alloy) or stainless steel, both for the main conductor as well as for the shielding of coaxial cables. The heat load of a cable cab be additionally linearly decreased by increasing the length or decreasing the cross-section surface, as can be seen from Eq.(A.3).

Another important contribution to the heat load of a cryostat comes from black body radiation of warmer surfaces. The total power is given with Stefan-Boltzman's law

$$Q = \epsilon \sigma S T^4 \tag{A.4}$$

where $\sigma = 5.67 \cdot 10^{-8}$ W/(m^{2}K^4) is the Stefan-Boltzman constant, S is the radiating surface area and ϵ is the emissivity coefficient. For two long concentric cylinders, as usually the case with superconducting magnet housing, Eq.(A.4) can be rewritten as [87]

$$\frac{Q}{S_1} = \sigma \frac{\left(T_2^4 - T_1^4\right)}{\frac{1}{\epsilon_1} + \frac{S_1}{S_2}\left(\frac{1}{\epsilon_2} - 1\right)} \tag{A.5}$$

Table A.3: Thermal conductivity of different materials between two typical temperature ranges. Data taken from [87].

Material	300 K to 4 K [W/cm]	77 K to 4 K [W/cm]
Copper (OFHC)	1620	690
Aluminium	730	220
Copper (typical)	460	54
Brass	170	20
Constantan	52	8.8
Stainless steel	30	3.2
G10 fibreglass	1.5	0.17
Nylon	0.8	0.13

where $S_{1/2}$ and $\epsilon_{1/2}$ correspond to surfaces with temperatures $T_{1/2}$, respectively. The emissivity coefficients are added to account for non-ideal black bodies, and they depend strongly on the material, surface finish, radiation wavelength and angle of incidence. Their values for typical materials of technical interest can be found in Tab. A.4.

Table A.4: Emissivity of different materials of typical technical interest. Data taken from [87].

Material	300 K to 77 K	77 K to 4 K
Matt black paint	0.9	0.7
Stainless steel (typical)	0.34	0.12
Stainless steel (mech. polished)	0.12	0.07
Stainless steel (electro-polished)	0.10	0.07
Aluminium (typical)	0.12	0.07
Aluminium (mech. polished)	0.10	0.06
Aluminium (electro-polished)	0.08	0.04
Copper (typical)	0.12	0.06
Copper (mech. polished)	0.06	0.02

The very strong T^4 dependence in Eq.(A.4) together with the values from Tab. A.4 make a strong argument for using intermediate temperature stages of cryogenic vessels, typically one or more layers of liquid nitrogen cooled radiation shielding. As an example, black body radiation to vanishingly small temperature is $Q = 401$ W/m^2 from 300 K and $Q = 2.3$ W/m^2 from 80 K. Vice-versa, it is very difficult to cool down objects by radiation only.

Appendix B

Electronic noise and filtering

Electronic noise is a term used for random fluctuations of an electronic signal. It is present in all kinds of electronic circuits and it limits the accuracy to which a signal can be measured. There are different types of noise, and while some of them are intrinsic characteristics of the material and cannot be removed, like thermal noise, some can be avoided by careful circuit design and choice of materials, like ground loops or flicker noise. Since most noise types are essentially just random fluctuations, different averaging techniques can help to improve the signal and improve the measurement accuracy. Nevertheless, it is often useful to quantify different noise sources and design the circuitry accordingly. An overview of different noise types is given in section B.1.

In general, noise should be distinguished from interference, which is manifested as noise, but caused either by electromagnetic radiation emitted from an external source or simply by an additional, unwanted signal. The main practical difference is that interference can, to a large degree, be removed with electronic filters, which process the signal before it reaches the desired circuit. An overview of the main filter types is provided in section B.2.

B.1. Types of electronic noise

Johnson noise Any resistor or electrical conductor generates a small random voltage signal due to thermal agitation of its charge carriers, independent of an actual voltage signal applied across it. It is commonly known as thermal, or Johnson noise, and it is characterized by a flat frequency spectrum (the so-called *white noise*), meaning that it has the same noise power per hertz of frequency. For a resistance R at a temperature T the root mean square (RMS) Johnson noise given by [47]

$$V_{\text{Johnson}} = \sqrt{4k_B T R \delta} \tag{B.1}$$

where δ is the measurement bandwidth in Hz. The amplitude distribution of this type of noise is Gaussian. As Johnson noise voltage depends not only on the resistance and temperature, but also on the measurement bandwidth, it is useful to define a *noise density*. It is given by

$$v_n = \frac{V_{\text{Johnson}}}{\sqrt{\delta}} \tag{B.2}$$

with a unit of $\text{V}/\sqrt{\text{Hz}}$.

Thermal noise is found on capacitors as well and usually referred to as kTC noise. However, since in RC circuits the ohmic resistance contributes both to noise and to its filtering, the noise bandwidth $\delta = 1/4RC$ eliminates it from the equation. The RMS voltage is then given by

$$V_{kTC} = \sqrt{\frac{k_B T}{C}} \tag{B.3}$$

where C is the capacitance.

Shot noise This type of noise appears because the electric current is not a continuous flow, but consists of discrete charge carriers. Therefore, for a given current, it becomes significant only when the uncertainties in the Poisson distribution of electrons become comparable with the electrical current itself. Its RMS value is given by [47]

$$I_{\text{shot}} = \sqrt{2eI\delta} \tag{B.4}$$

where e is the elementary charge and I the direct current through the conductor. It can be calculated that for a current of $I = 1$ A shot noise is of the order of $I_{\text{shot}} = I/10^7$, measured over 30 kHz bandwidth. However, for a current of 1 pA, e.g. a signal picked up from a Faraday cup, it amounts to $I_{\text{shot}} = I/10$, measured over the same bandwidth. Shot noise is also characterized with a Gaussian amplitude distribution, making it another type of white noise, where noise density can be defined analogous to Eq.(B.2).

Flicker noise While Johnson and shot noise are unavoidable physical quantities of ideal electrical conductors, flicker noise is excess noise present in all real electronic components. It appears because of resistance fluctuations, presence of impurities in the conducting channel, bad casing connections, etc. In general, different types of resistors have different characteristic excess noise, typically between 0.01-3 μV on a 10 kHz bandwidth [47]. Flicker noise is usually referred to as $1/f$ noise, or *pink noise*, because its power density spectrum has roughly a $1/f$ distribution, where f is the frequency. The reason for this is that at higher frequencies this type of noise becomes suppressed by other, white noise sources.

Ground loops Strictly speaking, ground loops are not a type of noise, but an unwanted effect which appears when two circuits are connected in points which should be at the same potential, typically ground, but in reality differ by a certain value. An illustration of a ground loop is given in Fig. B.1, showing two circuits with a common ground. Ideally the resistance of the ground connection R_{G} should be zero, in which case $V_{\text{out}} = V_2$. However, if the ground conductor has a non-zero resistance the current flowing through R_1 generates a voltage drop on R_G. The output voltage is then given by

$$V_{\text{out}} = V_2 - \frac{R_{\text{G}}}{R_{\text{G}} + R_1} V_1 \tag{B.5}$$

which means that the two circuits are no longer independent, but interfere with each other. Additionally, the ground conductor presents in this case a possible safety issue, since it is on a non-zero potential, even if $V_2 = 0$. In practice, ground loops often appear when using systems with floating ground or simply with a poor ground connection, which results in unstable, noisy

voltages. For instance, two voltage supplies plugged into different power outlets can generate a spurious current between them, modulated typically at 50 Hz or a harmonic thereof.

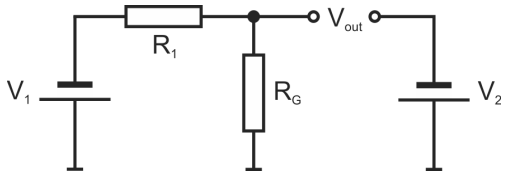

Figure B.1: Illustration of a ground loop. If the resistance R_G of the ground conductor is non-zero, it generates a voltage drop, which changes the output voltage of V_2.

B.2. Electronic filters

Filter types Electronic filters are circuits capable of processing AC signals depending on their frequency, typically in order to remove a certain unwanted frequency range. They can be constructed to attenuate frequencies smaller or bigger than a certain value (high-pass and low-pass filters, respectively) or to suppress frequencies inside or outside a certain frequency span (bandpass and notch filters, respectively). These characteristic frequencies are known as cut-off frequency ν_C for high- and low-pass filters, and central frequency ν_0 for bandpass and notch filters. The theory describing electronic filter operation can be found in many textbooks (e.g. [47, 48]), and an overview of the main four types is given in Fig. B.2.

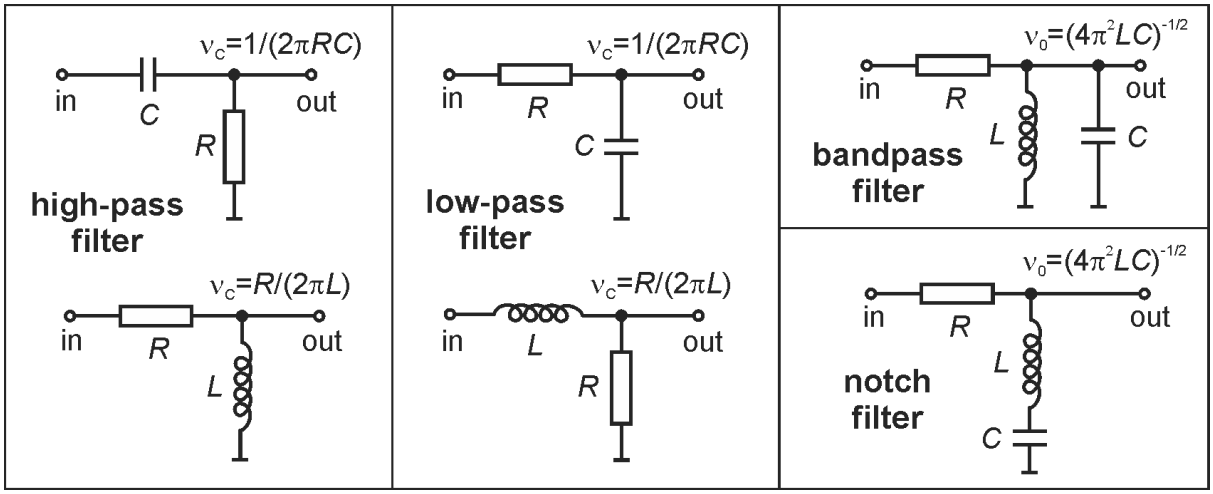

Figure B.2: The main passive, analog, first-order filter types with the corresponding cut-off frequency ν_C or central frequency ν_0.

Signal-to-noise ratio As electronic signal processing often spans several orders of magnitude, it is convenient to express filter attenuation (or amplifier gain) in decibels. As the unwanted frequency range which needs to be filtered out is typically seen as noise, one can speak of signal-to-noise ratio, given by

$$A_{\mathrm{dB}} = 10 \log \frac{V_s^2}{V_n^2} \tag{B.6}$$

where V_s is the signal and V_n is the noise. The reason for using squared voltages is the fact that power is proportional to the square of the voltage amplitude. Also, when adding two uncorrelated signals (e.g. signal and noise), their amplitudes do not add, while their squared amplitudes do add. In that sense, the cut-off frequency of a filter is the frequency where the signal power drops by one half, i.e. when the voltage drops by a factor of $1/\sqrt{2}$ or 3 dB.

Higher order filters The rate of fall in attenuation as a function of frequency is usually described in dB/decade, i.e. in attenuation fall (or gain) in dB when the frequency changes by a factor of ten. Common high- and low-pass filters shown in Fig. B.2 typically have a frequency attenuation of 20 dB/decade, as indicated in Fig. B.3 for a sample low-pass filter. Following the same example, if several filters of the same type are connected in series, frequencies can be attenuated more steeply, making a filter of the nth order for n connected first order filters.

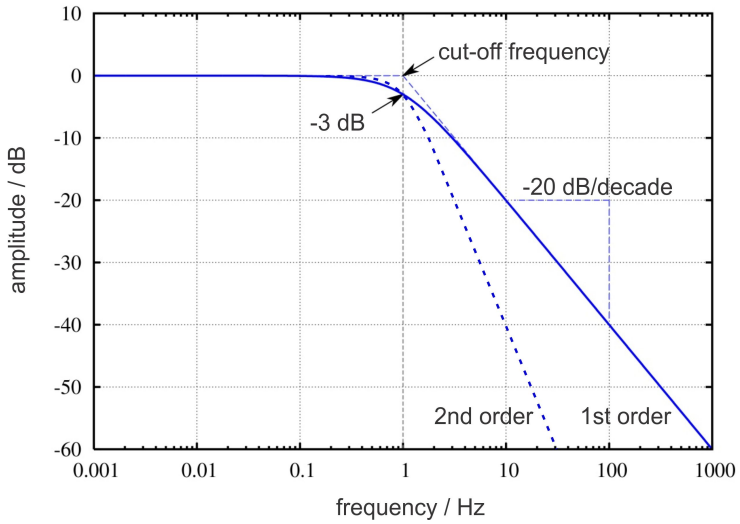

Figure B.3: Frequency response of a passive low-pass filter, of the first order (solid line) and the second order (dotted line). The position of the cut-off frequency is also indicated.

Appendix C

Level structure of Mg ions

In the presence of an external magnetic field, the sharp $3p\,^2\mathrm{S}_{1/2} \rightarrow 3p\,^2\mathrm{P}_{3/2}$ spectral line in Mg^+ splits into multiple closely spaced transitions. Known as the *Zeeman effect*, this splitting is attributed to the interaction between the magnetic field and electrons with different quantum numbers. For the ground-state transition in Mg^+ this results in six energy levels with different m_j quantum numbers, and the transitions between them follow the selection rules listed in Tab. 1.1. Figure C.1 shows an overview of the allowed transitions.

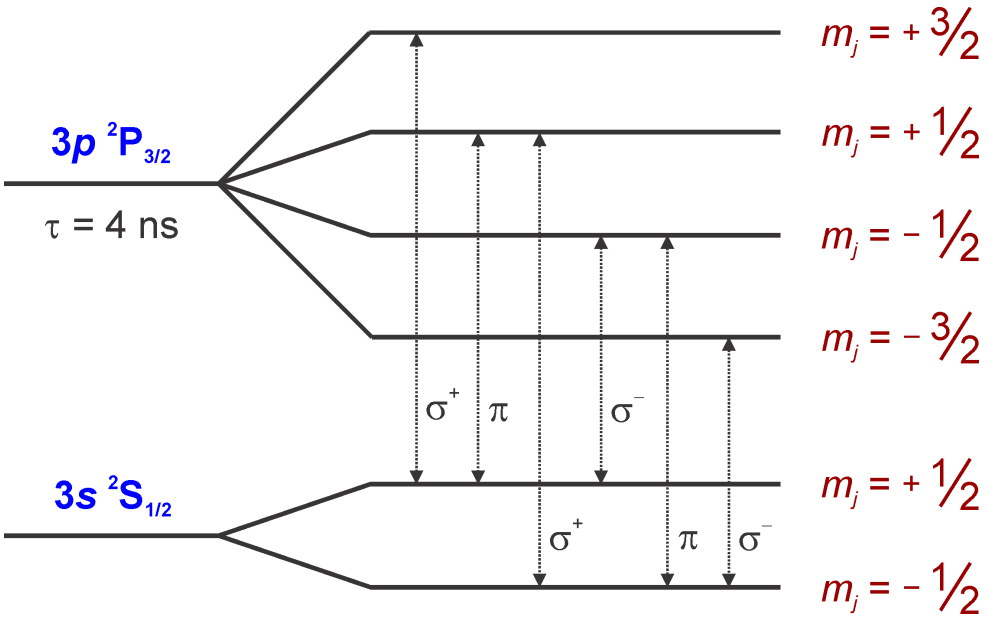

Figure C.1: Zeeman splitting of the $3p^2\mathrm{S}_{1/2} \rightarrow 3p^2\mathrm{P}_{3/2}$ ground state transition in Mg^+, used for laser cooling. The necessary polarisation for driving the corresponding transition is also indicated.

Bibliography

[1] T.T. Fang, C.R. Canizares : *Probing Cosmology with the X-Ray Forest*, Astrophys. J. **539** 532 (2000)

[2] M.A. Levine, R.E. Marrs, J.R. Henderson, D.A. Knapp, M.B. Schneider: *The Electron Beam Ion Trap: A New Instrument for Atomic Physics Measurements*, Phys. Scr. **T22** 157 (1988)

[3] B. Franzke: *The heavy ion storage and cooler ring project ESR at GSI*, Nucl. Instr. Meth. Phys. Res. B **24-25** 18 (1987)

[4] H.-J. Kluge, *et al.*: *HITRAP - A facility at GSI for highly charged ions*, Advances in Quantum Chemistry **53** 83 (2008)

[5] I. Klaft, et al.: *Precision Laser Spectroscopy of the Ground State Hyperfine Splitting of Hydrogenlike* $^{209}Bi^{82+}$, Phys. Rev. Lett. **73** 2425 (1994)

[6] P. Seelig, et al.: *Ground State Hyperfine Splitting of Hydrogenlike* $^{207}Pb^{81+}$ *by Laser Excitation of a Bunched Ion Beam in the GSI Experimental Storage Ring*, Phys. Rev. Lett. **81** 22 (1998)

[7] J.R. Crespo Lopez-Urrutia, *et al.*: *High precision measurements of forbidden transitions in highly charged ions at the Heidelberg EBIT*, Nucl. Inst. Meth. Phys. Res. B **235** 85 (2005)

[8] M.S. Safronova, W.R. Johnson, U.I. Safronova: *Relativistic many-body calculations of energies of n=2 states for boronlike ions*, Phys. Rev. A **54** 2850 (1996)

[9] V.M. Shabaev: *Hyperfine structure of hydrogen-like ions*, J. Phys. B: At. Mol. Opt. Phys. **27** 5825 (1994)

[10] R.E. Marrs: *Recent Results from the EBIT and Super EBIT at Lawrence Livermore National Laboratory*, Phys. Scr. **T73** 354 (1997)

[11] H. Watanabe, *et al.*: *Characteristics of the Tokyo Electron-Beam Ion Trap*, J. Phys. Soc. of Japan **66** 3795 (1997)

[12] Yu. Ralchenko, A.E. Kramida, J. Reader, and NIST ASD Team (2008). NIST Atomic Spectra Database (version 3.1.5), [Online]. Available: http://physics.nist.gov/asd3 National Institute of Standards and Technology, Gaithersburg, MD

[13] J.D. Gillaspy: *Highly charged ions*, J. Phys. B: At. Mol. Opt. Phys. **34** R93 (2001)

[14] T. Beier: *The g_j factor of a bound electron and the hyperfine structure splitting in hydrogenlike ions*, Phys. Rep. **339** 79 (2000)

[15] W. Greiner, B. Müller, J Rafelski: *Quantum Electrodynamics of Strong Fields*, Springer Berlin (1985)

[16] P. Beiersdorfer, A.L. Osterheld, J.H. Scofield, J.R. Crespo López-Urrutia, K. Widmann: *Measurement of QED and Hyperfine Splitting in the $2s_{1/2}$- $2p_{3/2}$ X-Ray Transition in Li-like $^{209}Bi^{80+}$*, Phys. Rev. Lett. **80** 3022 (1998)

[17] H.F. Beyer, V.P. Shevelko: *Atomic physics with heavy ions*, Springer (1999)

[18] L. Dahl, W. Barth, Th. Beier, W. Vinzenz, C. Kitegi, U. Ratzinger, A. Schempp: *The HITRAP Decelerator Project at GSI*, JACoW Conf. Proc. of EPAC 2006, Edinburgh 1568 (2006)

[19] B. Hofmann, A. Schempp, O. Kester, *The HITRAP RFQ decelerator at GSI*, JACoW Proc. of EPAC 2006, Edinburgh 1586 (2006)

[20] G. Maero: *Cooling of highly charged ions in a Penning trap for HITRAP*, PhD thesis, Rupertus-Carola University of Heidelberg, Germany (2008)

[21] S. Koszudowski: *Developments for the HITRAP Cooler Trap and mass measurements around $A = 96$ at SHIPTRAP*, PhD thesis, Rupertus-Carola University of Heidelberg, Germany (2009)

[22] E.D. Donets, V.I. Ilushchenko, V.A. Alpert, JINR P7-4124, Dubna (1968)

[23] S. Geyer, A. Sokolov, A. Thorn, G. Vorobyev, Th. Stöhlker, O. Kester: *Characterization of the SPARC-EBIT at GSI*, J. Instrum. **5** C10003 (2010)

[24] A. Sokolov: *Charge breeding investigation in EBIS/T and collision study of ions with cold atoms for HITRAP*, PhD thesis, Rupertus-Carola University of Heidelberg, Germany (2010)

[25] G.K. Woodgate: *Elementary atomic structure*, Oxford University Press, 1983

[26] C.J. Foot: *Atomic physics*, Oxford University Press, 2005

[27] J.D. Bjorken, S.D Drell: *Relativistic quantum mechanics*, 55, McGraw-Hill New York San Francisco Toronto London (1964)

[28] H. Marxer, L. Spruch: *Semiclassical estimation of the radiative mean lifetimes of hydrogenlike states*, Phys. Rev. A **43** 1268 (1991)

[29] M.W. Horbatsch, M. Horbatsch, E.A. Hessels: *A universal formula for the accurate calculation of hydrogenic lifetimes*, J. Phys. B: At. Mol. Opt. Phys. **38** 1765 (2005)

[30] V.M. Shabaev, A.N. Artemyev, V.A. Yerokhin, O.M. Zherebtsov, G. Soff: *Towards a Test of QED in Investigations of the Hyperfine Splitting in Heavy Ions*, Phys. Rev. Lett. **86** 3959 (2001)

[31] W. Demtröder: *Laser Spectroscopy*, Springer (2008)

[32] K.H. Kingdon: *A method for the neutralization of electron space charge by positive ionization at very low gas pressures*, Phys. Rev. **21** 408 (1923)

[33] F.M. Penning: *Glow discharge between coaxial cylinders at lo pressure in an axial magnetic field*, Physica (Utrecht), **3** 873 (1936)

[34] J.R. Pierce: *Theory and design of electron beams*, Macmillan & CO. London (1954)

[35] H.G. Dehmelt, F.L. Walls: *"Bolometric" technique for the RF spectroscopy of stored ions*, Phys. Rev. Lett. **21** 127 (1968)

[36] J.R. Crespo Lopez-Urrutia, P. Beiersdorfer, D.W. Savin, K. Widmann: *Direct Observation of the Spontaneous Emission of the Hyperfine Transition $F = 4$ to $F = 3$ in Ground State Hydrogenlike $^{165}Ho^{66+}$ in an Electron Beam Ion Trap*, Phys. Rev. Lett. **77** 826 (1996)

[37] J.R. Crespo Lopez-Urrutia, P. Beiersdorfer, K. Widmann, B.B. Birkett, A.-M. Martensson-Pendrill, M.G.H. Gustavsson: *Nuclear magnetization distribution radii determined by hyperfine transitions in the $1s$ level of H-like ions $^{185}Re^{74+}$ and $^{187}Re^{74+}$*, Phys. Rev. Lett. A **57** 879 (1998)

[38] K. Blaum: *High Accuracy Mass Spectrometry with Stored Ions*, Phys. Rep. **425** 1 (2006)

[39] D. Hanneke, S. Fogwell, G. Gabrielse: *New Measurement of the Electron Magnetic Moment and the Fine Structure Constant*, Phys. Rev. Lett. **100** 120801 (2008)

[40] M. Vogel, W. Quint: *Trap-assisted precision spectroscopy of forbidden transitions in highly-charged ions*, Phys. Rep. **490**, 1-2, 1 (2010)

[41] F.G. Major, V.N. Gheorghe, G. Werth: *Charged Particle Traps*, Springer (2004)

[42] L.S. Brown, G. Gabrielse: *Geonium theory - physics of a single electron or ion in a Penning trap*, Rev. Mod. Phys. **58**, 1, 233 (1986)

[43] G. Gabrielse, L. Haarsma, S.L. Rolston: *Open-endcap Penning traps for high precision experiments*, Int. J. Mass Spectr. Ion Proc. **88**, 319 (1989)

[44] S. Sturm, A. Wagner, B. Schabinger, J. Zatorski, Z. Harman, W. Quint, G. Werth, C. H. Keitel, K. Blaum: *g Factor of Hydrogenlike $^{28}Si^{13+}$*, Phys. Rev. Lett. **107** 023002 (2011)

[45] *Channeltron Electron Multiplier Handbook for Mass Spectrometry Applications*, taken from http://www.burle.com/cgi/byteserver.pl/pdf/ChannelBook.pdf online (Jan. 2011)

[46] P. Beiersdorfer, St. Becker, B. Beck, S. Elliot, K. Widmann, L. Schweikhard: *Fourier transform - ion cyclotron resonance mass spectrometry - A new tool for measuring highly charged ions in an electron beam ion trap*, Nucl. Instr. Meth.B

[47] P. Horowitz, W. Hill: *The art of electronics*, Cambridge University Press (1994)

[48] P. Scherz: *Practical electronics for inventors*, McGraw Hill (2007)

[49] J.D. Jackson: *Classical Electromagnetism*, Wiley, New York (1975)

[50] D.F.A. Winters, M. Vogel, D.M. Segal, R.C. Thompson: *Electronic detection of charged particle effects in a Penning trap*, J. Phys. B: At. Mol. Opt. Phys. **39** 3131 (2006)

[51] D. Wineland, H.G. Dehmelt: *Principles of the stored ion calorimeter*, J. Appl. Phys. **46** 919 (1975) **98**, 558 (1995)

[52] F. Diedrich, J.C. Bergquist, W.M. Itano, D.J. Wineland: *Laser Cooling to the Zero-Point Energy of Motion*, Phys. Rev. Lett. **62** 403 (1989)

[53] M. Vogel, W. Quint: *Laser spectroscopy by a radiofrequency measurement on a single ion in a Penning trap*, New J. Phys. **11** 013024 (2009)

[54] S. Djekic, J. Alonso, H.-J. Kluge, W. Quint, S. Stahl, T. Valenzuela, J. Verdu, M. Vogel, G. Werth: *Temperature measurement of a single ion in a Penning trap*, Eur. Phys. J. D **31** 451 (2004)

[55] L. Gruber, J.P. Holder, D. Schneider: *Formation of Strongly Coupled Plasmas from Multi-Component Ions in a Penning Trap*, Phys. Scr. **71** 60 (2005)

[56] T.M. O'Neil, *Centrifugal separation of multispecies pure ion plasma*, Phys. Fluids **24** 1447 (1981)

[57] S. Bharadia, M. Vogel, D.M. Segal and R.C. Thompson: *Dynamics of Ca^+ ions stored in a Penning trap with a rotating wall*, Appl. Phys. B *in print*

[58] S. Stahl, private communication

[59] G. Weinberg, B.R. Beck, J. Steiger, D.A. Church, J. McDonald, D. Schneider: *Electron capture from H_2 to highly charged Th and Xe ions trapped at center-of-mass energies near 6 eV*, Phys. Rev. A **57** 6 (1998)

[60] A. Murari, A. Barzon: *Comparison of new PEEK® seals with traditional helicoflex for ultra high vacuum applications*, Vacuum **72** 327-334 (2004)

[61] P.W. Hawkes, E. Kasper: *Principles of Electron Optics*, Academic Press (1996)

[62] D. Tiedemann: *Nuclear charge radius determination of $^{7,10}Be$ and the one-neutron halo nucleus ^{11}Be*, PhD thesis, Johannes Gutenberg University of Mainz, Germany (2009)

[63] R.T. McIver, Jr.: *Trajectory calculations for axial injection of ions into a magnetic field: overcoming the magnetic mirror effect with an R.F. quadrupole lens*, Int. J. Mass Spectom. Ion Proc. **98** 35 (1990)

[64] R. Cazan, C. Geppert, W. Nörtershäuser, R. Sanchez: *Towards sympathetic cooling of trapped ions with laser cooled Mg^+ ions for mass spectrometry and laser spectroscopy*, Hyp. Int. **196** 177 (2010)

[65] S. Albrecht, S. Altenburg, C. Siegel, N. Herschbach and G. Birkl: *A laser system for the spectroscopy of highly charged bismuth ions*, Appl. Phys. B, DOI: 10.1007/s00340-011-4732-8

[66] R. Jöhren, R. Berendes, W. Buglak, D. Hampf, V. Hannen, J. Mader, W. Nörtershäuser, R. Sanchez, C. Weinheimer: *APDs as Single-Photon Detectors for Visible and Near-Infrared Wavelenghts down to Hz Rates*, J. Instrum. **7**, P02015 (2012)

[67] P.A. Franken, A.E. Hill, C.W. Peters, G. Weinreich: *Generation of optical harmonics*, Phys. Rev. Lett. **7** 118 (1961)

[68] R. Cazan: *Preparation of cold* Mg^+ *ion clouds for sympathetic cooling of highly charged ions at SPECTRAP*, PhD thesis, Johannes Gutenberg University of Mainz, Germany (2012)

[69] A.B. Sommer: *Design, Aufbau und Test eines Niederenergie-Strahltransportes für das SpecTrap-Experiment*, diploma thesis, Justus-Liebig University of Giessen, Germany (2009)

[70] Z. Andjelkovic: *Development and Testing of a Trap and Laser System for Spectroscopy of Highly Charged Ions*, diploma thesis, Johannes Gutenberg University of Mainz, Germany (2007)

[71] S. Ulmer, C.C. Rodegheri, K. Blaum, H. Kracke, A. Mooser, W. Quint, J. Walz: *Observation of Spin Flips with a Single Trapped Proton*, Phys. Rev. Lett. **106** 253001 (2011)

[72] M. Vogel: *Erste Modellfreie Bestimmung der Dissoziationsenergien kleiner Metallcluster*, PhD Thesis, Logos Verlag Berlin, ISBN 3-89722-709-6 (2001)

[73] D.A. Church: *Charge-Changing Collisions of Stored, Multiply-charged Ions*, J. Mod. Opt. **39:2** 423 (1992)

[74] H.B. Pedersen, D. Strasser, O. Heber, M.L. Rappaport, and D. Zajfman: *Stability and loss in an ion trap resonator*, Physical Review A **65** 042703 (2002)

[75] A.S. Schlachter: *Charge-changing-collisions*, Proc. 10th Int. Cyc. Conf. Michigan 563 (1984)

[76] G. Herzberg: *Dissociation Energy and Ionization Potential of Molecular Hydrogen*, Phys. Rev. Lett. **23** 1081 (1969)

[77] J.J. Olivero, R.L. Longbothum: *Empirical fits to the Voigt line width: a brief review*, J. Quant. Spectrosc. Radiat. Transfer **17** 233 (1977)

[78] S.L. Gilbert, J.J. Bollinger, D.J. Wineland: *Shell-Structure Phase of Magnetically Confined Strongly Coupled Plasmas*, Phys. Rev. Lett. **60** 2022 (1988)

[79] F. Diedrich, E. Peik, J.M. Chen, W. Quint, H. Walther: *Observation of a Phase Transition of Stored Laser-Cooled Ions*, Phys. Rev. Lett. **59** 2931 (1987)

[80] K. Okada, T. Takayanagi, M. Wada, S. Ohtani, H. A. Schuessler: *Observation of ion Coulomb crystals in a cryogenic linear octupole rf ion trap*, Phys. Rev. A **80** 043405 (2009)

[81] S. Suckewer, J. Cecchi, S. Cohen, R. Fonck, E. Hinnov: *Tracer element injection into PDX tokamak for spectral line identification and localized doppler temperature measurement*, Phys. Lett. A **80** 259 (1980)

[82] J.R. Roberts, T.L. Pittman, J. Sugar, V. Kaufman, W.L. Rowan: *Magnetic-dipole wavelength measurements in the $n = 3$ configurations of highly ionized Cu, Zn, Ga, As, Kr, and Y*, Phys. Rev. A **35** 2591 (1987)

[83] K.N. Huang: *Energy-level scheme and transition probabilities of Si-like ions*, At. Data Nucl. Data Tables **32** 503 (1985)

[84] P. Beiersdorfer, *et al.*: *Hyperfine structure of hydrogenlike thallium isotopes*, Phys. Rev. A **64** 032506 (2001)

[85] M. Lochmann, PhD thesis in preparation, Johannes Gutenberg University of Mainz, Germany (2008)

[86] New International Dictionary of Refrigeration, 3$^{\text{rd}}$ edition, IIR-IIF Paris (1975)

[87] N.H. Balshaw: *Practical Cryogenics*, Oxford Instruments NanoScience (2006)